

Collisionless heating and particle dynamics in
radio-frequency capacitive plasma sheaths

G. Gozadinos

December 3, 2001

**COLLISIONLESS HEATING AND
PARTICLE DYNAMICS IN
RADIO-FREQUENCY CAPACITIVE
PLASMA SHEATHS**

A thesis for the degree of

PHILOSOPHIAE DOCTOR

Presented to

DUBLIN CITY UNIVERSITY

By

GEORGIOS GOZADINOS

School of Physical Sciences

Dublin City University

Research Supervisors:

Dr. David Vender and

Dr. Miles M. Turner


External Examiner: Dr. Declan Diver

Internal Examiner: Dr. Bert Ellingboe

May 2001

Declaration

I hereby certify that this material which I now submit for assessment on the programme of study leading to the award of Philosophiae Doctor is entirely my own work and has not been taken from the work of others save and to the extent that such work has been cited and acknowledged within the text of this work.



.....

Georgios Gozadinos, 31st May 2001

Abstract

The research presented here focuses on the study of phenomena associated with the sheaths present in capacitive rf discharges. A one-dimensional electrostatic current-driven computer simulation based on the Particle-In-Cell scheme is developed in order to treat a semi-infinite plasma in contact with an electrode. The plasma can be collisional or collisionless, ionisation is ignored and one or more ion species can be modelled.

Primarily, the simulation is used to study the electron heating mechanism in the absence of collisions. The currently predominant theory is based on the idea of stochastic heating through a Fermi acceleration mechanism. Existing theoretical models dealing with the problem are sensitive to various questionable assumptions. The theory of stochastic heating based on Fermi acceleration is found to give zero net heating and therefore to be inadequate in providing an explanation for the source of heating in the collisionless case.

In contrast, heating is shown to be the result of the alternating compression and rarefaction of the electron population by the oscillating sheaths. The conditions under which this mechanism gives a non-zero net result are described. An analytic fluid model is derived to illustrate the effect, and results obtained from this model show very good agreement with the simulation. This interpretation of collisionless heating illustrates the collective behaviour of the electrons, and also removes the role of the sheath edge as the source of collisionless heating.

Finally the problem of the plasma-sheath transition through an intermediate "presheath" region is studied for the cases where one or two ion species are present. The presheath region characteristics are compared with existing

theoretical models and good agreement is found. An investigation of the possible values of the average ion velocities compatible with the Bohm criterion, in terms of the values of the particle fluxes and the mean free paths, is performed for the multiple ion species case.

Acknowledgements

Most of all, I would like to thank my supervisors Dr. David Vender and Dr. Miles Turner, whose support, advice and encouragement have been proven invaluable on many occasions. This work would have never reached this stage without their help and friendship.

During my stay in DCU, I have benefited from many people, either directly or indirectly. I wish to acknowledge PRL members Drs. Bert Ellingboe, Mike Kay, Jonathan Goss, and Gilles Cunge as well as my fellow students, Brendan, Roberto, Paul, Deborah, Deirdre, Neil and Angus. Sam and Deirdre's personality and professional dedication have kept me protected from all the things I had to deal with and did not want to.

I am grateful to Prof. Rod Boswell for hosting and supporting my research visit to the Space Plasma and Plasma Processing Group in ANU. During that time, I had the chance to work with Prof. Mike Lieberman whose influence is evident throughout this work. I would also like to acknowledge useful discussions I had with Dr. Terry Sheridan and Prof. Karl-Ulrich Riemann.

My final acknowledgements, to my family, Cecile and my friends in Greece and Ireland must be of a rather different sort. In ways which I shall probably be the last to recognise, they too, have contributed a lot to this work, by letting it go on, or even encouraging it. I do not know how to thank them.

Contents

1	Introduction	13
1.1	Capacitive rf discharges	15
1.2	The sheath	17
1.3	The presheath and the Bohm criterion	18
1.4	Collisionless heating	20
1.5	Modelling	22
1.6	Research goals and outline	24
2	The semi-infinite PIC scheme	26
2.1	Introduction	26
2.2	General PIC implementation	28
2.2.1	Scaling of the physical quantities	29
2.2.2	Particle pushing	30
2.2.3	Charge assignment and electric field evaluation	31
2.2.4	Collisions	32

CONTENTS

2.3	Implementation of the single ion species model	33
2.3.1	Boundary conditions and initial loading	35
2.3.2	Particle loading and relaxation method	36
2.4	Implementation of the multiple ion species model	40
2.5	The collisionless case	43
2.6	Input parameters and diagnostics in the S.U.Sh.I code	44
2.7	Summary	46
3	Electron heating by Fermi acceleration	47
3.1	Fermi acceleration	49
3.2	Fermi acceleration applied to capacitive rf discharges	51
3.2.1	Experimental evidence of collisionless heating	53
3.2.2	Simulations	54
3.3	Calculation of the power deposition due to Fermi acceleration	56
3.4	The quasi-neutrality field	59
3.5	Power deposition into the plasma	63
3.6	“Hard Wall” errors	67
3.7	Direct calculation of heating due to Fermi acceleration	70
3.8	Plasma oscillations near the sheath edge	73
3.9	Summary	74
4	Collisionless heating revisited	77
4.1	The pressure heating equation	79
4.2	Approximate solution of the pressure heating equation	83
4.2.1	Power deposition for the symmetric sheath case	85
4.3	Comparison with the PIC simulation	86
4.4	The asymmetric sheath	90
4.5	Discussion	92

CONTENTS

5	The plasma-sheath transition	95
5.1	Introduction	95
5.1.1	The Bohm criterion	95
5.1.2	The Bohm criterion for multiple ion species	100
5.1.3	The Plasma-Sheath transition	101
5.2	Investigation of the single ion species case	103
5.2.1	The Bohm criterion in the single ion species case	103
5.2.2	The plasma, presheath and sheath regions	105
5.2.3	Plasma potential variation in the presheath	106
5.3	Investigation of the two ion species case	109
5.4	Summary	113
6	Conclusion	117
6.1	The simulation technique	118
6.2	Collisionless heating	119
6.3	The plasma-sheath transition	121
A	Lieberman's model for a collisionless capacitive rf sheath.	123

List of Figures

1.1	A simple schematic of a capacitive rf discharge.	16
2.1	The charge-exchange cross-section used for argon.	34
2.2	The evolution of the ion velocity distribution function	37
2.3	Flow chart of the simulation procedure.	39
2.4	The ion density profile in the collisional case	40
2.5	Density profiles in the two ion species case	42
2.6	Snapshots of the ion/electron density profile in the collisionless case	44
3.1	Illustration of the Fermi model.	50
3.2	The structure of the rf sheath.	56
3.3	The sheath electric fields.	60
3.4	The effect of the quasi-neutrality field on the electron density .	62
3.5	Average power per unit area scaling with current	64
3.6	Average power per unit area scaling with frequency	65

LIST OF FIGURES

3.7	Average power per unit area scaling with temperature	66
3.8	The instantaneous sheath position	68
3.9	The average electron velocity on the sheath edge compared to the sheath velocity	69
3.10	The Hard Wall Approximation error	70
3.11	Electron velocity distributions along the sheath edge	72
3.12	The contribution of stochastic heating to the power per unit area	73
3.13	Plasma oscillations at the sheath edge	75
4.1	The electron density profile for the asymmetric and symmetric cases	87
4.2	Comparison of the power deposition variation from the model and the symmetric PIC simulation	88
4.3	The average normalised power deposition as a function of the parameter H	89
4.4	A comparison of the variation of the normalised temperature τ from the model and the symmetric PIC simulation.	90
4.5	The variation of the normalised temperature in time and space as obtained by the symmetric PIC	91
4.6	A comparison of the power per unit area and P_{pr} variation from the asymmetric PIC simulation	92
5.1	A graphical interpretation of the Bohm criterion	99
5.2	The average ion velocity normalised to the Bohm velocity (sin- gle ion species case)	104
5.3	The charge density for the single ion species case	105

LIST OF FIGURES

5.4	The ion density and potential variation in the bulk, presheath and sheath (single ion species case)	107
5.5	The ion distribution function variation in the bulk, presheath and sheath	108
5.6	The potential variation in the presheath	109
5.7	The ion density and average velocity profiles (2-ion case, constant fluxes)	112
5.8	The ion density and average velocity profiles (2-ion case, constant MFP) I.	114
5.9	The ion density and average velocity profiles (2-ion case, constant MFP) II.	115

List of Tables

2.1	Conversion between physical quantities and PIC variables. . .	30
2.2	Input parameters for the S.U.Sh.I code.	45
2.3	Diagnostics in S.U.Sh.I.	45
5.1	The values of the ion mean free paths, ion densities at the sheath edge and ratio of their average velocity to their individual Bohm speed.	111
5.2	The values of the ion fluxes, ion densities at the sheath edge and ratio of their average velocity to their individual Bohm speed.	113

List of symbols

A	area (m^{-2})
d	distance (m)
D	diffusion coefficient (m^2s^{-1}); D_a ambipolar diffusion coefficient; drift energy flux (Wm^{-2})
e	absolute electron charge ($\simeq 1.6 \times 10^{19}$ C)
E	electric field (Vm^{-1}); energy (J or eV)
f	frequency (Hz); distribution function (m^{-2}s)
I	current (A)
j	$(-1)^{1/2}$
J	current density (Am^{-2})
k	Boltzmann's constant ($\simeq 1.381 \times 10^{-23}$ JK $^{-1}$)
l	length (m)
m	mass (kg); m_e electron mass ($\simeq 9.1 \times 10^{-31}$ kg); m_i ion mass

continued on next page

continued from previous page

n	particle number density (m^{-3}); n_e electron density; n_i ion density; n_g neutral gas density
P	power (W)
p	pressure (Torr)
q	electric charge (C)
Q	heat flux (Wm^{-2})
s	sheath position (m)
S	energy flux (Wm^{-2})
t	time (s)
T	temperature (K, Volts or Joule)
u	velocity (ms^{-1}); average velocity; u_B Bohm velocity
v	velocity (ms^{-1})
V	electric potential (V)
\mathcal{W}	super-particle weighting factor
x	rectangular coordinate
Γ	particle flux ($\text{m}^{-2}\text{s}^{-1}$)
δ	Dirac delta function; small quantity
Δ	Δt PIC timestep; Δx PIC cell size
ϵ_0	vacuum permittivity ($\simeq 8.8 \times 10^{-12} \text{ Fm}^{-1}$)
ζ	small displacement (m)
η	normalized potential
θ	angle (rad)
λ	mean free path (m); λ_i ion mean free path; λ_D electron Debye length (m)

continued on next page

continued from previous page

μ	mobility ($\text{m}^2\text{s}^{-1}\text{V}^{-1}$); μ_e electron mobility; μ_i ion mobility
ν	collision frequency (Hz)
ρ	charge density (Cm^{-3})
σ	cross section (m^{-2}); electrical conductivity ($\Omega^{-1}\text{m}^{-1}$)
τ	normalized temperature
ϕ	angle (rad)
Φ	potential (V)
ω	angular frequency (rad s^{-1}); ω_{pe} electron plasma frequency; ω_{pi} ion plasma frequency

CHAPTER 1

Introduction

The use of capacitively coupled radio-frequency (rf) discharges for dry etching and deposition of thin solid layers on substrates is now very common [1, 2]. Some of the most important application areas include the semiconductor industry, the fabrication of thin film solar cells, and plasma-based hardening of materials in the aerospace, automotive and steel industries.

However, we still lack understanding of the fundamental mechanisms involved in these processes, and although occasionally empirical understanding can be sufficient for the industrial needs, a thorough study of plasmas will enhance our ability to use plasmas efficiently. Towards this aim, the focus of this research will be phenomena associated with the most important regions present in capacitive rf discharges, the plasma sheaths. The reasons why sheaths are important are twofold: on the one hand, sheaths represent the interface between the plasma and any surface that comes into contact with

it, while on the other hand it is in the sheath region where electrons gain the energy necessary to sustain the plasma in low pressure conditions.

Sheaths occur naturally in *any* practical application where the plasma interacts with some material, whether that is the fabrication of microprocessors or launching radio-waves into space by an antenna. In as far as it concerns plasma processing applications, this is even more evident because the processing may depend on the ions which gain energy by being accelerated through the sheath, and the region adjacent to it called the *presheath*, before reaching the surface under process. Despite its importance, ion dynamics through the presheath are still poorly understood. It is therefore of primary interest to gain knowledge of the basic phenomena, particularly in connection with the velocities that the ions acquire falling in the presheath potential.

There is also a trend in plasma processing applications to operate capacitive discharges in low pressure conditions, where the ion mean free path becomes large compared to sheath dimensions and better control over the ion energy can be achieved. Under these conditions electron collisions in the plasma are rare and Ohmic heating no longer constitutes an effective mechanism for power deposition to the plasma. This is crucial because this power is needed in order to sustain the plasma. However, there exists a very effective *collisionless* heating mechanism which imparts energy to the electrons. This mechanism has been associated with the electron dynamics in the sheath region, but despite efforts since the 60's in trying to understand under what conditions and exactly how this happens [3, 4], no satisfactory interpretation of the basic phenomenon has yet been given.

The goal of this research is to provide a better understanding of the phenomena governing ion and electron dynamics in the presheath and sheath

1.1 Capacitive rf discharges

regions. The main objective is to see why and how the current theory on collisionless electron heating fails, as well as to elucidate the mechanism through which it really works. In addition, the sheath formation through a presheath and the ion dynamics within it are briefly examined. To investigate these phenomena numerical simulations are employed. The advantages of this approach are that one can impose conditions that are not easily accessible experimentally and therefore test theoretical assumptions while at the same time, virtual experiments can be carried out with diagnostics that are impossible or very difficult to implement in a “real” experiment.

1.1 Capacitive rf discharges

A plasma is usually defined as a collection of electrons and ions (normally in a quasi-neutral state) which exhibits collective behaviour. In laboratory experiments, the plasma is confined in a chamber and energy is fed to it from an external source. Capacitive (or E-type) discharges [5, 6] with which this work is concerned are driven by a rf voltage/current source applied to the electrodes through a matching unit. The electrodes are usually in direct contact with the plasma as shown in figure 1.1. In contrast with inductive discharges where the rf fields in the plasma are the result of a changing magnetic flux, in capacitive discharges electromagnetic phenomena are minimal and an electrostatic description suffices. The neutral gases that provide the ions are usually noble gases such as Argon or Helium but other gases are also commonly used in applications. Although with certain gases negative ions can be obtained this research is limited to electropositive discharges. Typical voltages applied to the electrodes vary from hundreds to thousands of volts and driving frequencies are in the MHz range, with the the most commonly

1.1 Capacitive rf discharges

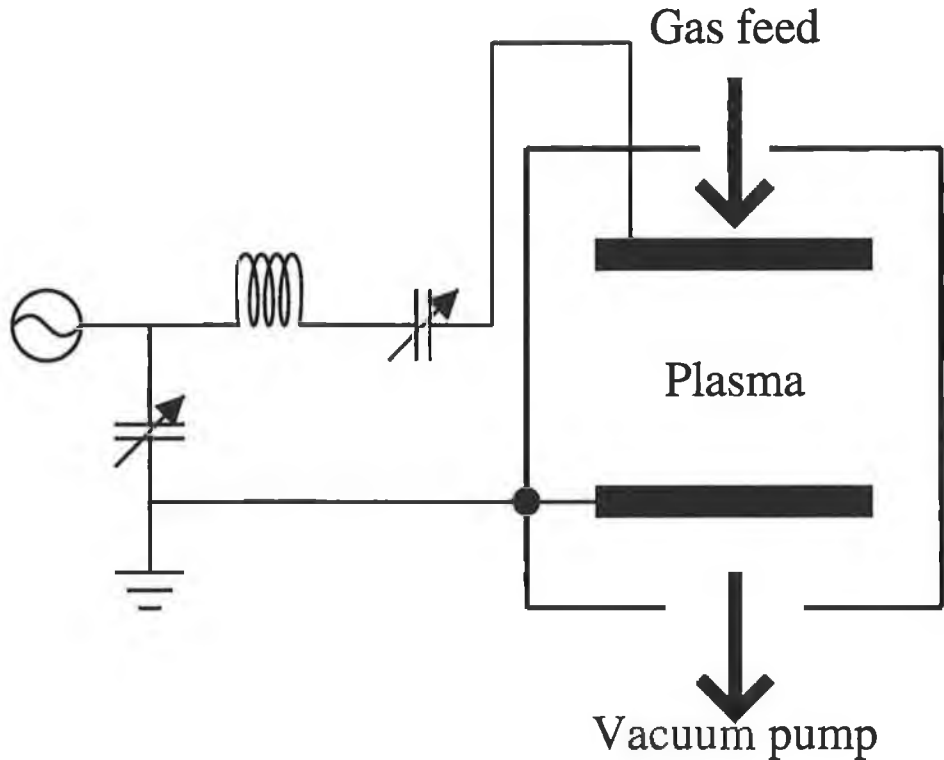


Figure 1.1: *A simple schematic of a capacitive rf discharge.*

used frequency being $f_{rf} = 13.56$ MHz. Discharges are operated at a pressure range varying from milliTorr to Torr range and the charged particle densities are of the order of $10^{14} - 10^{17} \text{ m}^{-3}$. Probably the most important feature of capacitive rf discharges is that they are far from equilibrium, meaning that the typical temperature of the electrons ($1 - 4$ eV) is much higher than that of the ions which have approximately the room temperature. The reason for this is mainly that electrons absorb energy from the rf fields and remain confined in the discharge due to the sheaths, while at the same time they hardly lose any energy when suffering elastic collisions. This is because for elastic collisions the energy transfer is proportional to the mass ratio of the

1.2 The sheath

colliding species.

1.2 The sheath

In capacitive electropositive discharges a high intensity electric field exists in the vicinity of the electrodes. This field points towards the electrodes and is the result of the higher mobility of the negative charge carriers compared to the positive charge carriers. To get some intuition on how and why this happens, let us consider a quasi-neutral plasma in contact with a grounded conductor. Since the electrons have much larger thermal velocities than the ions do, the random electron flux is much higher than that of the ions and more electrons than ions will initially be absorbed by the electrode. This will lead to the breaking of quasi-neutrality in the vicinity of the conductor and the creation of a positive space-charge area. An electric field will therefore appear, repelling the electrons back to the plasma and accelerating the ions towards the electrode. The space-charge region, which is called the *sheath* will continue growing until the ion and electron fluxes are balanced and equilibrium is reached.

Now, when the electrode is driven by an rf voltage (or current), this gives rise to more complicated dynamics. To illustrate the basic phenomena, a simple qualitative model based on one used by Godyak in the 1970's and now widely known as the homogeneous model [3] will be used. Let us start by considering a semi-infinite plasma in contact with a plane electrode and driven by a sinusoidal rf current $I_{rf} = \tilde{I}_{rf} \sin(\omega t)$. In addition it will be assumed for simplicity that the ion density n is uniform and constant in time everywhere, whereas the electron density is equal to the ion density except for the sheath regions near the electrode where it is zero. Using Poisson's

1.3 The presheath and the Bohm criterion

equation, the electric field is found to be

$$E(x, t) = \begin{cases} \frac{en}{\epsilon_0} (x - s(t)) & \text{for } x \geq s(t), \\ 0 & \text{otherwise,} \end{cases} \quad (1.1)$$

where $s(t)$ is the position of the instantaneous sheath edge. Considering now the current through the sheath, since usually $\omega_{pi} \ll \omega$ where ω_{pi} is the ion plasma frequency, the ions carry no rf current. Because in addition there are no electrons in the sheath region the current has to be purely displacement current i.e.,

$$-enA \frac{ds}{dt} = \tilde{I}_{rf} \sin(\omega t), \quad (1.2)$$

where A is the area of the plate. As can be seen from equation (1.2) the sheath front is no longer static (as it would be for a DC current) but instead it oscillates in time. In reality the sheath dynamics are more complicated than is suggested by this introduction: the ions are accelerated by the sheath electric field towards the electrodes and this forces the ion density to drop as we get closer towards the electrode which makes the sheath motion more complex. In addition, the region between the point of maximum expansion of the sheath and the instantaneous sheath edge is not entirely field-free. There are better analytic models that account for these effects, the most useful being Lieberman's analytic model [7], which is reviewed in appendix A.

1.3 The presheath and the Bohm criterion

In order for the transition from the quasi-neutral plasma to the space charge region of the sheath to occur (or in other words in order for the electron density to drop faster than the ion density in the sheath region so that quasi-neutrality is broken), it can be shown [8] that a condition known as the *Bohm* criterion [9, 10] has to be satisfied.

1.3 The presheath and the Bohm criterion

For the case of a single ion species, the Bohm criterion gives

$$\langle u \rangle \geq u_B = \left(\frac{kT_e}{m_i} \right)^{1/2}, \quad (1.3)$$

where u_B is referred to as the Bohm velocity, $\langle u \rangle$ is the average velocity of the ions, k is Boltzmann's constant, T_e is the electron temperature and m_i is the ion mass. With some very rare exceptions the condition described by equation (1.3) is satisfied with the equality sign and readily provides the average ion velocity at the plasma-sheath interface. This has immediate applications to Langmuir probe theory and plasma processing. For example, if the ion current is measured the ion density at the sheath edge can be estimated.

However, if two or more ion species are present, the Bohm criterion is written as

$$\sum_k \frac{q_k^2 n_k}{m_k \langle u_k \rangle^2} \leq \frac{e^2 n_e}{kT_e}, \quad (1.4)$$

where e is the absolute electron charge, n_e is the electron density at the sheath edge and q_k , n_k , $\langle u_k \rangle$ denote the charge, density and average velocity at the sheath edge of the k^{th} ion species. The problem is that equation (1.4) has no unique solution for the average ion velocities. Whether one can obtain special solutions depending on the plasma parameters, and what additional information is required to do so, remains an open question.

Finally, in order for the ions to reach the sheath edge satisfying the relevant Bohm criterion, they need to be accelerated through a region (which can be the entire plasma) called the *presheath*. This acceleration is affected by collisions, ionisation, or current concentration due to the geometry of the discharge [10]. The characteristic length of the presheath layer is of the order of the smallest of the characteristic lengths in the plasma region associated with the ions (such as the ion mean free path, ionisation length or lengths

1.4 Collisionless heating

associated with the discharge geometry).

1.4 Collisionless heating

Sustaining a plasma involves having electrons energetic enough to ionise the neutral gas and maintain the ion population. It is therefore imperative to have a knowledge of how electrons can gain energy. We can distinguish between two types of heating:

- Ohmic or collisional heating occurs when electrons exchange momentum through collisions with neutrals. This is of course a mechanism which is very well understood [1]. The time-averaged power per unit volume deposited to the plasma is

$$P_{ohm} = \frac{1}{2} \tilde{J}^2 \text{Re}(\sigma_p^{-1}), \quad (1.5)$$

where \tilde{J} is the current density, $\sigma_p = \epsilon_0 \omega_{pe}^2 / (j\omega + \nu_m)$ is the plasma conductivity, ω is the driving frequency and ν_m is the collision frequency for momentum transfer.

- Collisionless heating can also occur and it is one of the most interesting phenomena that are associated with sheaths. At high pressure, the plasma can be sustained by the power being deposited to electrons through collisions. At lower pressures though, when the electron mean free path is large enough for the electrons to be essentially collisionless, it has been established experimentally and through simulations that there exists a non-ohmic mechanism that imparts energy to the electrons. The nature of this mechanism has been the subject of very active research for the last 50 years and it is the core theme of this work.

1.4 Collisionless heating

In brief, the currently dominant approach to collisionless heating is based on the paradigm of Fermi acceleration [4] and is usually referred to as *stochastic heating*, *sheath heating* or *wave riding*. The main idea was initially considered in the context of resonant plasma probes [11] and has been later applied to plasmas by Godyak and others [3, 4]. It is commonly considered that electrons travel freely through the bulk plasma of the discharge until they reach the sheath regions, where they “collide” with the sheath electric fields and are being reflected back. Assuming that these collisions are elastic (which is known as the “*Hard Wall*” approximation), i.e. that

$$u_r = -u_i + 2u_s, \quad (1.6)$$

where u_i is the incident velocity of the electron, u_s is the velocity of the sheath front and u_r is the velocity of the electron after the reflection, the particles gain or lose energy depending on whether they move in the opposite or same direction as the sheath front at the time when the collision occurs. Because head-on collisions are more frequent, net energy gain can in principle be expected on average. However, there has recently been some criticism regarding whether the Fermi acceleration mechanism is applied correctly to capacitive discharges and other alternatives have been proposed.

One of the different mechanisms proffered is the so-called *pressure heating*, where power deposition occurs as a result of the alternating compression and decompression of the electron population in the sheath region due to the motion of the sheath edge. This was initially suggested by Surendra [12] to explain the negative power deposition that was observed in the bulk, and further developed to account for sheath heating by Turner [13]. However, no complete model has so far been formulated to illustrate the mechanism and provide predictions comparable to experiments or simulations.

1.5 Modelling

Although experiments provide the basis for the comprehension of the great range of phenomena occurring in plasmas, they are not always sufficient. This is especially true for the matters which are considered in this work. One of the main reasons for this is that taking experimental measurements in the sheath region is an extremely challenging task.

Modelling can in this case be a very good substitute. In addition, it enables us to create situations which are difficult or impossible to obtain experimentally and which can be used to test theoretical models. There are several different techniques used to model plasmas, each with its own advantages and disadvantages, but the following is a useful categorisation:

- *Equivalent Circuit models* are models where the discharge is separated into parts each of which is taken to correspond to a simple electrical circuit. The sheath, for instance, is sometimes seen in these models as a resistor, a capacitor and a diode in parallel. The values of the components can be either estimated theoretically or measured experimentally, and useful properties of the discharge, such as for example the ionic energy at the electrode, can be easily obtained. Obviously, the disadvantage of this approach is that it is somewhat crude, and one could not expect such models to provide insight into complex phenomena.
- *Fluid models* make assumptions regarding the particle distribution function which allows for a reduction of the problem of solving the full Boltzmann equation to solving a set of moment equations. This is done by multiplying the Boltzmann equation by increasing powers of the velocity and integrating over velocity space to obtain each moment

1.5 Modelling

equation. Usually, only the first three moments are used describing particle, momentum and energy conservation. In any case, for each moment equation added to the system a new unknown is introduced, so there is always the need for a closure assumption. This need for a closure assumption, together with the occasional restriction on the form of the distribution function are the disadvantages of these models, which otherwise are very popular because they are computationally cheap and have been tested extensively.

- Finally, *kinetic models* are models where particle dynamics are explicitly accounted for, i.e. no assumption about the distribution function is made. Again, there is a broad variety of models that fit into this category: in Monte Carlo simulations, for instance, the fields are assumed to be known *a priori* and the equations of motion for the particles under the influence of these fields are solved. On the other hand, using the Particle-In-Cell (PIC) technique [14, 15] allows for a self-consistent solution of the Boltzmann equation by simultaneously solving the particle equations together with the fields. PIC simulations vary a lot in their sophistication: one can model one, two or even three dimensional problems in different geometries, include external circuits, use realistic cross-sections to account for chemistry and perform a great range of diagnostics to measure physical quantities. Their main disadvantage is of course that they require more computational time compared to fluid models. Finally, direct solvers of the Boltzmann equation also exist (see [16] for an example).

1.6 Research goals and outline

The general outline of this thesis is as follows: in chapter 2 the simulation method used throughout this research is introduced. The method is based on the Particle-In-Cell simulation scheme which has been modified to model a semi-infinite plasma in contact with an electrode. The plasma can be treated as collisional (using charge-exchange collisions for the ions and elastic scattering for the electrons) or collisionless and ionisation processes are ignored. The fact that only the area near the sheath/presheath regions is modelled allows simulations to be undertaken which closely resemble theoretical models, whose assumptions can be tested. Better diagnostic resolution is also obtained.

In chapter 3, a detailed examination of the theory of stochastic heating through Fermi acceleration follows. This is done through both self-consistent PIC simulations and Monte-Carlo simulations using model fields. The results presented indicate that the presence of a small field in front of the sheath edge which preserves quasi-neutrality is important, and its exclusion from models which attempt to describe the sheath dynamics leads to a violation of current conservation. It is shown analytically that accounting for current conservation between the plasma and the sheath does not permit net heating to occur under the Fermi acceleration formalism. In addition, various assumptions used by analytic models attempting to describe collisionless heating through Fermi acceleration are tested and predictions from these models are compared to PIC results. Finally, it is shown that if a self-consistent calculation of heating by Fermi acceleration is performed through the PIC simulation, it yields a zero average result in accordance with the analytic calculation.

In chapter 4 the problem of collisionless heating is re-examined. It is

1.6 Research goals and outline

shown that the idea of pressure heating of the electrons by the moving sheaths can correctly interpret the heating measured by the PIC simulation. An analytic fluid model is derived, from which scaling laws are obtained and compared with the PIC simulation measurements exhibiting excellent agreement. This interpretation of collisionless heating not only illustrates the collective behaviour of the electrons, but also removes the role of the sheath edge as the source of collisionless heating.

The problem of the plasma-sheath transition is examined in chapter 5. A study of the transition through a collisional presheath with no ionisation in the case of one and two ion species is presented and comparisons are made with the existing theory. Emphasis is given to the allowed solutions to the generalised Bohm criterion in the two ion species case.

Finally, a summary of this work is presented in chapter 6. Conclusions are drawn, and the implications of this research as well as its limitations due to the implementation are discussed.

CHAPTER 2

Self-consistent treatment of the sheath through the Semi-Infinite Particle-in-Cell Simulation scheme

2.1 Introduction

The problem one has when attempting to examine the physical mechanisms behind plasma processes is simply that these are often too complicated. At a microscopic level, a plasma can be seen as an N-body problem and further analysis is impossible. At a macroscopic level, Maxwell's equations along with Boltzmann's equation provide an adequate description of the system, but then the problem is that these are hard to solve self-consistently without the use of simplifying assumptions.

An alternative approach to analytical study of the plasma is through numerical or semi-numerical models. Many different types of model fall into this category, such as equivalent-circuit models, fluid models, models solv-

2.1 Introduction

ing the Boltzmann equation directly and kinetic models [17], each with its own advantages and disadvantages. The Particle-In-Cell (PIC) simulation is nowadays one of the most commonly used kinetic schemes. The technique was initially proposed by Dawson [18] and later developed in Berkeley by Birdsall and Langdon [19–21]. A detailed description along with a historical survey of the method can be found in [14, 15, 19–21]. PIC simulations are very attractive because they provide a self-consistent¹ solution of the fields and particle dynamics from first-principles, without the need for additional assumptions. Their main disadvantage is that they are relatively expensive computationally, however the continuous development of new faster microprocessors makes it possible for them to run even on cheap home-class computers at the present time. The use of PIC simulations is two-fold: first of all, they provide insight in areas where the theory is incomplete or inaccurate. This can be most useful especially when the assumptions of the theory cannot be verified experimentally. Secondly, PIC simulations can be thought of as an extension to experiments, either providing results that are difficult to obtain experimentally, or to compare directly to experiments, enabling us to clarify the underlying mechanisms involved in some experimental measurement. This second use is currently quite limited mainly due to the complexities arising from plasma chemistry and surface processes.

Since the focus in this work is the particles' behaviour in the sheath, the standard PIC scheme has been modified in order to model only the sheath region and the plasma in its vicinity [22]. Thus it is assumed that to the left of the simulation region lies an infinite, collisional bulk plasma, while to the right a perfectly absorbing electrode exists. This modification makes it

¹In this context, the term “self-consistent” is used to stress the fact that in PIC simulations the solution of the field equations and particle motions is done simultaneously.

2.2 General PIC implementation

possible to model the sheath with increased detail compared to the standard PIC implementation at the cost of the same computational resources. In addition, the sheath is not directly coupled to the bulk processes, recreating the conditions studied in the theoretical models. The drawback, however, is that the nature of the problem requires that the boundary on the bulk-side of the plasma is treated independently, and there is a difficulty in doing so in a self-consistent way. More precisely, it is difficult to avoid creating a “source sheath” in the vicinity of the boundary which is clearly an undesirable effect since it may affect the simulated area (see for example [23]). In this chapter this problem is addressed and a method is presented to deal with the particle loading and the electric field at the boundary. A source sheath is present, but its magnitude is very small and the simulation barely affected. An alternative method of modelling a semi-infinite magnetised plasma through a PIC simulation is presented in [24].

2.2 General PIC implementation

The method is based on a purely kinetic representation of a plasma consisting of ions and electrons which are treated as individual particles moving under the influence of self-consistent electric fields. Only first principles are used (that is the particles’ equations of motion coupled by Poisson’s law) without any *ad hoc* assumptions and even with relatively few (only $10^4 - 10^5$ particles are needed for the 1-d case) particles a realistic picture of a plasma can be obtained in a few hours.

S.U.Sh.I², the implementation of the PIC model used in this work, assumes a one-dimensional planar geometry so the analysis will be restricted

²Super Universal Sheath Integrator

2.2 General PIC implementation

to that case. Therefore, each of the simulation particles is actually a charge sheet which can move inside the fixed simulation region. Each of these *super-particles* represents a large number of ‘real’ particles typically on the order of 10^{10} m⁻² particles/super-particle. Every super-particle is assigned a position x and two velocities, u_x in the x direction and u_\perp in the direction perpendicular to x . The simulation region in which the super-particles exist is divided into N_c cells resulting in a grid with $N_c + 1$ points. Only electric fields are considered, so the equation of motion for the i^{th} super-particle is

$$\frac{d^2 x_i}{dt^2} = \frac{q}{m_i} E(x_i, t), \quad (2.1)$$

with E being the electric field, which can be found from Poisson’s equation

$$\begin{aligned} \frac{d^2 \Phi(x, t)}{dx^2} &= -\frac{\rho}{\epsilon_0}, \\ E(x, t) &= -\frac{d\Phi}{dx}. \end{aligned} \quad (2.2)$$

2.2.1 Scaling of the physical quantities

In order to reduce the number of calculations involved, all physical quantities have to be rescaled to produce dimensionless variables. This is done by normalising with respect to the characteristic lengths of the system: Δx the size of each spatial cell, Δt the time integration step and \mathcal{W}_s the weight of each super-particle belonging to the s^{th} type of species. It is obvious that the quantities Δx , Δt , \mathcal{W}_s have to be chosen in order to balance between the desired accuracy and computational cost. However for the simulation to be stable and accurate, the minimal criteria that have to be respected [14] are

- $\omega_{pe} \Delta t < 0.2$,
- $\frac{\Delta x}{\lambda_D} < 0.5$,

2.2 General PIC implementation

where λ_D is the electron Debye length, so that the plasma time and space scales are properly resolved.

The fundamental physical quantities used along with their rescaled counterparts are shown in table 2.1. Other quantities such as the current or the kinetic energy can be calculated from these quantities.

Quantity	Rescaled Quantity
Time t	$\tilde{t} = \frac{t}{\Delta t}$
Position x	$\tilde{x} = \frac{x}{\Delta x}$
Velocity u	$\tilde{u} = \frac{u\Delta t}{\Delta x}$
Surface number density n_s	$\tilde{n}_s = \frac{n_s\Delta x}{\mathcal{W}_s}$
Charge q	$\tilde{q} = \frac{q}{ q_e }$
Surface charge density ρ	$\tilde{\rho} = \sum_s \frac{n_s\Delta x}{\mathcal{W}_s}$
Mass m	$\tilde{m} = \frac{m}{m_e}$

Table 2.1: *Conversion between physical quantities and PIC variables.*

2.2.2 Particle pushing

At every simulation step all particle positions and velocities are initially updated. The integration scheme used is the usual leap-frog method. In this scheme, a particle's position is known at time t , whereas its velocity is known at time $t - \frac{1}{2}\Delta t$. Thus, at the next step the position and velocity respectively

2.2 General PIC implementation

will be

$$\begin{aligned}x^{t+1} &= x^t + u^{t-\frac{1}{2}}\Delta t, \\u^{t+\frac{1}{2}} &= u^{t-\frac{1}{2}} + \frac{qE(x^t, t)}{m}\Delta t,\end{aligned}\tag{2.3}$$

where the indices $t+1$ and $t \pm \frac{1}{2}$ denote times $t + \Delta t$ and $t \pm \Delta t/2$. Expressed in the rescaled variables, equations (2.3) become

$$\begin{aligned}\tilde{x}^{t+1} &= \tilde{x}^t + \tilde{u}^{t-\frac{1}{2}}, \\ \tilde{u}^{t+\frac{1}{2}} &= \tilde{u}^{t-\frac{1}{2}} + \frac{\tilde{E}(\tilde{x}^t, t)}{\tilde{m}}.\end{aligned}\tag{2.4}$$

2.2.3 Charge assignment and electric field evaluation

Once all particle positions and velocities have been updated and new particles have been loaded, the new charge density and field evaluation take place. If the i^{th} grid point of the charge grid is considered, the value of charge assigned to it is given by

$$\tilde{\rho} = \sum_{s,k} \tilde{q}_s Q(\tilde{x}_k - x_i),\tag{2.5}$$

where s is the summation index for the particle species, k is the summation index for the super-particles and Q is the interpolation kernel given by

$$Q(x - x_i) = \begin{cases} 1 - |x - x_i| & \text{if } |x - x_i| \leq 1 \\ 0 & \text{otherwise.} \end{cases}\tag{2.6}$$

The kernel described by equation (2.6) essentially distributes the charge of every super-particle to its two nearest grid points linearly, smoothing the charge density. Different interpolation kernels, discussed in detail in [19], could be used, but they result in an increased computational cost, and it is generally accepted that the kernel described by equation (2.6) gives the best tradeoff between speed and accuracy.

2.2 General PIC implementation

Once the charge density is calculated, the potential and electric field can be calculated on the grids by the use of the finite difference equations

$$\begin{aligned}\tilde{\Phi}_{i+1} &= -\frac{\tilde{\rho}_i}{\epsilon_0} + 2\tilde{\Phi}_i - \tilde{\Phi}_{i-1} \quad \text{and} \\ \tilde{E}_i &= \frac{\tilde{\Phi}_{i+1} - \tilde{\Phi}_{i-1}}{2},\end{aligned}\tag{2.7}$$

Using equations (2.7) with appropriate boundary conditions which are discussed later in section 2.3.1, the potential and electric field on the grid points can be calculated.

2.2.4 Collisions

As has been mentioned already, plasma chemistry plays a fundamental role in plasmas. However, the full complexity of these processes cannot be fully integrated into numerical codes, mainly because this would radically increase the number of modelled species needed and therefore computational time, but also because there is lack of information (such as cross-sections) for some of the processes. A compromise is therefore usually made and most simulations include only the most basic processes such as elastic collisions, ionisation and excitation. For this work, it can be assumed that ionisation is not an important process on the sheath scale (the ionisation length being usually much larger than the sheath dimensions), and only two processes are taken into account: elastic scattering for electrons and charge exchange with neutrals for ions. The cross-section used for argon [25] is shown in figure 2.1. Due to absence of data available for helium, an average cross-section value of $\sigma = 3.0 \times 10^{-19} \text{ m}^2$, also used in the Berkeley's XPDP1 [26] code³, is utilised. In general, in PIC simulations collisions are handled through a Monte-Carlo approach: firstly, a collision probability is calculated for each of the reactant

³XPDP1 is available at <http://langmuir.eecs.berkeley.edu/>

2.3 Implementation of the single ion species model

particles depending on their velocity from a known cross-section, then a random number is produced. If it is smaller than the collision probability, the reaction occurs.

For the purposes of this research however it is desirable to produce a simulation that compares with theoretical models which generally assume a collision frequency independent of velocity. Therefore, initially

$$\nu = n_g \overline{\sigma u}, \quad (2.8)$$

is calculated, where ν is the collision frequency, n_g is the neutral gas density, σ is the energy dependent cross-section, u is the relative velocity of the participating species and the horizontal bar denotes averaging in velocity space. Then, at each simulation step, $\nu \Delta t$ randomly picked super-particles undergo a collision.

2.3 Implementation of the single ion species model

The case of a single ion species semi-infinite plasma in contact with an electrode will now be considered. It will be assumed that the plasma is isothermal such that $\nabla p = kT \nabla n$ [1] and that the electrode is perfectly absorbing. Secondary electron emission from the electrode will be ignored. The goal is to build a simulation capable of modelling a finite portion of this plasma from an arbitrary point in the bulk, up to the electrode, and drive this region with a sinusoidal rf current

$$I_{rf} = I_0 \sin(\omega_{rf} t). \quad (2.9)$$

The problem that arises is how particles should be loaded from the boundary and what should be the boundary condition for the electric field.

2.3 Implementation of the single ion species model

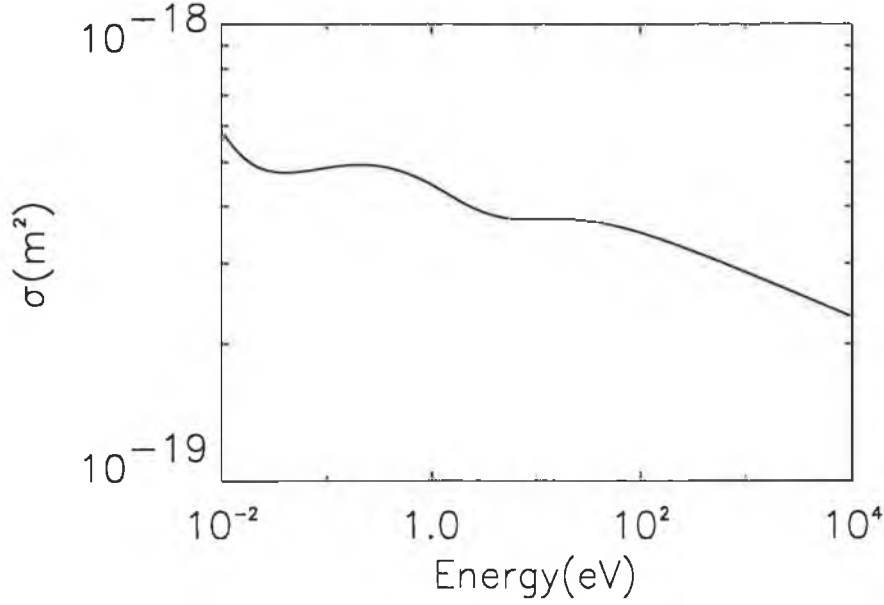


Figure 2.1: *The charge-exchange cross-section used for argon.*

In the plasma considered, the equilibrium macroscopic force equation for species s in the bulk of the plasma is written as

$$q_s n_s E - kT_s \frac{dn_s}{dx} - m_s n_s \nu_{ms} u_s = 0, \quad (2.10)$$

where ν_{ms} are the momentum transfer frequencies due to collisions of the relevant species. The flux of the ions has to be equal to that of the electrons at every point to prohibit charge from building up. Solving for the common flux $\Gamma = n_s u_s$ from equation (2.10) gives

$$\Gamma = -\frac{\mu_i D_e + \mu_e D_i}{\mu_i + \mu_e} \frac{dn}{dx} = -D_a \frac{dn}{dx}, \quad (2.11)$$

where $\mu_s = |q_s|/(m_s \nu_{ms})$ are the mobilities, and $D_s = kT_s/(m_s \nu_{ms})$ are the diffusion coefficients. D_a is the ambipolar diffusion coefficient. The density profile of the species in the absence of ionisation is linear in the bulk and the

2.3 Implementation of the single ion species model

electric field in the bulk is given by

$$E = \frac{D_i - D_e}{\mu_i + \mu_e} \frac{1}{n} \frac{dn}{dx}, \quad (2.12)$$

2.3.1 Boundary conditions and initial loading

From the above it is clear that the constant flux is the parameter that determines the behaviour of the bulk plasma boundary. That is, having set a value for the flux and determined somehow what the density n_b should be at the boundary, one can solve for the average velocity of the species at the boundary $u_b = \Gamma/n_b$. If in addition the gradient of the density is known at the boundary, the electric field at the boundary can be found by equation (2.12). The problem of how to obtain the values of the density and its gradient is discussed in section 2.3.2.

One method of determining the flux is to pick the density at the sheath edge as a control parameter for the simulation. Then, *assuming* that the ions will arrive at the sheath edge with an average velocity equal to the Bohm velocity $u_B = (kT_e/m_i)^{1/2}$ [10], the flux of the ions is determined.

In order to start the simulation, an arbitrarily chosen linear density profile is assumed. Having the density $n(x)$ at any point, ion super-particles obtained from a warm Maxwellian drifting at a velocity $u(x)$ such that $n(x)u(x) = \Gamma = \text{const}$ are loaded. Enough electron super-particles are subsequently loaded from a warm non-drifting Maxwellian to preserve quasi-neutrality. Different initial loading schemes could be implemented accounting for example for a density drop in the sheath region or for particles which have suffered collisions, but they will not be discussed here.

2.3 Implementation of the single ion species model

2.3.2 Particle loading and relaxation method

The loading of the particles at the boundary has to be done from particle distributions which are as consistent as possible with the boundary conditions. Failure to do so, leads to the creation of an artificial “source sheath” at the boundary, as for example in [23]. This happens mainly for the following reasons:

- The electric field at the bulk boundary given by equation (2.12), is a static, macroscopic approximation, which cannot be fully self-consistent with the dynamically changing particle dynamics in the boundary vicinity. Thus, the source sheath will be created in order to account for the inconsistency and correct it.
- A drifting flux which essentially does not contain particles that have recently suffered collisions is injected, whereas the “real” ion distribution at the boundary should contain a tail of low energy ions which have been affected by recent collisions⁴. This effect will persist for a length of the order of the ion mean free path, after which the ion distribution function will have relaxed (see figure 2.2).
- In the case when there is an rf component to the current drive, this should be reflected in the electron fluxes that are loaded into the simulation. Therefore, in that case, the loading of electrons has to be done from drifting warm Maxwellian fluxes.

The procedure followed in a simulation step is illustrated in the flow chart in figure 2.3. Once the simulation is started, at every step $\Gamma\Delta t/\mathcal{W}_i$ ion super-particles obtained from a warm drifting Maxwellian flux are injected from the

⁴Here, since a charge-exchange model is used, every time a collision occurs, the new ion velocities are picked randomly from a thermal ion distribution.

2.3 Implementation of the single ion species model

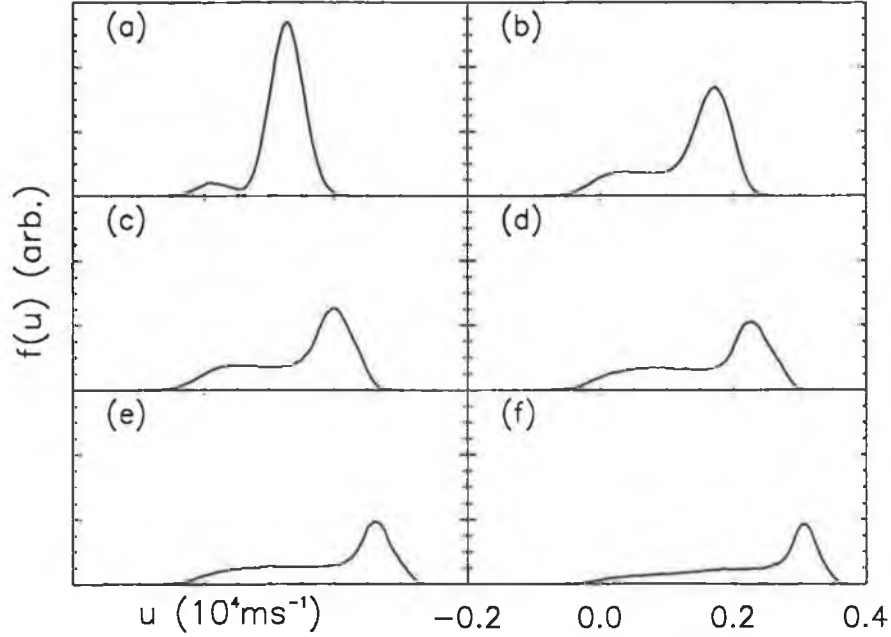


Figure 2.2: *The evolution in space of the ion velocity distribution function. At $x = 0$ the ion distribution function is composed by the super-position of the drifting Maxwellian that is injected and the ions that have recently suffered collisions. Further towards the electrode, the ion velocity distribution function relaxes to a self-consistent distribution. The positions where the distributions were gathered were (a) $x = 0.0$ cm, (b) $x = 0.33$ cm, (c) $x = 1.0$ cm, (d) $x = 1.3$ cm, (e) $x = 1.6$ cm and (f) $x = 1.9$ cm. The potential drop across the source sheath was $\Delta\Phi_{\text{source}} = 0.04$ V. Conditions: Argon gas, $I = 0$ Am⁻², $T_e = 2.57$ eV, $T_i = 0.027$ eV, $n_{\text{sheath}} \simeq 6.25 \times 10^{15}$ m⁻³, $P = 10$ mTorr.*

2.3 Implementation of the single ion species model

boundary in the simulation. The drift u_b of the flux is such that $\Gamma = n_b u_b$. Furthermore, since $m_e \ll m_i$, all rf current is carried by the electrons whilst, because $\omega_{pe} \gg \omega_{rf}$, the displacement current at the boundary is negligible and the loading of the electrons is done in the following way: taking into account how much charge $Q(t)$ has left or entered the simulation area from the bulk boundary (including the newly loaded ions) at that particular step, enough electron super-particles are injected so as to conserve the total current i.e. $(Q(t) - J_{DC}\Delta t - J_{rf}\Delta t)/e\mathcal{W}_e$ super-particles. The electron super-particles are picked from time-dependent warm drifting Maxwellian fluxes with a drift velocity equal to $u_d(t) = J_{rf}(t)/en_b$. In order to reduce the calculation time, the time-dependent fluxes are stored statically in an array.

As the simulation advances in time, the density profile is averaged in the proximity of the bulk boundary. At a certain time (usually several ion plasma periods) the average density profile near the bulk boundary vicinity is fitted by a straight line. The extrapolation of the line to the boundary yields what the new density should be at the boundary, and again knowing the flux the loading fluxes for both ions and electrons are altered accordingly so as to account for the new drift velocities. Finally the value of the electric field at the boundary is recalculated from equation (2.12). This process continues until steady state is reached. A typical result is shown in figure 2.4, where the ion density is plotted as a function of position along with a linear fit of the density in the bulk boundary vicinity. The effect of the source sheath on the density profile near the boundary is visible in the enlarged region shown in the same figure.

2.4 Implementation of the multiple ion species model

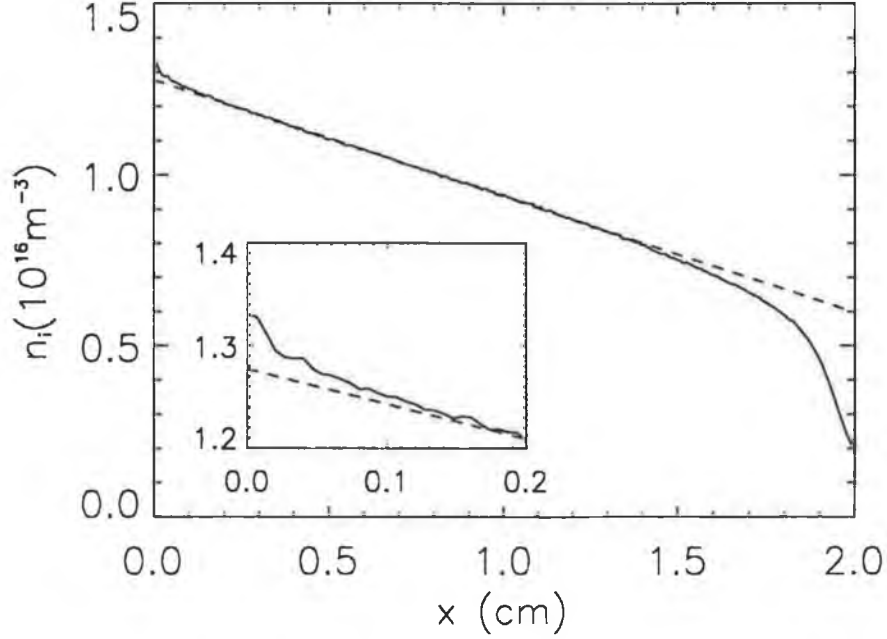


Figure 2.4: The ion density profile. The solid curve corresponds to the ion density and the dashed line is a linear fit in the bulk part of the simulation region. The effect of the source sheath is shown in the embedded graph. Conditions: Argon gas, $I = 0 \text{ Am}^{-2}$, $T_e = 2.57 \text{ eV}$, $T_i = 0.0027 \text{ eV}$, $n_{sheath} \simeq 6.25 \times 10^{15} \text{ m}^{-3}$, $P = 10 \text{ mTorr}$.

2.4 Implementation of the multiple ion species model

When more than one ion species are to be simulated, the complexity of the problem increases significantly and the analysis presented in section 2.3 has to be modified. Specifically, there does not exist a common value for the individual ion species and electron fluxes (although the sum of the ion fluxes still has to be equal to the electron flux) and therefore one cannot write equations similar to (2.11) and (2.12). In addition, although the electron

2.4 Implementation of the multiple ion species model

density profile will still be linear the same does not necessarily happen for the ion density profiles. Finally the hydrodynamic Bohm criterion in the case of multiple ion species [27] gives

$$\sum_i \frac{q_i^2 n_i}{m_i u_i^2} \geq \frac{e^2 n_e}{k T_e}, \quad (2.13)$$

which involves the individual densities of the ion species and therefore cannot be used directly to provide an estimate of the values of the individual ion fluxes. It is possible to overcome this problem by using extra equations to obtain closure. For instance, if only two ion species are considered, one can give an estimate of the floating potential, calculate the electron current and then obtain one additional equation for the total ion flux from current conservation. This problem however, does not invalidate the method, as the simulation will still converge to a “real” solution for arbitrary ion fluxes. The control over the desired values of the densities at the sheath edge in the single ion case is lost though.

Once the individual ion fluxes are specified, the procedure followed differs from the single ion case at the following points:

1. The densities of the ions at the boundary are all obtained from a 2nd order polynomial fit for each of the individual species. The electron density at the boundary is given by a linear fit.
2. As has been noted already, the non self-consistent character of the fluxes that are injected at the boundary will always create a source sheath. When more than one ion is used at low pressure the source sheath becomes more significant due to interactions between the ion species. To deal with this, the ion species are sorted by their collision frequency and the density averaging is performed for the electrons and all the ions except for the least collisional one. When the boundary is

2.4 Implementation of the multiple ion species model

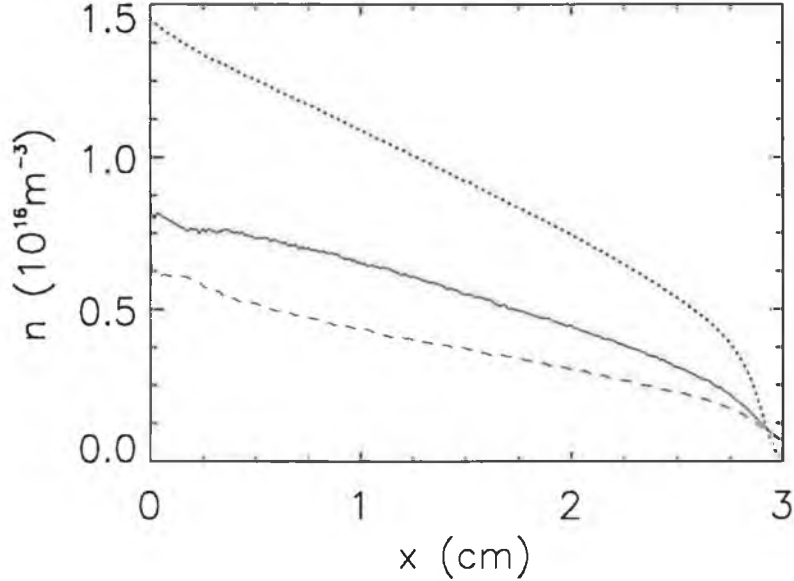


Figure 2.5: Density profiles in the two ion species case. The dotted line corresponds to the electron density and the solid and dashed curves to the argon and helium densities respectively. The potential drop across the source sheath was $\Delta\Phi_{source} = 0.03$ V. Conditions: $I = 0$ A m⁻², $T_e = 2.57$ eV, $T_i = 0.027$ eV, $\Gamma_{He} = 1.58 \times 10^{19}$ m⁻²s⁻¹, $\Gamma_{Ar} = 4.94 \times 10^{19}$ m⁻²s⁻¹, $P = 50$ mTorr.

updated, the least collisional ion species takes its value not from a fit but using a quasi-neutrality condition.

3. The ambipolar electric field at the boundary is evaluated by fitting the potential at the bulk vicinity, instead of using the values of the calculated densities and density gradients.

An example of a simulation with two ions is shown in figure 2.5. Closer inspection reveals that, as mentioned already, the electron density is linear whereas the ion densities have a slight curvature, one being concave and the

2.5 The collisionless case

other convex so as to add up to a linear profile in order to preserve quasi-neutrality. If the simulation size is increased, as we go far from the electrode, one of the ion species' density gradient goes to zero, while the other ion species density gradient approaches the electron density gradient.

2.5 The collisionless case

So far, only plasmas that have some finite collision frequency have been examined. For some classes of problems one would like to treat the plasma as completely collisionless. In that instance the previous analysis still applies but with some simplifications. The plasma structure obtained from the simulation is shown in figure 2.6. It consists of a bulk plasma region where the density remains constant, and a sheath region. A presheath region for the planar geometry cannot exist without collisions (in a cylindrical/spherical geometry, a geometrical presheath would be present). Therefore, the ions injected into the bulk region of the simulation have to already satisfy the Bohm criterion. As a result, the ion loading is done by a warm Maxwellian drifting at the Bohm velocity in the single ion case, or from warm drifting Maxwellians that satisfy the generalised Bohm criterion in the multiple ion case. Although experimental and theoretical research [28, 29] indicates that ions have quite different distributions near the sheath than the one assumed, tests have been performed with different ion temperatures without noticing significant discrepancies. This is due to the fact that the sheath structure is not sensitive to the ion distribution.

As far as the relaxation method is concerned, obviously it is not needed in this situation since the density at the boundary remains constant. This also makes the convergence faster.

2.6 Input parameters and diagnostics in the S.U.Sh.I code

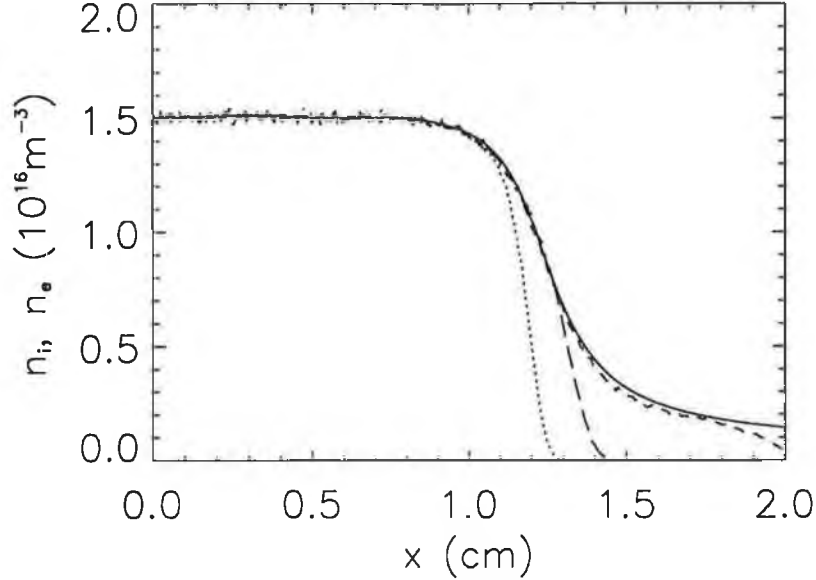


Figure 2.6: Snapshots of the ion/electron density profile in the collisionless case. The solid line represents the average ion density and the short dashed, long dashed and dotted lines the electron density at $t = 0.0 T_{rf}$, $t = 0.25 T_{rf}$ and $t = 0.5 T_{rf}$ respectively, where T_{rf} is the rf period. Conditions: Helium gas, $I_{rf} = 90 \text{ Am}^{-2}$, $\omega_{rf}/2\pi = 13.56 \text{ MHz}$, $T_e = 2.57 \text{ eV}$, $T_i = 0.0027 \text{ eV}$.

2.6 Input parameters and diagnostics in the S.U.Sh.I code

The parameters the user needs to specify in order to run a simulation are shown in table 2.2. These are stored in a file which is parsed at the time the simulation is started. Additionally, in the same file, the diagnostics that the user would like to access are indicated. The most useful diagnostics that are built-in to the simulation are shown in table 2.6. These diagnostics are resolved in both time and space and in order to improve accuracy,

2.6 Input parameters and diagnostics in the S.U.Sh.I code

General parameters		Species parameters		Drive parameters	
l	Simulation length	m_s	Mass	I_{rf}	rf current amp.
N_c	Number of cells	q_s	Charge	f_{rf}	rf frequency
Δt	Time-step	Γ_s	Particle flux (ions)	ϕ	rf phase offset
N_{tp}	Time-steps/period	T_s	Bulk temperature	I_{DC}	DC offset
N_t	Number of steps	\mathcal{W}_s	Super-particle weight		

Table 2.2: *Input parameters for the S.U.Sh.I code.*

averaging over the rf cycles takes place (with the exception of course of the phase-space diagnostic) once convergence has occurred and the simulation has reached equilibrium. In order to facilitate user interaction, all diagnostics can also be displayed graphically in real-time on computers capable of displaying OpenGL graphics or through the XGrafix library⁵ otherwise. For the velocity distribution diagnostic, the user has the choice to specify in which temporal and spatial interval he would like the distribution to be collected.

General diagnostics	Species diagnostics
Potential	Density
Electric field	Phase-space
Displacement current	Convection current
Potential Energy	Velocity distribution
	Phase-space $(x - u_x)$
	Temperature
	$f(u)$ moments

Table 2.3: *Diagnostics in S.U.Sh.I.*

⁵The XGrafix library is available at <http://langmuir.eecs.Berkeley.edu/>

2.7 Summary

Summarising, a method based on the PIC scheme for modelling a semi-infinite plasma in contact with an electrode has been presented. The advantages of this implementation are two-fold: firstly it makes it possible to simulate the sheath structure and the plasma in its vicinity independently of the rest of the plasma, achieving increased diagnostic detail that would be very expensive computationally in a generic PIC simulation. Secondly, conditions that are usually used by analytic models can be imposed so that the validity of these models can be tested.

Due to the nature of the problem, a source sheath is unavoidably created at the boundary. Through self-consistent loading of the particles and boundary field evaluation, the effect of the source sheath is minimised.

In the context of the present work, it has been assumed that ionisation is not an important process on the sheath scale and a collision model involving only charge-exchange for the ions and elastic scattering for the electrons is used. It is also possible to treat the plasma as collisionless, in which case the method is simplified.

Finally, simulations with only one or two different ion species will be presented and only in planar geometry. However, the generalisation of the method to cylindrical and spherical geometries is possible, and more ion species could be included.

CHAPTER 3

Collisionless electron heating by capacitive rf plasma sheaths through the Fermi acceleration mechanism.

One of the reasons why the understanding of plasma sheaths and electron dynamics in their vicinity is of crucial importance is the fact that the discharge maintenance mechanism is associated with this region under low-pressure conditions. This is because, in contrast to the high pressure regime where the plasma is sustained by Ohmically heated electrons, in the low-pressure regime electrons are heated by the spatially inhomogeneous rf fields that are present in the sheaths.

In order to clarify this matter, let us consider an ensemble of electrons with density per unit volume n . If u is the average velocity of the electrons, J the current density and E the strength of a periodic electric field, these

are related by

$$\begin{aligned} J &= enu, \\ J &= \sigma_p E, \end{aligned} \tag{3.1}$$

where $\sigma_p = e^2 n / m(\nu_m + j\omega)$ is the local conductivity and ν_m the collision frequency for momentum transfer. The power transfer per unit volume is then given by

$$P = \frac{1}{2} \text{Re}(JE^*) = \frac{1}{2} |J|^2 \text{Re}(\sigma_p^{-1}). \tag{3.2}$$

By inspecting equation (3.1), it can be seen that in the absence of collisions ($\nu_m = 0$), the average electron velocity (or current) phase is offset by $\pi/2$ with respect to the electric field. Therefore, the energy exchange between the field and the electrons, averaged over a whole cycle of the periodic field, is zero. In contrast, in the presence of collisions ($\nu_m > 0$), individual electrons lose phase coherence with the field every time a collision occurs, and this gives rise to heating.

As was first demonstrated by Landau [30], in the absence of collisions and in the presence of a field with spatial variation, the electrons can sample the field's inhomogeneity provided they have sufficient thermal energy. In that case, the current density at some point in the plasma is not defined by the electric field at that point, but rather by an integrated effect over its neighbourhood. What follows is that phase coherence can be lost since the field "seen" by an electron is non-periodic even if the field itself is periodic. The loss of phase coherence can then allow, under certain conditions, for heating to occur.

It is not difficult to see how the above argument applies to capacitive rf discharges. Roughly speaking, the discharge can be separated in two regions, the bulk and the sheath region. In the bulk region the electric field is mainly

3.2 Fermi acceleration applied to capacitive rf discharges

3.2.1 Experimental evidence of collisionless heating

Most of the early experimental investigations linked to collisionless heating are due to Godyak and co-workers and are summarised in [3]. In a capacitive, parallel plate mercury vapour discharge which was symmetrically driven in a frequency range between 40 MHz and 100 MHz, Godyak *et al.* [52] and Godyak and Popov [53] performed measurements of the current-voltage characteristic from which they evaluated the effective collision frequency. Their results established that as the pressure goes down, the effective collision frequency levels off to some finite value instead of dropping linearly as would be the case if only Ohmic heating was present. The same was done by Popov and Godyak in [54], but this time measuring the rf power absorbed directly and using these measurements to calculate the effective collision frequency. In all those experiments, the power deposition to the ions at the sheath regions was neglected in the analysis, although it is usually significant in the parameter range considered.

For an argon gas in an approximately plane configuration at a fixed frequency of 13.56 MHz and for a pressure range varying from 3 mTorr to 3 Torr, Godyak and Piejak [55] and Godyak *et al.* [56, 57] performed measurements of the current, voltage, plasma density, electron energy distribution function (EEDF), ion current to the electrodes and DC bias voltage in the rf sheath. By averaging $V_{rf}I_{rf}$ over the rf period, the total power deposition P_{tot} was calculated, whereas the power deposition to the ions P_{ions} was determined from the sheath DC bias voltage and the ion current. The power absorption P_{ohm} by the electrons due to Ohmic heating was estimated by the plasma conductivity, and it was compared to the total power deposited to the electrons $P_{el} = P_{tot} - P_{ions}$. It was found that at pressures greater than 0.1 Torr, $P_{el}/P_{ohm} \approx 1$, i.e. all heating is due to collisions, whereas at the lowest pres-

3.1 Fermi acceleration

constituted by the ambipolar and rf fields and has a low strength. Although it can change the drift velocity and density of the electrons and maintain quasi-neutrality, it contributes little to heating. On the other hand, in the sheath region, the electric fields which develop have a strong spatial and temporal dependence and are significantly larger than the bulk plasma fields. It is therefore in the sheath region that collisionless heating is expected to appear, and that is indeed the case as shown by both the experimental results and the simulations that are discussed in this chapter.

3.1 Fermi acceleration

In order to investigate the dynamics of the electron interaction with these fields, it has been suggested that the model of Fermi acceleration, which was utilised initially by Fermi to give an explanation on the origin of cosmic radiation [31], can be used. In this model, a particle which bounces elastically between a fixed and an oscillating wall or two oscillating walls (see figure 3.1) is considered. Assuming that the collisions between the particle and the walls are elastic, the velocity u_r which the particle will have after a collision is

$$u_r = -u_i + 2u_w, \quad (3.3)$$

where u_i is the incident velocity of the particle and u_w the velocity of the wall at the time of the collision. It can be easily seen from equation (3.3) that, depending on whether the particle and the wall collide while moving towards the same or opposite direction, the particle loses or gains energy respectively. According to Fermi's argument, because head-on collisions are more probable, the particle will on average gain energy, provided there is no phase correlation between the collisions.

3.1 Fermi acceleration

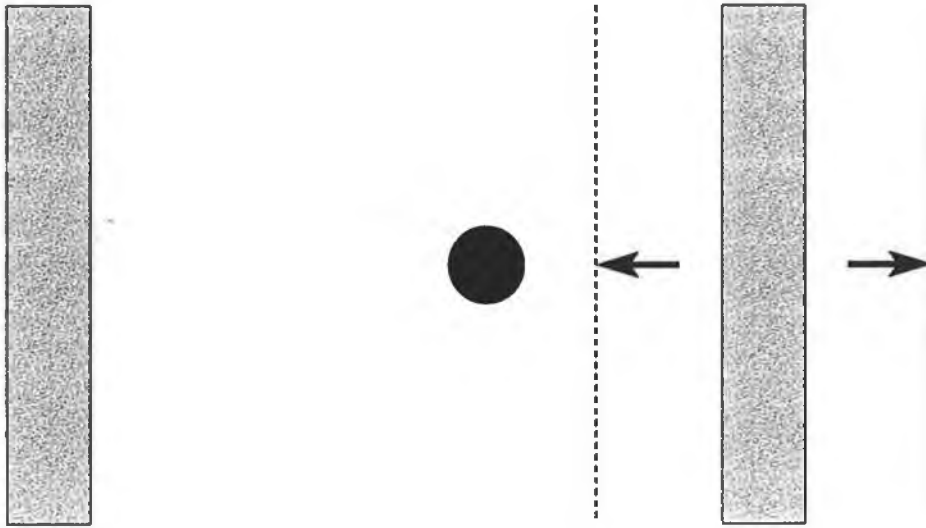


Figure 3.1: *Illustration of the Fermi model.*

This model has served as a paradigm in physics and has been applied in many different fields. A lot of the initial work was focused on finding the conditions under which phase coherence could be lost using Hamiltonian mappings [32]. Zaslavskii and Chirikov [33] analysed the motion of particles which collide with objects whose motion is completely deterministic (a sawtooth wall velocity was assumed), and derived conditions for the stochastic behaviour of a one-dimensional system. Later, Lieberman and Lichtenberg [34] introduced a simplified Hamiltonian mapping in which a wall that was fixed in space but at the same time could transfer momentum. They went on to show that there are parameter regions where the random-phase assumption holds and the particle motion is chaotic, and regions where organised islands exist and the motion is phase-correlated. In addition, it was shown that the particle motion in the chaotic region could be described by a Fokker-Planck equation. A comparison of some of these models in the context of the ergodic hypothesis and KAM stability appeared in [35]. Thorough

3.2 Fermi acceleration applied to capacitive rf discharges

reviews of the early work on Fermi acceleration can be found in [4, 36, 37].

3.2 Fermi acceleration applied to capacitive rf discharges

Initially, the idea of electron interaction with rf fields was considered by Gabor *et al.* [38] in order to resolve the “Langmuir paradox”: probe measurements in a low pressure mercury arc indicated that the electrons could be described by a Maxwellian energy distribution. This was an unexpected result considering that in the pressure range where the measurements were taken the electron mean free path largely exceeded the tube dimensions. The measurements were explained by the presence of plasma oscillations near the DC sheath edge dispersing the electron velocities. Considering a DC potential with a small rf perturbation, Pavkovich and Kino [39] found a numerical solution of the appropriate Boltzmann equation showing also that there is rf energy absorption due to the electron-wave interaction.

In the context of radio-frequency plasma sheaths, stochastic heating¹ through Fermi acceleration, was first discussed in the early 1960’s by Mayer [11]. Godyak [40] was the first to link Fermi acceleration directly with collisionless heating in capacitive discharges. In that original model, he used a small sinusoidal signal on a DC parabolic potential, and assuming that the electrons were colliding elastically with the oscillating field, he calculated the

¹In the literature, one finds several different terms such as *stochastic heating*, *wave riding* and *sheath heating* describing essentially the same phenomenon: heating of electrons by the oscillating sheaths through Fermi acceleration. Because the use of different nomenclature is confusing, the term “stochastic heating” will be used to uniquely denote this mechanism. The term “sheath heating” will be used to denote heating occurring in the sheath regions by *any* mechanism.

3.2 Fermi acceleration applied to capacitive rf discharges

power deposited to the plasma. Further work was done by Akhiezer and Bakai [41] who used a simplified Fermi map model to calculate the power deposition and by Alanakyan [42] who studied the interaction of a hot electron distribution with the rf field and found that the distribution function follows a power law in energy space. By assuming a sinusoidal movement of the sheath, utilising the Fermi acceleration mechanism and applying physical constraints, Goedde *et al.* [43] obtained a partially self-consistent model of an rf discharge. The electron energy distribution function was found to be of the form $f(E) \propto E^{\frac{1}{2}}$. Lieberman [7] proposed an almost fully self-consistent model of the sheath and calculated the power deposition due to the Fermi acceleration mechanism. This model is of particular importance to this work, because it provides the most complete basis for comparison and it is reviewed in appendix A.

Finally, one of the alternative possibilities that have been proposed to describe and evaluate stochastic heating is based on the non-local solution of the time and space dependent Boltzmann equation by reducing it to a zero-dimensional time-space independent equation [44]. This equation involves the time-space averaged energy diffusion coefficient $D(E)$, which provides all information needed for the calculation of the power deposition to electrons. Using this approach, Smirnov and Kaganovich among others, have treated rf discharges [45, 46] and stochastic heating specifically [47–49]. The processes that lead to phase randomisation and energy diffusion due to non-linear effects have been investigated in [37, 50] and classified by Kaganovich *et al.* in [48]. In another approach, Aliev *et al.* [51] described electron heating as a process similar to Landau damping involving particle-wave interactions of resonant electrons.

3.2 Fermi acceleration applied to capacitive rf discharges

sure value (3 mTorr), collisionless power deposition could be thousands of times larger than the Ohmic power deposition.

Finally, a dramatic change in the shape of the EEDF when the transition from collision-dominated heating to collisionless heating occurs by changing the pressure was reported by Godyak *et al.* [57]. It was observed that in the Ohmic heating regime the EEDF was Druyvensteyn-like, whereas in the collisionless heating regime, the EEDF could be well approximated by a bi-Maxwellian distribution with a hot and a cold electron population. The same type of transition was observed by Buddemeier *et al.* [58] while keeping the pressure constant at $P = 67.4$ mTorr and varying the rf potential from 30 volts to about 100 volts.

3.2.2 Simulations

There has been a significant contribution to the subject by research based on simulations, either dealing with collisionless heating in general, or specifically with collisionless heating through Fermi acceleration. Vahedi *et al.* [21] compared EEDFs obtained by PIC simulations to the experimental results reported by Godyak and Piejak [55]. Good agreement was found, and the transition of the shape of the EEDF from Druyvensteyn-like to bi-Maxwellian was also observed. Surendra *et al.* [59] performed PIC simulations in a model gas based on helium and showed that even if the secondary electron emission coefficient is set to zero, high-energy electrons which acquire their energy near the plasma-sheath interface propagate through the discharge. Surendra and Dalvie [60] also calculated the terms in the moment equations derived from the Boltzmann equation explicitly, using a PIC simulation. Their results indicated that electron heating can be separated into two terms, attributed to Ohmic heating and pressure work respectively. Vender and Boswell [61]

3.2 Fermi acceleration applied to capacitive rf discharges

showed using a PIC simulation that the intensity of the ionisation processes which is related to how energetic electrons are, is higher near the sheath while the sheath expands and lower when it collapses, following the presence of hot electrons. The importance of electron inertia, power losses to the electrodes, and the lack of self-consistency in models dealing with electron-sheath interactions were pointed out by the same authors in [62]. Using a semi-infinite PIC simulation very similar to the one constructed here, Surendra and Vender [23] studied heating in a collisionless sheath and provided scalings using the ratio of the drift velocity to the thermal velocity of the electrons as a parameter. A comprehensive comparison of the results obtained from various types of models including kinetic, hybrid and fluid simulations with the experimental results of Godyak was undertaken by Surendra [63]. Finally, Monte-Carlo simulations assuming an analytic form for the electric field with which the electrons interact and calculating power deposition have been performed by Kushner [64] and by Wendt and Hitchon [65].

Summarising, in capacitive rf discharges the Fermi acceleration paradigm has been applied as follows: electrons with a temperature $T_e \approx 3$ eV travel freely in the bulk, until they reach the moving fronts of the sheath electric fields, where they undergo reflection. Since the electron temperature is $T_e \approx 3$ eV and the fields are of the order of hundreds or thousand of volts, the electrons can be seen as the “particles” and the fields as the “walls”, and therefore the collision can be considered elastic. This approximation is referred to in the literature as the “Hard Wall Approximation”. Provided there is some phase randomisation mechanism, such as collisions or field fluctuations in the bulk, the electrons can in principle gain energy in an average sense.

3.3 Calculation of the power deposition due to Fermi acceleration

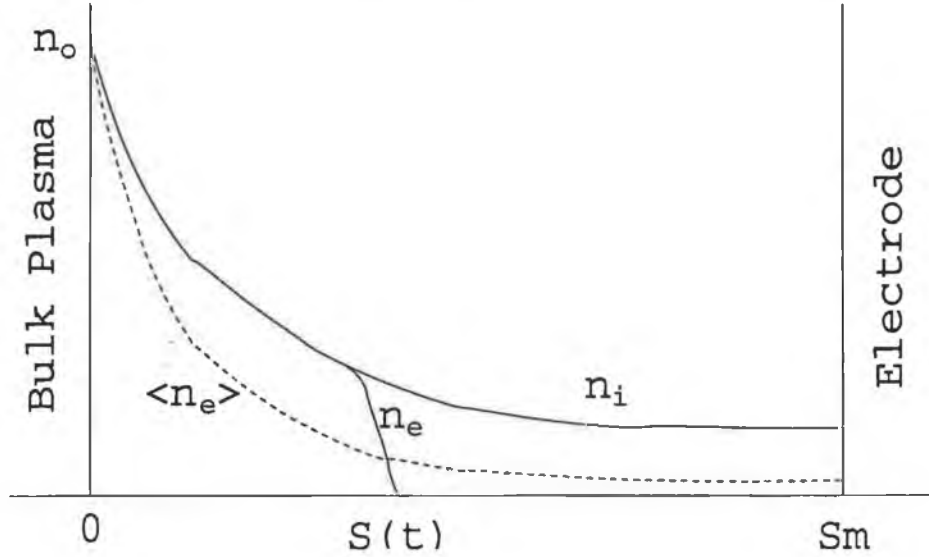


Figure 3.2: *The structure of the rf sheath.*

3.3 Calculation of the power deposition due to Fermi acceleration

Let us now proceed by calculating the power deposition to the electrons from the Fermi acceleration mechanism analytically, following the formalism of Lieberman [7]. A collisionless sheath with a particle density $n = n_0$ at the plasma-sheath boundary is assumed as in figure 3.2. The ion density falls as we approach the electrode because the ions are accelerated. The electron density follows the ion density so that quasi-neutrality is preserved, until the instantaneous sheath edge is reached, where it is assumed that the electron density falls rapidly to zero. An electron that collides with the sheath electric field, assuming the collision is elastic, will be reflected with a velocity

$$u_r = -u + 2u_s, \quad (3.4)$$

where u is its incident velocity and u_s is the velocity of the sheath front. The energy gain or loss will be equal to the difference in its kinetic energy after

3.3 Calculation of the power deposition due to Fermi acceleration

and before the collision, i.e.,

$$\Delta E = \frac{1}{2} m_e (u_s^2 - u^2) = 2m_e u_s (u_s - u). \quad (3.5)$$

Considering now the whole electron distribution function and keeping in mind that the electrons that arrive at the sheath edge are those that have a velocity higher than the sheath velocity, the instantaneous power deposition $S_{FA}(t)$ is equal to

$$\begin{aligned} S_{FA}(t) &= \int_{u_s}^{\infty} (u - u_s) f_s(u, t) \Delta E \, du \\ &= -2m \int_{u_s}^{\infty} u_s (u - u_s)^2 f_s(u, t) \, du, \end{aligned} \quad (3.6)$$

where f_s is the electron distribution function at the sheath edge. It is plausible to approximate the electron distribution function, at the sheath edge by a drifting Maxwellian

$$f(u) = n_e \left(\frac{m}{2\pi kT} \right)^{\frac{1}{2}} \exp \left[-\frac{m(u - u_d)^2}{2kT} \right], \quad (3.7)$$

where u_d and T are the electron drift velocity at the sheath edge and temperature respectively.

Considering now current conservation at the sheath edge, note that in the sheath region where the electron density is non-zero (i.e. from the ion sheath edge or Bohm point, up to the electron sheath edge), the rf electric fields are negligible and all current is carried by electrons. In contrast, in the region starting from the electron sheath edge and up to the electrode, there are no electrons and current is purely displacement current, due to the field variations. The ion current can be considered negligible. Therefore, for a sinusoidal current-driven sheath, by equating convection current to displacement current at the electron sheath edge, current conservation gives

$$-en_e u_d = -en_i u_s = J_0 \sin \omega t, \quad (3.8)$$

3.3 Calculation of the power deposition due to Fermi acceleration

where n_i is the ion density at the sheath edge. Since quasi-neutrality still holds at the electron sheath edge, u_d has to be equal to u_s , that is, the electrons must be drifting with a velocity equal to the sheath velocity. So, equation (3.6) becomes

$$\begin{aligned} S_{FA}(t) &= -2mu_s \int_0^\infty V^2 g_s(V) dV \\ &= -n_s u_s kT \\ &= \frac{J_0 kT}{e} \sin \omega t, \end{aligned} \quad (3.9)$$

where a change of variables has been performed by setting $V = u - u_s$ and $g_s(V)$ is the Maxwellian distribution function with zero drift. It is clear from equation (3.9) that although the instantaneous power is non-zero the power over an entire rf cycle averages to zero.

In contrast to the above statement, Lieberman, who first presented the above calculation [7], has obtained a positive net power deposition result, by assuming $f_s = g_s(u - u_0)$ instead of $f_s = g_s(u - u_s)$ where u_0 is the electron drift velocity at the Bohm point. With that assumption, and utilising the analytic expression for the sheath velocity calculated in [7], $\langle S_{FA}(t) \rangle$ becomes

$$\langle S_{FA} \rangle = \frac{3\pi}{32} H m n_0 \bar{u} u_0^2, \quad (3.10)$$

where $\bar{u} = (8kT/\pi m)^{1/2}$ is the average electron speed, and $H = J_0^2/(\pi\epsilon_0 kT\omega^2 n_0)$ is a dimensionless parameter. Taking u_0 to be the drift velocity of the electrons at the sheath edge violates the electron flux continuity and therefore current conservation: for the flux to be conserved we need $n_s u_s = n_e(x) u_e(x) = n_0 v_0$ everywhere between the Bohm point and the electron sheath edge. Since the electron density drops as we approach the electron sheath edge, it is apparent that u_s has to increase in order to satisfy continuity, and therefore Lieberman's solution is inconsistent. This was first noted

3.4 The quasi-neutrality field

by Surendra and Dalvie [60] who also remarked that using the correct drift velocity for the electrons yields zero net heating as has been shown above.

An alternative way of showing that there is no power deposition to the electrons due to the Fermi acceleration mechanism, independently of the electron distribution function, is the following: as in equation (3.6) the power deposition is

$$\begin{aligned} S_{FA}(t) &= \int_{u_s}^{\infty} (u - u_s) f_s(u, t) \Delta E \, du \\ &= \int_{u_s}^{\infty} \frac{1}{2} m (u_r^2 - u^2) (u - u_s) f(u) \, du. \end{aligned} \quad (3.11)$$

Now, expressing the incident velocity as the sum of its drift and thermal components u_d and u' respectively, equation (3.11) gives

$$\begin{aligned} S_{FA} = -2m \left\{ \int_{u_s - u_d}^{\infty} (u_s - u_d)(u' + u_d - u_s)^2 g(u') \, du' \right. \\ \left. + \int_{u_s - u_d}^{\infty} u_d(u' + u_d - u_s)^2 g(u') \, du' \right\}, \end{aligned} \quad (3.12)$$

where again $g(u') = g(u - u_d)$ is the undisplaced distribution function. The first integral in equation (3.12) which represents the rate of change of the thermal energy of the distribution vanishes due to current conservation ($u_d = u_s$), whereas the second one which does not vanish merely maintains the drift energy and averages to zero over an rf cycle. Therefore, the conclusion again is that there can be no heating due to Fermi acceleration.

3.4 The quasi-neutrality field

In Lieberman's treatment of the collisionless heating effect, individual electron trajectories are assumed to be unaffected by the electric field (which will be referred to as the "quasi-neutrality field" hereafter) that necessarily exists

3.4 The quasi-neutrality field

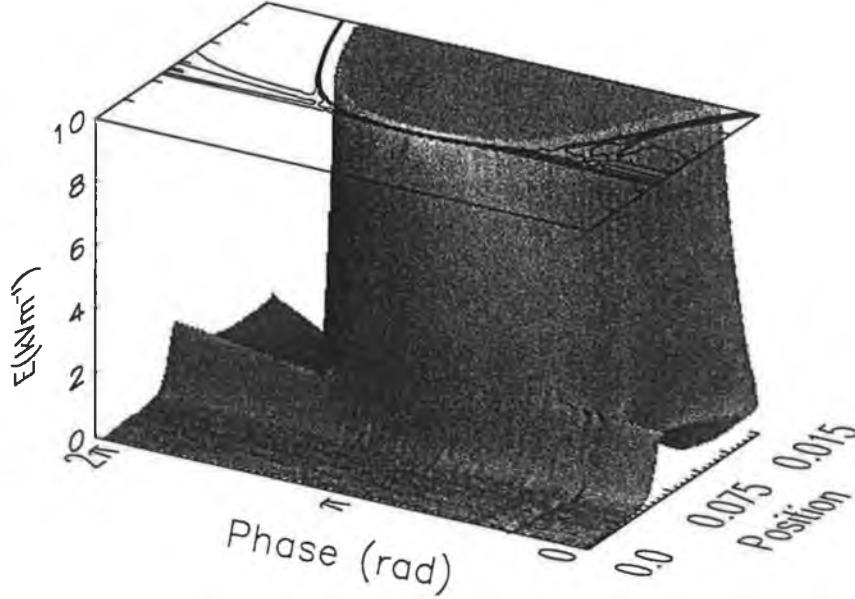


Figure 3.3: Detail of the electric field in the sheath showing the quasi-neutrality field. The field has been clipped at the value of 10 kV m^{-1} . The maximum of the field when the sheath is fully expanded is at $E \simeq 1.1 \times 10^5 \text{ V m}^{-1}$. Conditions: $I_{rf} = 60 \text{ A m}^{-2}$, $n_e = 5.0 \times 10^{15} \text{ m}^{-3}$, $\omega_{rf}/2\pi = 13.56 \text{ MHz}$, $T_e = 2.57 \text{ eV}$.

between the bulk plasma and the instantaneous sheath edge, and which preserves quasi-neutrality in that region and maintains the electron flux. The quasi-neutrality field (shown in figure 3.3), although small compared to the sheath field, causes a potential difference which is of the order of the electron temperature and therefore affects the incident distribution that arrives at the sheath edge. Lieberman includes the quasi-neutrality field in his model only implicitly via his assumption of Boltzmann equilibrium for the electron fluid. This field has been explored analytically in [47] but the resulting equations were not solved.

A first-order time-independent approximation can be obtained if it is as-

3.4 The quasi-neutrality field

sumed that electrons are in Boltzmann equilibrium with the quasi-neutrality field so that

$$n_e(x) = n_0 \exp(V(x)/T_e), \quad (3.13)$$

where T_e is the electron temperature measured in volts. From quasi-neutrality $n_e = n_i$, and taking the potential at the bulk to be zero, one can solve for the potential $V(x)$ and differentiate to obtain the field strength

$$E_{qm}(x) = -T_e \frac{d}{dx} \left(\ln \frac{n_i(x)}{n_0} \right). \quad (3.14)$$

To emphasise the argument for the necessity of the quasi-neutrality field, a direct comparison of results obtained from a Monte-Carlo simulation where only the sheath electric field as calculated by Lieberman is present, and a modification of it with the quasi-neutrality field included is presented [66, 67]. The numerical simulation used is based on following individual electron trajectories as they interact with the model sheath electric field. A similar approach, using a simpler model, can be found in [65]. The loading process (particles entering the sheath from the bulk plasma) assumes a one-dimensional time-dependent drifting Maxwellian flux. At a random phase a particle is given a velocity from the flux using a Monte-Carlo approach. The equations of motion for the particle are then integrated numerically with the appropriate boundary conditions inside the sheath region, using a Runge-Kutta 5th order integration scheme. The electric field strength is interpolated using dense tabulated data for different phases of the rf cycle and different positions in the sheath. While the particle remains inside the sheath region, its velocity and position are allocated to grids. By averaging over a large number of particles ($\simeq 10^5$) and properly rescaling these grids all standard diagnostics can be obtained.

As can be seen in figure 3.4, gross distortion of the electron density profile

3.4 The quasi-neutrality field

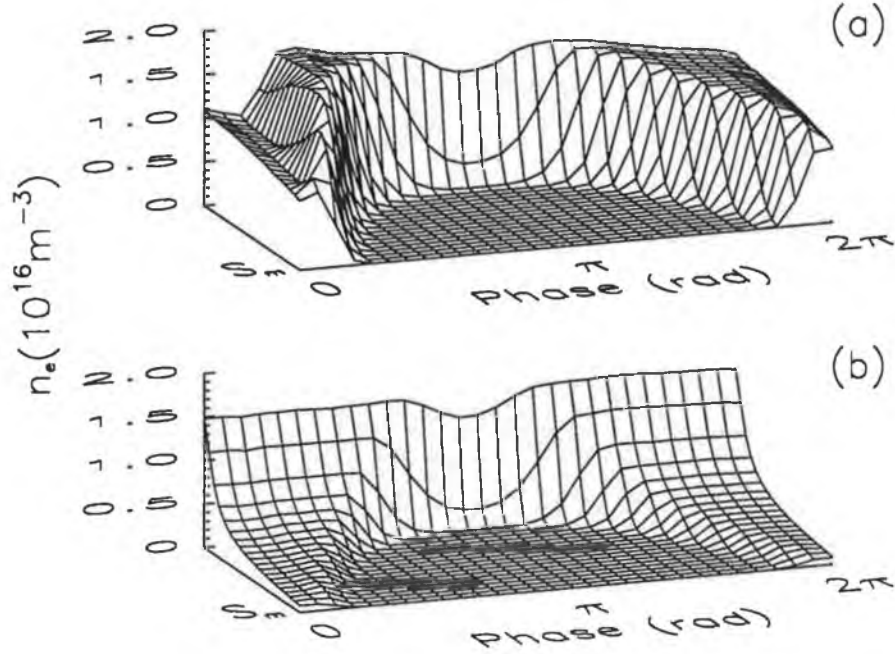


Figure 3.4: *Electron density profile from the Monte-Carlo simulation without (a) and with (b) the quasi-neutrality field. See also figure 3.2. $n_e = 1.5 \times 10^{16} \text{ m}^{-3}$ in the bulk.*

occurs in the absence of the quasi-neutrality field, leading to violation of current conservation. However, due to the non self-consistent character of the model, absolute current conservation cannot be achieved even though the inclusion of the quasi-neutrality field improves the density and current profiles. The importance of current conservation when calculating the power deposition due to Fermi acceleration has already been stressed and these remarks are made only to emphasise the need for a self-consistent approach to resolve the issue: in other words, in order to establish whether the heating observed experimentally and by simulations is due to the Fermi acceleration mechanism or not, one would like to perform the calculation described by equation (3.6) without prescribing an analytic form for the quantities involved. That

3.5 Power deposition into the plasma

is, recalculate equation (3.6) and its average using a self-consistent distribution function f_s together with a self-consistent description of the sheath velocity u_s . The simulation scheme that has been presented in chapter 2 in its collisionless version is ideal for this type of calculation, since all the quantities obtained are self-consistent and at the same time the simulation closely resembles the sheath structure assumed by theoretical models, providing the basis for a valid comparison.

3.5 Power deposition into the plasma

It is desirable to compare at this point the power deposition as calculated by the PIC simulation with the values predicted by Lieberman's model. The average power per unit area deposited into the plasma by the oscillating sheaths can be calculated directly from the PIC simulation by

$$\bar{P} = \frac{1}{T} \int_0^{s_m} \int_0^T J_e E \, dt \, dx, \quad (3.15)$$

where E is the electric field and J_e is the electron current density. Since the analytic model does not account for electron loss, in order for the comparison to be made, the contribution to the power per unit area by the electrons which are being lost at the electrode has to be excluded: every escaping electron has contributed $1/2 m_e u_i^2 - 1/2 m_e u_f^2$ of energy, where u_i is its initial velocity when it enters the simulation area from the bulk boundary and u_f is its velocity when it exits at the electrode. Since the potential is taken to be zero at the bulk side, the energy removed by the electron is equal to $q_e V(t)$ where $V(t)$ is the instantaneous potential of the electrode. Averaging this quantity over many rf cycles, $P_{loss}(t)$, the power per unit area lost due to electron loss as a function of phase is obtained.

3.5 Power deposition into the plasma

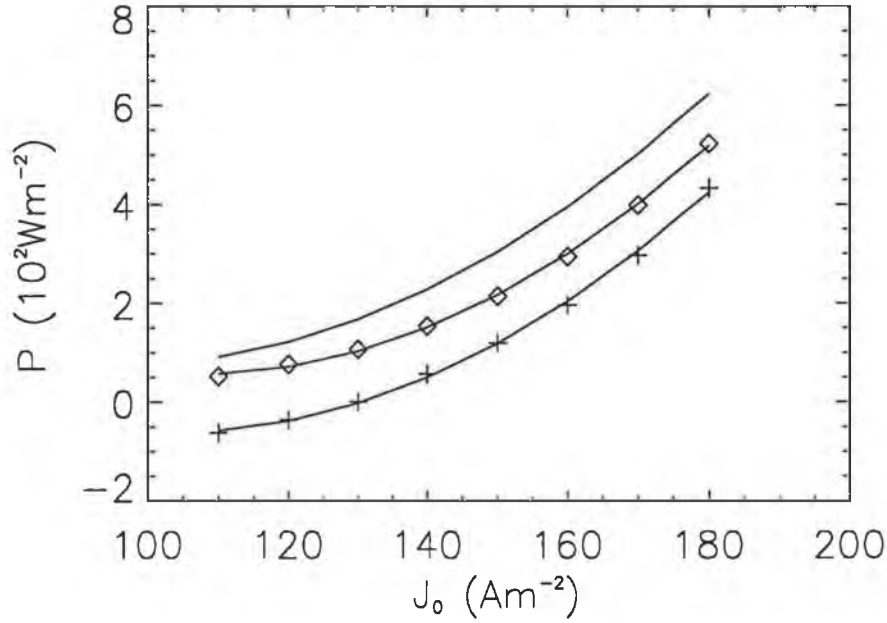


Figure 3.5: Average power per unit area scaling with current. The upper solid line corresponds to Lieberman's prediction, + to \bar{P} from the simulation and \diamond to $\bar{P} - P_{\text{loss}}$. Conditions: $n_e = 1.5 \times 10^{16} \text{ m}^{-3}$, $\omega_{\text{rf}}/2\pi = 13.56 \text{ MHz}$, $T_e = 2.57 \text{ eV}$.

In figure 3.5 the average power per unit area deposited into the plasma as a function of the current drive is shown. The PIC results scale similarly to Lieberman's calculation, but Lieberman's model slightly overestimates the power deposition, even if the electron loss contribution is removed. In figure 3.6 the average power per unit area scaling with frequency for a constant rf voltage as predicted theoretically by stochastic heating theories ($\bar{P} \propto \omega^2$) is compared with the results obtained from the simulation. In order to keep the voltage across the sheath constant in these simulations the current drive was varied until the voltage was stabilised at the value of $V_{\text{rf}} = (400 \pm 5) V_{p-p}$. The predicted scaling does not agree with the results obtained from the PIC simulation. However, it has to be noted that Lieberman's model assump-

3.5 Power deposition into the plasma

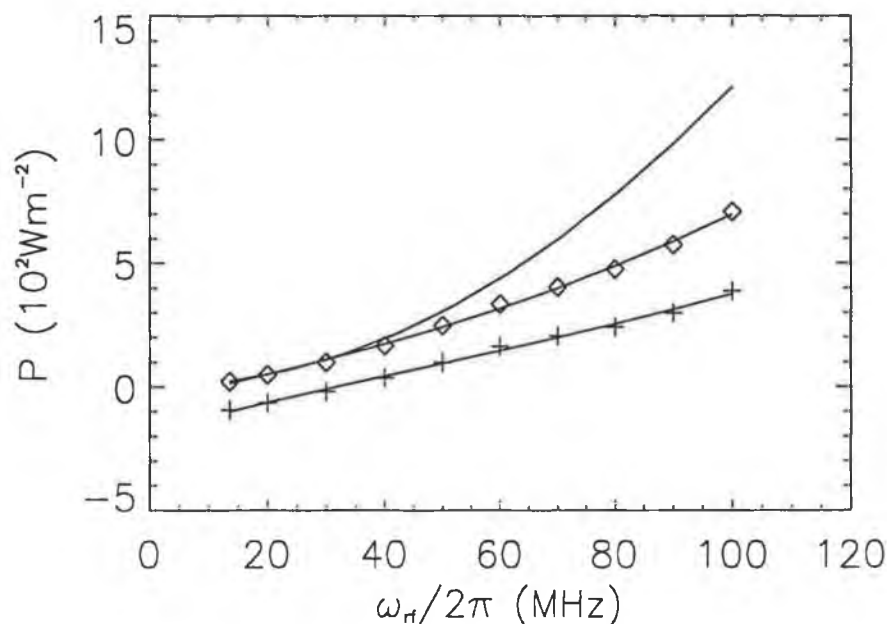


Figure 3.6: Average power per unit area scaling with frequency. The upper solid line corresponds to Lieberman's prediction, + to \bar{P} from the simulation and o to $\bar{P} - P_{loss}$. Conditions: $V_{rf} = 400$ V_{p-p}, $n_e = 1.5 \times 10^{16}$ m⁻³, $T_e = 2.57$ eV.

tions are not valid as the driving frequency approaches the electron plasma frequency and that at the lowest frequency range shown in figure 3.6 where the model's performance is best, Lieberman's prediction and the PIC simulation are in good agreement. It also has to be noted, as reported previously [12, 13], that increasing the frequency leads to an injection into the plasma of a fast electron current due to a pressure wave developing as the electron fluid is compressed and decompressed by the sheath. This current imposes a small electric field in the bulk side of the plasma which leads to a negative $J_e E$ in the bulk. Therefore the integration over $J_e E$ is performed from the point where the sheath begins. Performing the integration for the whole simulation area only makes the disagreement with the theoretical re-

3.5 Power deposition into the plasma

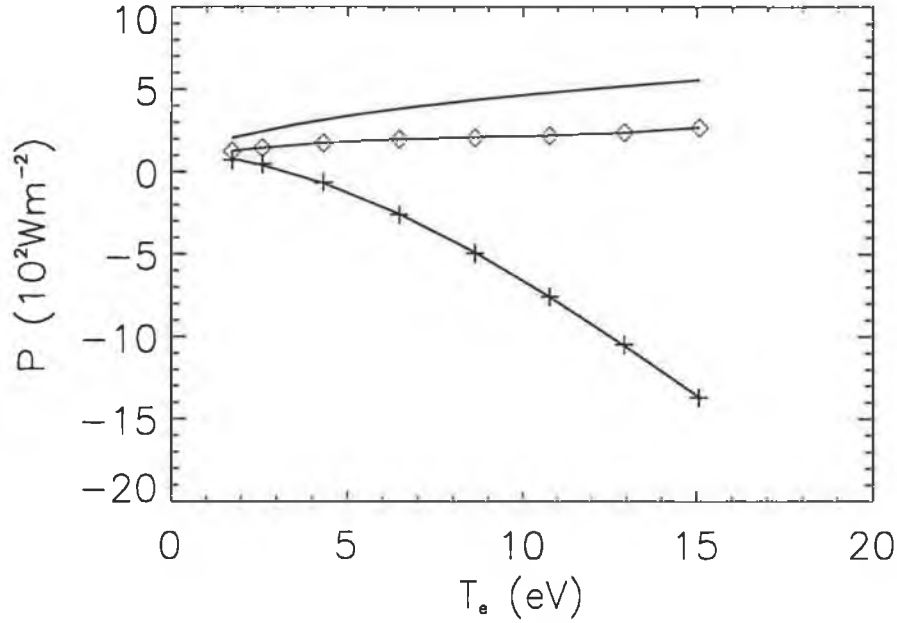


Figure 3.7: Average power per unit area scaling with temperature. The upper solid line corresponds to Lieberman's prediction, + to \bar{P} from the simulation and \diamond to $\bar{P} - P_{loss}$. Conditions: $V_{rf} = 2000 V_{p-p}$, $n_e = 1.5 \times 10^{16} m^{-3}$, $\omega_{rf}/2\pi = 13.56$ MHz.

sults more profound. Finally, when the electron temperature is used as a scaling parameter (see figure 3.7), although the PIC result and Lieberman's prediction scale similarly ($\bar{P} \propto T_e^{1/2}$), Lieberman's model overestimates the power deposition by a factor of two. Also, the importance of electron thermal loss to the electrode when that is included in the calculation (+ symbols in figure 3.7) has to be noted. The rf voltage amplitude is kept almost constant for these measurements ($\simeq 2000V_{p-p}$).

3.6 “Hard Wall” errors

Following the arguments presented in the previous sections, although the above scalings of power deposition show a fair agreement with the theoretical predictions, this can only hold if one of the two important assumptions of the underlying theory breaks down: that is, either the HWA or the Maxwellian nature of the incident electron fluxes to the sheath. It is therefore of interest to examine the error that the HWA would give when applied on the self-consistent field obtained by the PIC simulation. The procedure followed is to consider that the instantaneous sheath edge at time t is found where the displacement current has dropped to 10% of the value it had at the electrode. The sheath position is smoothed with a FFT filter to avoid anomalies caused by the small amplitude plasma oscillations (discussed in section 3.8) and by differentiating, the sheath velocity at time t is obtained. A typical case is shown in figure 3.8. Although this procedure seems arbitrary, it gives an accurate estimate of the sheath position and velocity. The results obtained hereafter are not prone to important changes when different criteria (drop percentage of the displacement current) for the sheath edge are used.

A good test for the validity of this criterion is to check whether the average electron velocity at the sheath edge matches the sheath speed, implying current continuity. This is shown in figure 3.9 where the two velocities are very close to each other except for the phases when the sheath is near the electrode. This emphasises the point that conservation of current implies that the electrons arrive at the sheath edge with an average velocity equal to that of the sheath and, therefore, there will be no net energy gain over a full rf period. The disagreement of the two velocities at phases when the sheath is nearly collapsed occurs because at those phases the magnitude of the electric field is small and therefore electron current in the sheath region,

3.6 "Hard Wall" errors

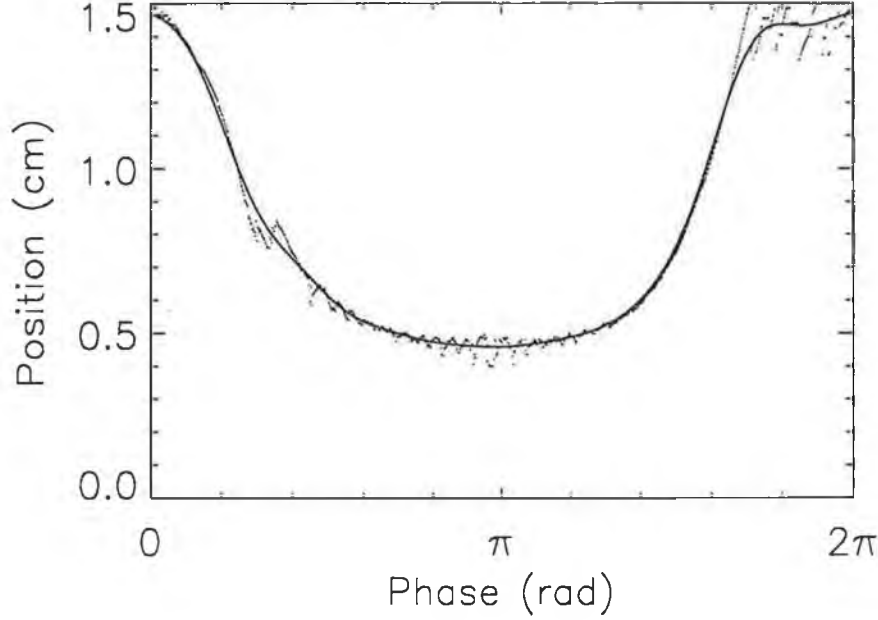


Figure 3.8: Dots indicate the sheath position obtained by the method described in the text. The solid line corresponds to the FFT fitting. Conditions: $I_{rf} = 60 \text{ Am}^{-2}$, $n_e = 5.0 \times 10^{15} \text{ m}^{-3}$, $\omega_{rf}/2\pi = 13.56 \text{ MHz}$, $T_e = 2.57 \text{ eV}$.

as well as electron loss, become significant.

Using the Monte-Carlo simulation described in section 3.4 with the self-consistent field as a model field, the relative error of the HWA

$$\sigma = \frac{u_r - 2u_s + u_i}{2u_s - u_i}, \quad (3.16)$$

can be calculated, where u_i is the incident velocity of the electron coming from the bulk and u_r is the velocity of the reflected electron. The velocity of the sheath edge at time $t = \frac{1}{2}(t_1 + t_2)$ is denoted by u_s , where t_1 is the time when the electron crossed the sheath edge coming from the bulk with $u > u_s$ and $t_2 > t_1$ the time when it crossed the sheath edge going towards the bulk with $u < u_s$. The result averaged over many electrons as a function of the

3.6 "Hard Wall" errors

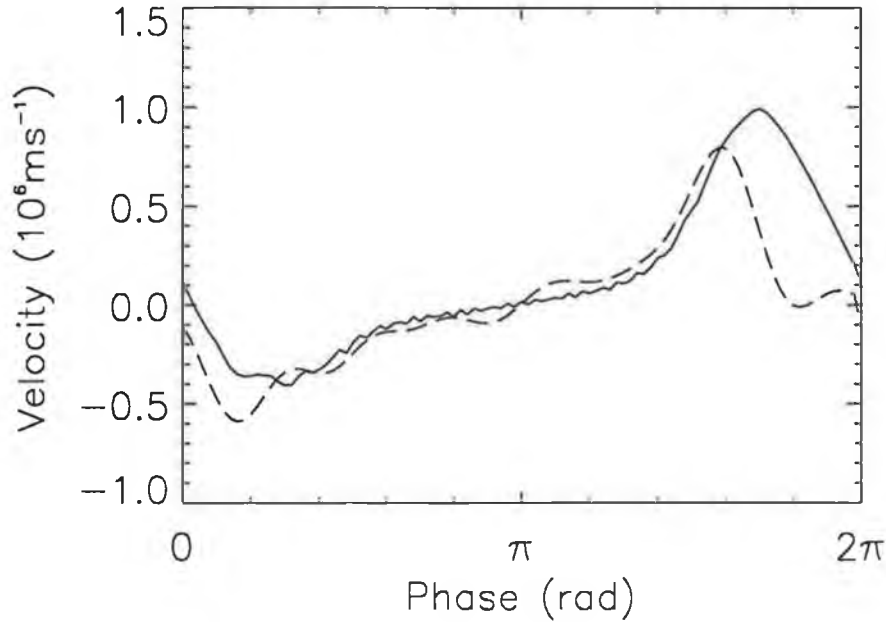


Figure 3.9: *The average electron velocity on the sheath edge (solid line) and the sheath velocity (dashed line). Conditions as in figure 3.8.*

rf phase is shown in figure 3.10. From the graph it is clear that the errors remain of the order of 10% for most of the rf period. They are the result of neglecting electron inertia and the time dependence of the quasi-neutrality field. Electrons lost to the electrode or reflected by the quasi-neutrality field are not included in the calculation, but should be considered in general. During the retraction phase of the sheath, the errors can grow large due to the rapid movement of the sheath and the presence of a field reversal which exists in order to accelerate the electrons towards the electrode and maintain a zero net current over the rf cycle (see Turner and Hopkins [68] who have attributed the field reversal to a collisional drag force, Vender and Boswell for PIC measurements [62] and Sato and Lieberman [69] for experimental measurements showing a field reversal).

3.7 Direct calculation of heating due to Fermi acceleration

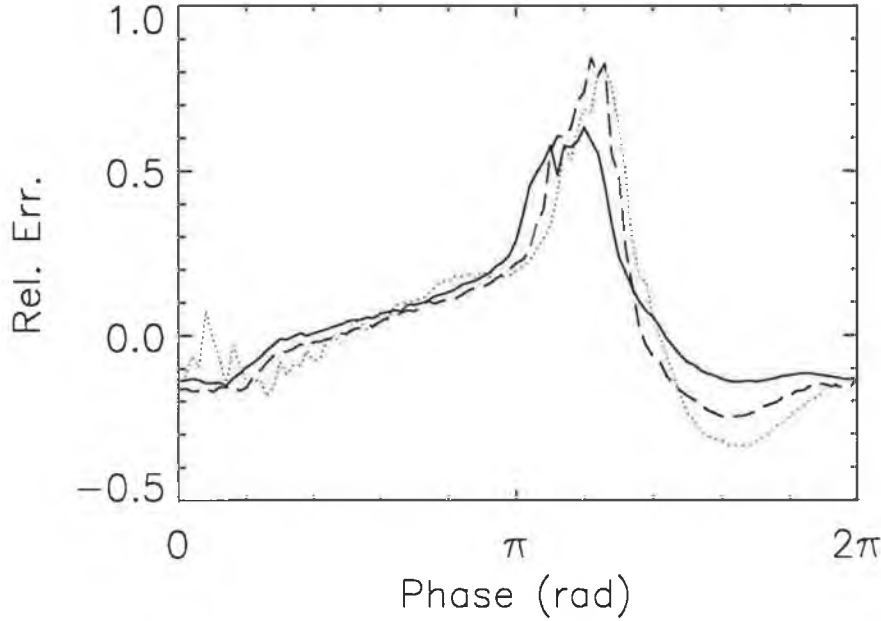


Figure 3.10: *The error given by the HWA. Solid line is for $I_{rf} = 130 \text{ Am}^{-2}$, dotted line for $I_{rf} = 140 \text{ Am}^{-2}$ and dashed line for $I_{rf} = 150 \text{ Am}^{-2}$. Conditions: $n_e = 1.5 \times 10^{16} \text{ m}^{-3}$, $\omega_{rf}/2\pi = 13.56 \text{ MHz}$, $T_e = 2.57 \text{ eV}$.*

3.7 Direct calculation of heating due to Fermi acceleration

It remains to investigate the nature of the incident and reflected distributions of the electrons interacting with the sheath edge. In figure 3.11 the electron distribution function sampled over many rf cycles ($\simeq 500$) near the instantaneous sheath edge at various phases is shown along with the drifting Maxwellian assumed by the theory. Notice that during the initial and final parts of the cycle the distribution departs from being Maxwellian. The gross distortion at the end of the collapse phase is due to the field reversal that develops in order to accelerate the electrons towards the electrode transform-

3.7 Direct calculation of heating due to Fermi acceleration

ing the distribution into a beam. It must be kept in mind however, that the electrons affected escape and do not otherwise contribute to heating.

From what has been demonstrated so far it is apparent that there exist deviations from both the HWA and the assumption that the electron distribution is a drifting Maxwellian at the sheath edge. These deviations leave the possibility open for heating to appear due to the Fermi acceleration mechanism. Therefore, an attempt to evaluate directly whether heating does occur through this mechanism or not is necessary. The approach chosen here is as follows: knowing the instantaneous sheath position from the method described in section 3.6, a set of electron distribution functions on the instantaneous sheath edge is collected at one hundred evenly distributed time intervals in the rf cycle. From these, equation (3.6) can be evaluated directly and hence a calculation of the heating which can be attributed to the mechanism proposed can be performed. A typical result is shown in figure 3.12 along with the actual power per unit area calculated from $\overline{P - P_{loss}}$ and Lieberman's theoretical prediction. Note that the three curves are not only quite different from each other, but also the one corresponding to the direct calculation of equation (3.6) integrates to almost zero. Observe also that the direct calculation agrees quite well with the dashed line which corresponds to the correct calculation of the power deposition due to Fermi acceleration (equation (3.9) in section 3.3). The above procedure has been repeated for a range of different parameters and the result was found to remain invariable: the average power per unit area dissipated is always much smaller than $\overline{P - P_{loss}}$ and averages to almost zero. These simulation results indicate, in accordance with the analytic calculation presented in section 3.3, that a hard-wall type of interaction with the sheaths cannot correctly interpret collisionless electron heating [70].

3.7 Direct calculation of heating due to Fermi acceleration

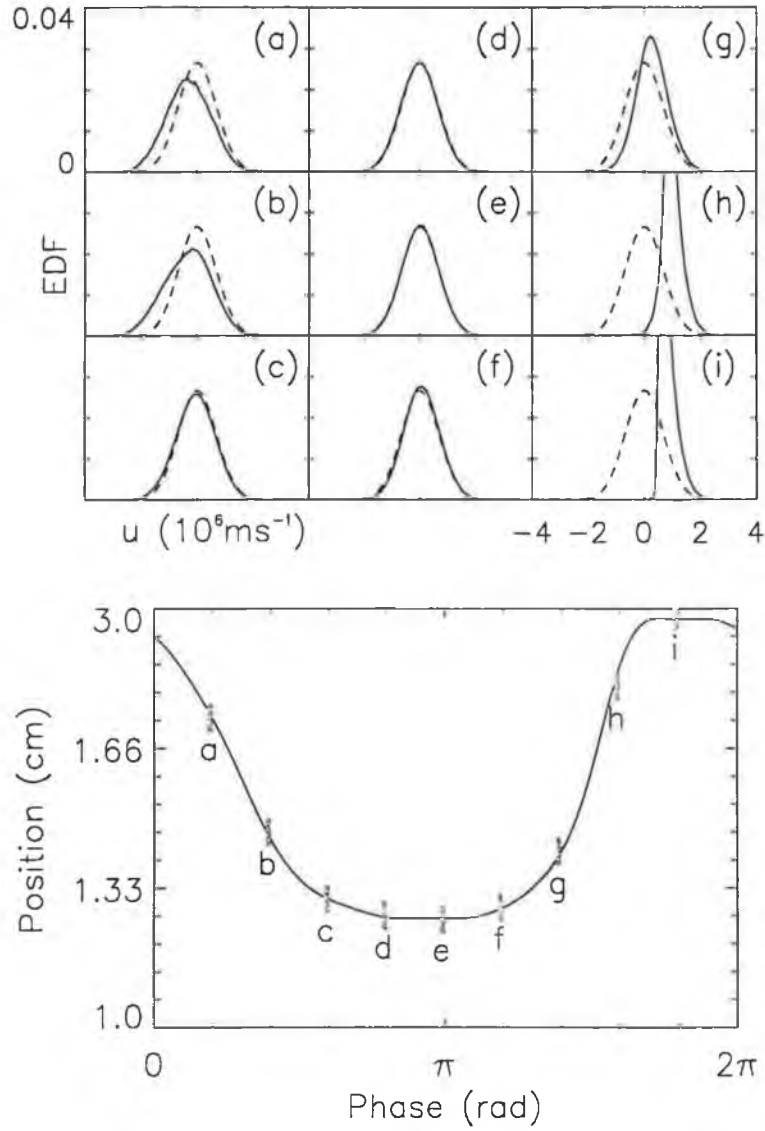


Figure 3.11: *Electron velocity distribution functions normalised to unity. Solid lines correspond to the distributions calculated from the simulation at phases and positions indicated in the bottom figure. Dashed lines correspond to the expected Maxwellian distributions. The average electron velocity ($\approx 5 \times 10^4 \text{ ms}^{-1}$) under these conditions is small compared to the thermal velocity ($\approx 7 \times 10^5 \text{ ms}^{-1}$). Conditions: $I_{rf} = 130 \text{ Am}^{-2}$, $n_e = 1.5 \times 10^{16} \text{ m}^{-3}$, $\omega_{rf}/2\pi = 13.56 \text{ MHz}$, $T_e = 2.57 \text{ eV}$.*

3.8 Plasma oscillations near the sheath edge

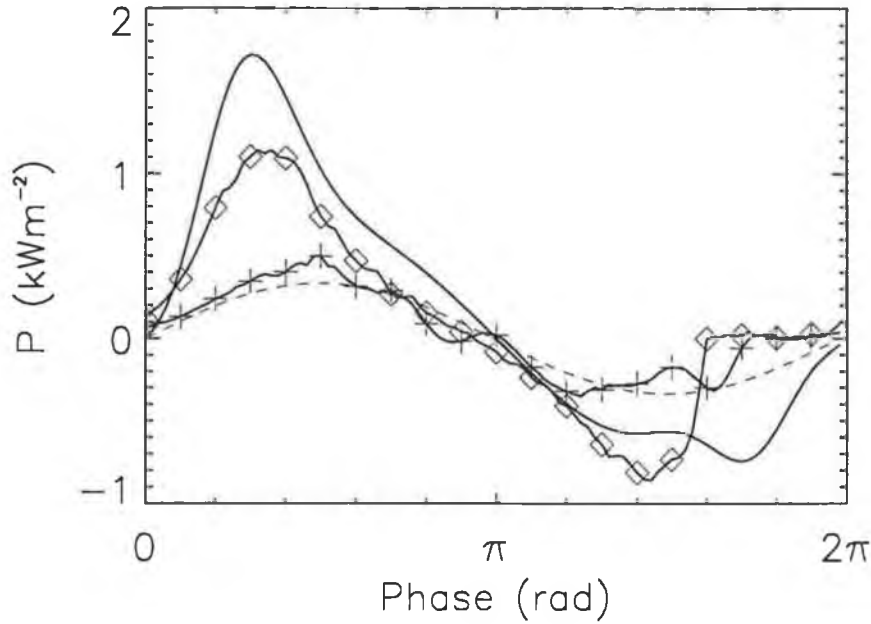


Figure 3.12: *The contribution of stochastic heating to the power per unit area as a function of phase. The bare solid line corresponds to Lieberman's prediction of \overline{P} , \diamond to $\overline{P} - \overline{P}_{loss}$, the dashed line to equation (3.9), and + is a direct evaluation of equation (3.6). Conditions: $I_{rf} = 130 \text{ Am}^{-2}$, $n_e = 1.5 \times 10^{16} \text{ m}^{-3}$, $\omega_{rf}/2\pi = 13.56 \text{ MHz}$, $T_e = 2.57 \text{ eV}$.*

3.8 Plasma oscillations near the sheath edge

The plasma oscillations that always occur near the instantaneous sheath edge are briefly discussed in this section. These oscillations have been reported before by Vender and Boswell [62] and in a similar context by Borovsky [71]. Experimental evidence of these oscillations was given by Wood *et al.* in [72]. They are the result of the progressive failure of quasi-neutrality at the electron sheath edge and are enhanced as the ratio of the drift velocity to the thermal velocity increases. They are more visible during the expansion

3.9 Summary

of the sheath towards the plasma: at the time when the sheath attains its maximum velocity, a plasma wave starts propagating towards the bulk of the plasma (see figure 3.13). The same happens while the sheath retreats, but the wave moves towards the electrode and the effect is smaller. At conditions where this ratio becomes sufficiently large, there seems to be significant particle-wave interaction, including particle-trapping effects, and this leads to instantaneous power deposition. However, this power transfer does not seem to contribute significantly to the total power deposition in an average sense. The electron distribution function though can be strongly affected.

3.9 Summary

The electron dynamics in the sheath region of a rf capacitive discharge have been investigated in connection with stochastic heating through Fermi acceleration using analytic and self-consistent models. The results obtained indicate that the presence of a small field in front of the sheath edge which preserves quasi-neutrality is important, and its exclusion from models which attempt to describe the sheath dynamics leads to a violation of current conservation. A time-independent approximation of this field has been provided but a more realistic solution requires a self-consistent treatment of the whole sheath.

In addition, it has been shown that the Hard Wall Approximation (although it can be used for the derivation of models that attempt to investigate analytically the global dynamics of the rf sheath), can be applied only when the sheath is moving slowly. In contrast, the applicability of the HWA turns out to be very limited when the sheath is moving fast due to the fact that electron inertia and transit time effects are neglected.

3.9 Summary

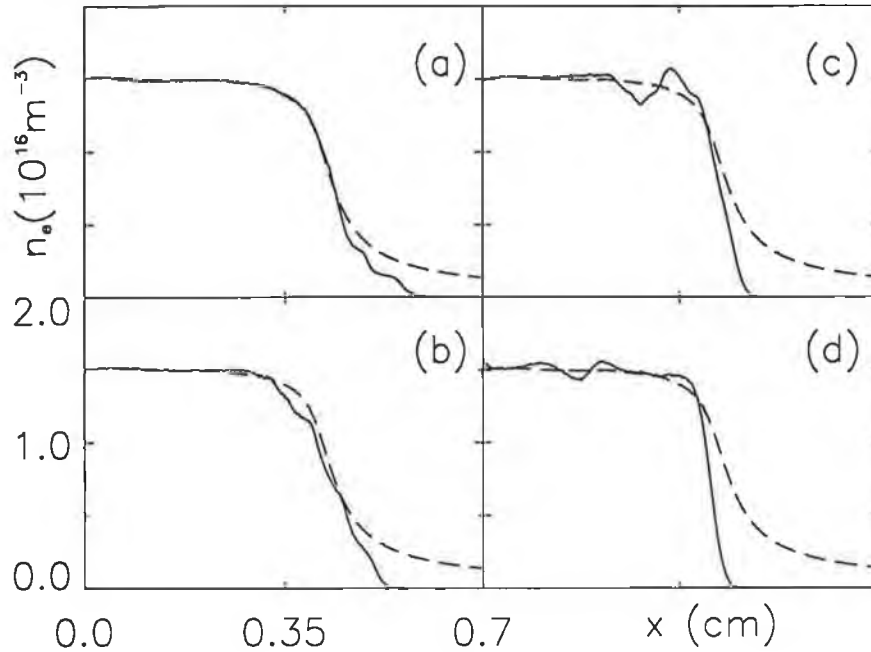


Figure 3.13: *The evolution of the failure of quasi-neutrality and the propagation of a plasma wave towards the bulk (left) is shown during the expansion phase of the sheath. During the contraction phase a similar wave moves to the opposite direction. (a) $t = 0.2 T_{rf}$, (b) $t = 0.25 T_{rf}$, (c) $t = 0.3 T_{rf}$, (d) $t = 0.4 T_{rf}$. Conditions: $\omega_{rf}/2\pi = 100.0$ MHz, $I_{rf} = 500$ Am⁻², $n_0 = 1.5 \times 10^{16}$ m⁻³, $T_e = 2.57$ eV.*

The scalings performed with a current drive and electron temperature as parameters showed fair qualitative agreement with Lieberman's theory, but not the scaling using the driving frequency as a parameter. This agreement seems to be fortuitous though, since the scaling laws with which the comparison was made have been obtained by using wrong assumptions and do not comply with current conservation. If instead the analytic calculation is performed correctly, it has been demonstrated that zero net power is to be expected.

3.9 Summary

To resolve this issue, the power deposition that can be attributed to the Fermi acceleration mechanism has been calculated self-consistently by the PIC simulation without any analytic approximations. The results obtained verified the analytic calculation, in that no net heating was found, despite the fact that some of the assumptions of the analytic calculation (namely the “Hard Wall” approximation and the Maxwellian nature of the electron distribution function in the sheath region) were only approximate. Therefore in conclusion, Fermi acceleration and the theories based upon it cannot provide the answer to the question of how and why electrons are heated in the absence of collisions.

Finally, the existence of plasma oscillations near the plasma-sheath interface has been noted. These oscillations originate from the gradual breaking of quasi-neutrality near the sheath edge, and can propagate from the plasma-sheath interface towards the bulk and vice-versa, following the motion of the sheath. The energy transfer through plasma-wave interactions due to these oscillations has been found negligible in a time average sense.

CHAPTER 4

Collisionless heating revisited

It has been shown in chapter 3 that the theory of stochastic heating based on Fermi acceleration is not relevant to capacitive rf discharges. However, the question of what *is* the actual mechanism through which energy transfer to the electrons is enabled has been left unanswered. In this chapter, an alternative route to a complete theory is discussed through an analytic model which accounts correctly for collisionless heating and is based on the theory of so-called *pressure heating*.

The idea of pressure heating had been initially suggested by Surendra and further explored by Turner. The general principle is that since the electron density drops from the bulk to the electrode, during the half-period when the electrons flow towards the electrode they get decompressed and cooled, whereas while they are pushed towards the bulk by the sheath in the other half-period they get compressed and heated.

Initially, Surendra and Graves [12] developed an analytic fluid model seeking to explain the electron cooling observed in the bulk plasma of a capacitive rf discharge. In that model, a sinusoidally driven collisional plasma is considered and the electron population is separated in two components, a “fast” and a “slow” one, with constant temperatures T_f and T_s respectively. The species, momentum balance and current conservation equations are linearised and solved with the assumptions that the density variation of the slow electrons is small compared to the fast ones and that all electron current in the ion-sheath region is due to the fast electrons [73]. The solutions obtained describe acoustic waves whose driving force is the pressure gradient and which are responsible for the negative heating observed.

However, the question whether sheath heating could be attributed to the same effect was not discussed, but in a later paper [60], Surendra and Dalvie showed by calculating separately the components of the momentum and energy balance equations from self-consistent PIC simulations that pressure terms can account for almost all of the power deposited.

Turner in [13] challenged the common idea that collisionless heating by the oscillating sheaths should be attributed to stochastic heating by presenting the following experiment: an ordinary PIC simulation is used to produce a discharge in the usual way. Then, using the ion density profile obtained from that simulation, another simulation is run where instead of having absorbing “electrodes” at the boundaries, periodic conditions are used. That is, an electron that would reach the left electrode now re-enters the simulation from the right electrode and vice-versa. At the same time, the simulation is started from a quasi-neutral state everywhere in the discharge, which is preserved at all times by suppressing ionisation. The result is a simulation where electrons move in the discharge following the fixed ion density profile

4.1 The pressure heating equation

but no sheath electric fields are present. Despite this, the heating observed is not much diminished compared to the original simulation where the sheath fields were present, and this supported the idea that the presence of the “oscillating walls” is not crucial to the heating mechanism.

Turner went on to propose that the rarefaction and compression of the electron population produces non-equilibrium thermal disturbances and that if there exist dissipative processes the net work done is not necessarily zero [13, 74]. An analytic fluid model was developed assuming that heat conduction in the energy balance equation can be written as

$$\frac{\partial q_e}{\partial x} = -n_e \bar{D}_e \frac{\partial^2}{\partial x^2} (kT_e) \quad (4.1)$$

where \bar{D}_e is the space-averaged electron diffusion coefficient. However, the model’s complexity makes it inappropriate for obtaining scaling laws and performing direct comparisons of its predictions with experiments and simulations.

No further attempt was made to clarify whether pressure heating is an additional mechanism to stochastic heating through Fermi acceleration (as is implied in [4]) or if it could account for collisionless heating as a whole. In this chapter a new analytic model is presented to describe pressure heating [75]. Scaling laws are obtained and the model predictions are compared directly to the simulation results.

4.1 The pressure heating equation

Let us start by describing the electrons by the one-dimensional collisionless Vlasov equation

$$\frac{\partial f}{\partial t} + v \frac{\partial f}{\partial x} - \frac{eE}{m} \frac{\partial f}{\partial v} = 0. \quad (4.2)$$

4.1 The pressure heating equation

A distribution f (not necessarily Maxwellian) is assumed for which an average velocity and thermal energy content can be defined such that

$$\int_{-\infty}^{\infty} f(v) dv = n, \quad (4.3)$$

$$\int_{-\infty}^{\infty} v f(v) dv = nu, \quad (4.4)$$

$$\int_{-\infty}^{\infty} mv^2 f(v-u) dv = nT, \quad (4.5)$$

where n is the electron particle density, u is the average velocity and the temperature T is measured in energy units for convenience. By multiplying by increasing powers of the velocity and integrating over velocity space, the first three velocity moments describing species, momentum and energy conservation are found to be

$$\frac{\partial n}{\partial t} + \frac{\partial nu}{\partial x} = 0, \quad (4.6)$$

$$m \frac{\partial nu}{\partial t} + \frac{\partial}{\partial x} (nT + mnu^2) + eEn = 0 \quad (4.7)$$

and

$$\frac{\partial}{\partial t} \left(\frac{1}{2} nT + \frac{1}{2} mnu^2 \right) + \frac{\partial}{\partial x} \left(\frac{3}{2} nuT + \frac{1}{2} mnu^3 + Q \right) + eEnu = 0, \quad (4.8)$$

where

$$Q = \frac{1}{2} m \int_{-\infty}^{\infty} v^3 f(v-u) dv \quad (4.9)$$

is the thermal flux. The drift energy terms and the electric field can be eliminated between equations (4.6), (4.7) and (4.8) to obtain

$$\frac{\partial}{\partial t} \left(\frac{1}{2} nT \right) + \frac{\partial (D + Q)}{\partial x} - u \frac{\partial (nT)}{\partial x} = 0, \quad (4.10)$$

where $D = (3/2)nuT$ is the convective flux.

Consider now a sinusoidally current-driven sheath, and assume that it consists of two distinct regions, one which is quasi-neutral and the other

4.1 The pressure heating equation

electron-free, separated by the electron sheath front. Provided that $\omega_{pe} \gg \omega \gg \omega_{pi}$, the displacement and ion currents in the quasi-neutral region can be ignored and therefore all current is carried by the electrons, such that

$$-enu = \tilde{J} \sin \omega t, \quad (4.11)$$

whereas in the space-charge region the current is purely displacement current. Integrating equation (4.10) in the quasi-neutral region between the Bohm point at $x = 0$ and the instantaneous sheath edge at $x = s(t)$, gives

$$\int_0^s \frac{\partial \frac{1}{2} n T}{\partial t} dx - \int_0^s u \frac{\partial n T}{\partial x} dx + Q \Big|_0^s + D \Big|_0^s = 0, \quad (4.12)$$

where the indices 0 and s indicate the Bohm point and the instantaneous sheath edge respectively.

Furthermore, it is assumed that the temperature is uniform across the sheath region. This remains to be justified, but it is a reasonable assumption considering the fact that if heating is *a priori* expected to be due to acoustic waves, only a small spatial variation of the temperature is anticipated inside the sheath since the acoustic wavelengths are usually large compared to the sheath length. Thus, equation (4.12) becomes

$$\frac{1}{2} \frac{dT}{dt} \int_0^s n dx - T \int_0^s u \frac{\partial n}{\partial x} dx + Q \Big|_0^s + D \Big|_0^s = 0. \quad (4.13)$$

The first integral can be evaluated by considering current conservation at the sheath edge

$$-enu = -en \frac{ds}{dt} = \tilde{J} \sin \omega t, \quad (4.14)$$

which by integration gives

$$\int_0^s n dx = \frac{\tilde{J}}{e\omega} (1 + \cos \omega t), \quad (4.15)$$

where the boundary conditions have been taken such that they agree with the definition of the current phase (that is at time $t = 0$, the sheath edge is

4.1 The pressure heating equation

found at the electrode, and the sheath starts expanding towards the plasma). Substituting u in the second integral from equation (4.11), equation (4.13) becomes

$$\frac{1}{2}(1 + \cos \omega t) \frac{\tilde{J}}{e\omega} \frac{dT}{dt} + \frac{\tilde{J}T}{e} \ln \left(\frac{n_s}{n_0} \right) \sin \omega t + Q \Big|_0^s + D \Big|_0^s = 0. \quad (4.16)$$

Notice now that there can be no thermal flux towards or from the electron-free region and therefore, $Q_s = 0$. There is however a convective flux at that point associated with the sheath motion, so that $D_s = 3/2 n_s u_s T$, but this term is cancelled by the convection term at the Bohm point $D_0 = 3/2 n_0 u_0 T$ because of flux conservation. In order to calculate the thermal flux at the Bohm point, it is further assumed that the electron distribution at the Bohm point is composed by two electron populations, one entering the sheath with a density n_{in} and a temperature T_{in} , and the other leaving the sheath with a density n_{out} and a temperature T_{out} . The thermal flux at the Bohm point is therefore

$$Q_0 = \frac{1}{2} (n_{in} \bar{v}_{in} T_{in} - n_{out} \bar{v}_{out} T_{out}), \quad (4.17)$$

where $\bar{v}_{in,out} = (8T_{in,out}/\pi m)^{1/2}$ are the respective average electron velocities. For consistency with the previous assumptions, the following conditions need to be imposed:

$$\begin{aligned} n_{in} + n_{out} &= n_0, \\ n_{in} T_{in} + n_{out} T_{out} &= n_0 T, \\ n_{in}^2 T_{in} - n_{out}^2 T_{out} &= 0, \end{aligned} \quad (4.18)$$

where the second condition in the system of equations (4.18) says that the temperature at the Bohm point is identically T as has been assumed and the third condition is such that there is no directed random particle flux at that point. By assuming that the electrons entering the sheath come

4.2 Approximate solution of the pressure heating equation

from the unperturbed bulk with temperature $T_{in} = T_b$, where T_b is the bulk temperature, T_{out} is found to be

$$T_{out} = \frac{T^2}{T_b}. \quad (4.19)$$

Note that by taking T_b to be constant, in common with previous models [7, 76], assumptions about thermalisation of electrons in the plasma bulk are implied (on this point see [48]).

After some algebraic manipulation the thermal flux at the Bohm point turns out to be

$$Q_0 = \frac{1}{2} n_0 \bar{v}_b T \left(1 - \frac{T}{T_b} \right) = Q_b \frac{T}{T_b} \left(1 - \frac{T}{T_b} \right), \quad (4.20)$$

where $Q_b = 1/2 n_0 \bar{v}_b T_b$ is the thermal electron flux arriving at the sheath edge from the bulk plasma. Thus, the pressure heating equation finally becomes

$$(1 + \cos \omega t) \frac{dT}{dt} + 2\omega T \ln \left(\frac{n_s}{n_0} \right) \sin \omega t - \frac{2e\omega}{\tilde{J}} Q_0 = 0, \quad (4.21)$$

or, replacing $\omega t = \theta$ and setting $u_0 = \tilde{J}/en_0$, $\tau = T/T_b$,

$$(1 + \cos \theta) \frac{d\tau}{d\theta} + 2\tau \ln \left(\frac{n_s}{n_0} \right) \sin \theta + \frac{\bar{v}_b}{u_0} \tau (\tau - 1) = 0. \quad (4.22)$$

4.2 Approximate solution of the pressure heating equation

Although it is difficult to solve equation (4.22) for the quantity τ , an approximate solution can be found if it is expressed as a power series in a small parameter $\delta \ll 1$. A convenient choice for δ is the ratio of the amplitude of the drift velocity at the Bohm point to the average velocity in the bulk, i.e. $\delta = u_0/\bar{v}_b$. Taking

$$\tau = \tau^{(0)} + \delta \tau^{(1)} + \delta^2 \tau^{(2)} + O(\delta^3), \quad (4.23)$$

4.2 Approximate solution of the pressure heating equation

inserting this expressions into the differential equation and retaining terms up to $O(\delta^2)$ produces

$$\begin{aligned} (1 + \cos \theta) \left(\delta \frac{d\tau^{(0)}}{d\theta} + \delta^2 \frac{d\tau^{(1)}}{d\theta} \right) \\ + 2 (\delta \tau^{(0)} + \delta^2 \tau^{(1)}) \ln \left(\frac{n_s}{n_0} \right) \sin \theta \\ + \delta \tau^{(1)} + \delta^2 \tau^{(2)} + \delta^2 \tau^{(1)2} = 0. \end{aligned} \quad (4.24)$$

Coefficients of each power of δ must vanish separately, so that

$$\tau^{(0)} - 1 = 0, \quad (4.25)$$

$$2 \ln \left(\frac{n_s}{n_0} \right) \sin \theta + \tau^{(1)} = 0, \quad (4.26)$$

$$(1 + \cos \theta) \frac{d\tau^{(1)}}{d\theta} + 2\tau^{(1)} \ln \left(\frac{n_s}{n_0} \right) \sin \theta + \tau^{(2)} + \tau^{(1)2} = 0, \quad (4.27)$$

and

$$\tau^{(0)} = 1, \quad (4.28)$$

$$\tau^{(1)} = -2 \ln \left(\frac{n_s}{n_0} \right) \sin \theta, \quad (4.29)$$

$$\begin{aligned} \tau^{(2)} &= - \left\{ 2\tau^{(1)} \ln \left(\frac{n_s}{n_0} \right) \sin \theta + (1 + \cos \theta) \frac{d\tau^{(1)}}{d\theta} + \tau^{(1)2} \right\} \\ &= -(1 + \cos \theta) \frac{d\tau^{(1)}}{d\theta}. \end{aligned} \quad (4.30)$$

Also

$$\frac{d\tau^{(1)}}{d\theta} = -2 \left\{ \cos \theta \ln \left(\frac{n_s}{n_0} \right) + \sin \theta \frac{1}{n_s} \frac{dn_s}{d\theta} \right\}, \quad (4.31)$$

so

$$\tau^{(2)} = 2(1 + \cos \theta) \left\{ \cos \theta \ln \left(\frac{n_s}{n_0} \right) + \sin \theta \frac{1}{n_s} \frac{dn_s}{d\theta} \right\}. \quad (4.32)$$

The average power deposition can now be calculated by noting that it is

4.2 Approximate solution of the pressure heating equation

essentially the average of the thermal flux at the Bohm point

$$\begin{aligned}
 \langle P \rangle &= -\langle Q_0 \rangle \\
 &= \frac{1}{2} n_0 \bar{v}_b T_b \left\langle \delta \tau^{(1)} + \delta^2 \left(\tau^{(2)} + \tau^{(1)2} \right) \right\rangle + O(\delta^3) \\
 &= Q_b \left\langle \delta \tau^{(1)} + \delta^2 \left(\tau^{(2)} + \tau^{(1)2} \right) \right\rangle + O(\delta^3). \tag{4.33}
 \end{aligned}$$

From equation (4.33) the power deposition can be calculated for any given density profile in the sheath region. Note also that equation (4.33) vanishes for $\delta \rightarrow 0$, which corresponds to electrons in Boltzmann equilibrium, as expected.

4.2.1 Power deposition for the symmetric sheath case

The best available analytic model providing a solution for the density profile in the sheath, is Lieberman's model (see appendix A). In that model, the density at the sheath edge is given by

$$\frac{n_s}{n_0} = \left[1 - H \left(\frac{3}{8} \sin 2\phi - \frac{1}{4} \phi \cos 2\phi - \frac{1}{2} \phi \right) \right]^{-1}, \tag{4.34}$$

where $H = \tilde{s}_0^2 / (\pi \lambda_D^2)$, $\tilde{s}_0 = \tilde{J} / (e \omega n_0)$ is an effective amplitude of the sheath oscillation, and λ_D is the electron Debye length. The phase ϕ is related to θ by $\phi = \theta + \pi$.

Lieberman's model describes a symmetric sheath (meaning that $n_s(-\phi) = n_s(\phi)$) with no electron loss. Under these conditions, the first order term in equation (4.33) vanishes to give

$$\langle P \rangle = Q_b \delta^2 \left\langle \tau^{(2)} + \tau^{(1)2} \right\rangle + O(\delta^3). \tag{4.35}$$

The bracketed quantities in equation (4.35) averaged over an rf cycle are functions solely of the dimensionless parameter H , and it has been found

4.3 Comparison with the PIC simulation

that a good fit for $1 < H < 50$ (which covers essentially the range of all values that H can take for any reasonable parameter set) is

$$\langle P \rangle \approx Q_b \delta^2 \frac{35H}{60 + H}. \quad (4.36)$$

4.3 Comparison with the PIC simulation

In order to get the closest possible comparison with theory, the PIC simulation has to be adapted so as to model a time symmetric sheath. This can be achieved by running a simulation to steady state and then stopping the movement of the ion super-particles. Since this eliminates ion loss, electron loss also stops and the sheath becomes symmetric in the sense discussed above. An example can be seen in figure 4.1 where the electron density is shown as a function of phase and position in the sheath for the “normal” and symmetric cases.

The power deposition as a function of phase from the symmetric PIC simulation is compared to the analytic model in figure 4.2 and very good agreement is obtained. This agreement persists over a large range of parameters as shown in figure 4.3 where the average power deposition normalised to $Q_b \delta^2$ is shown as a function of the parameter H . The symbols correspond to the power deposition calculated by the simulation for a current range between $\tilde{J} = 110 \text{ Am}^{-2}$ and $\tilde{J} = 180 \text{ Am}^{-2}$ at a fixed frequency equal to $f_{rf} = 13.56 \text{ MHz}$ (+ symbols), and a frequency range from $f_{rf} = 10 \text{ MHz}$ to $f_{rf} = 80 \text{ MHz}$ at a fixed maximum rf voltage at the electrode equal to 400 Volts (\diamond symbols). In the same figure, Lieberman’s result (equation (3.10) in section 3.3 based on stochastic heating is plotted and is shown to clearly overestimate the power deposition. Note that this does not invalidate the results shown in chapter 3 where better agreement between Lieberman’s result

4.3 Comparison with the PIC simulation

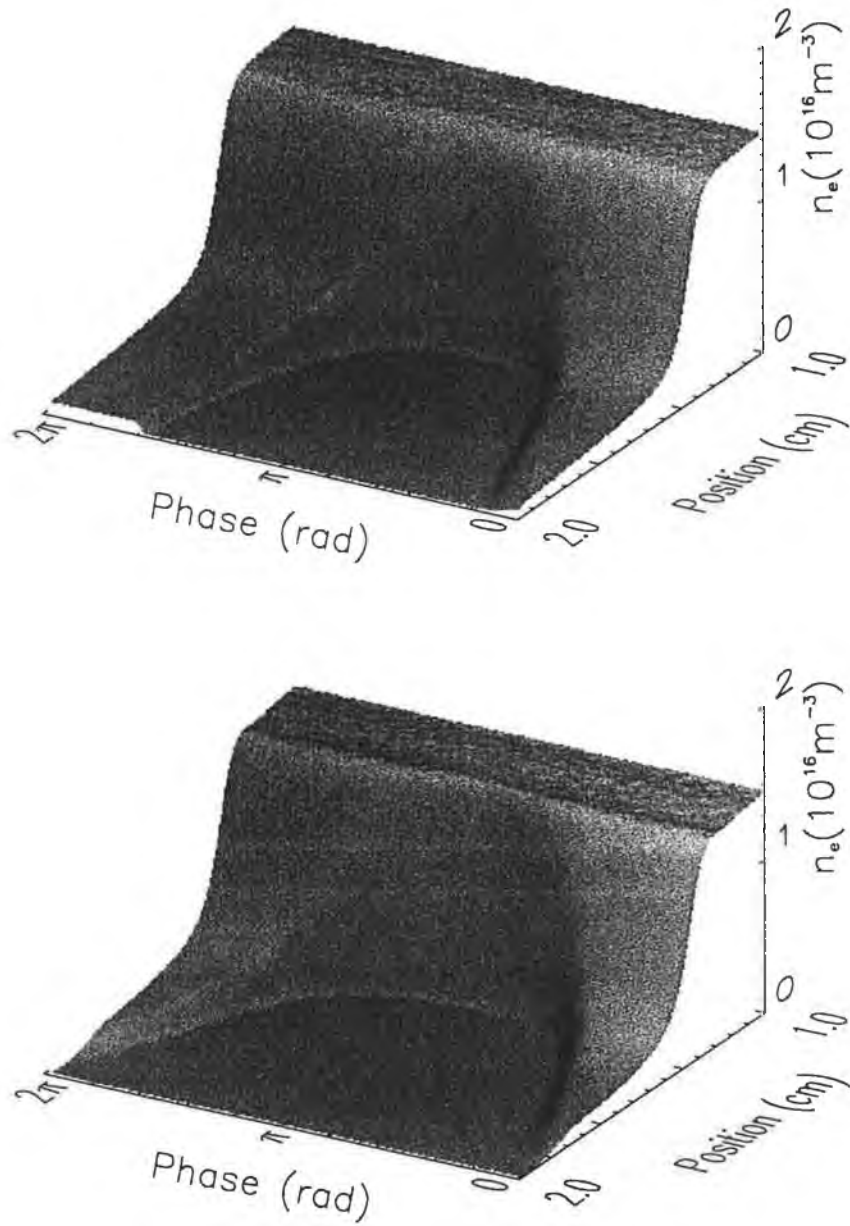


Figure 4.1: The electron density profile from the normal PIC (top) and the PIC where symmetry was imposed (bottom). Conditions: $\tilde{J} = 130 \text{ Am}^{-2}$, $\omega_{rf}/2\pi = 13.56 \text{ MHz}$, $n_0 = 1.5 \times 10^{16} \text{ m}^{-3}$, $T_b = 2.57 \text{ eV}$.

4.3 Comparison with the PIC simulation

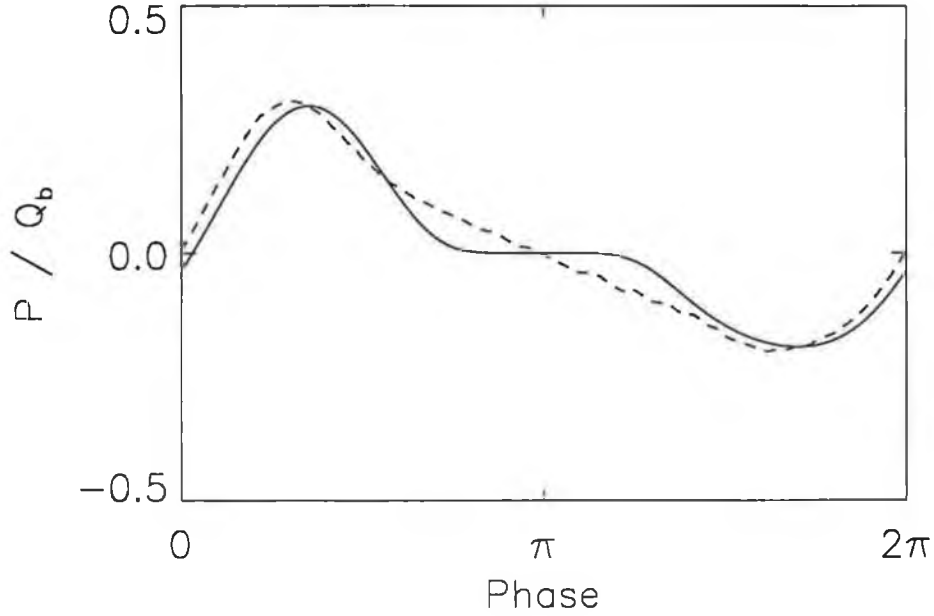


Figure 4.2: A comparison of the power deposition normalised to the heat flux from the bulk Q_b from the model and the symmetric PIC simulation. The solid line is the model prediction and the dashed line is the PIC result. Conditions as in figure 4.1

and the PIC simulation was obtained, as here the symmetric PIC is used for the comparison. In fact, it is the symmetric PIC simulation that provides a better basis of comparison since Lieberman's model treats the symmetric sheath case.

On the other hand, the temperature variation obtained by the model and shown in figure 4.4 does not agree as well with the space-averaged temperature

$$\bar{T} = \frac{\int_0^{s(t)} \int_{-\infty}^{\infty} m(v-u)^2 f(v) \, dv \, dx}{\int_0^{s(t)} \int_{-\infty}^{\infty} f(v) \, dv \, dx}, \quad (4.37)$$

4.3 Comparison with the PIC simulation

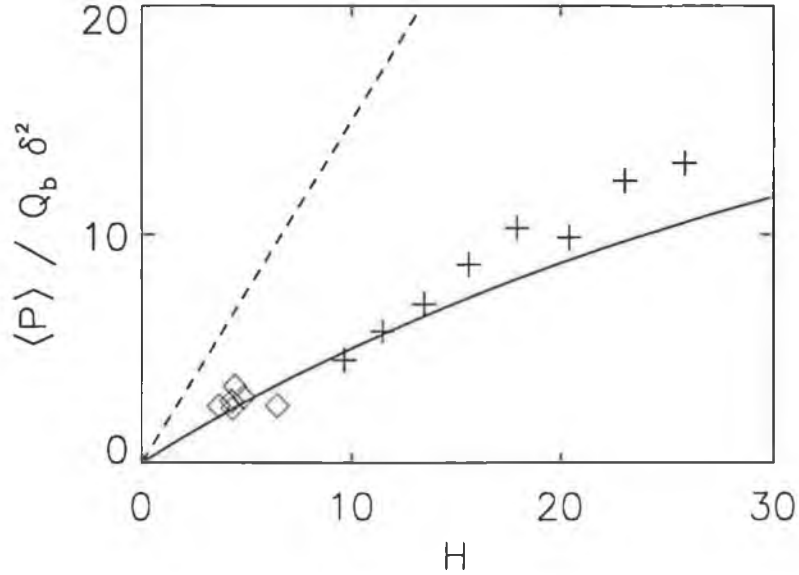


Figure 4.3: The average normalised power deposition as a function of the parameter H . The solid line is the model prediction calculated from equation (4.36), the dashed line is Lieberman's result [7], and the symbols correspond to the parameter range indicated in the text.

calculated from the symmetric PIC. This is mainly due to the simplifying assumption that the temperature remains constant in the sheath region. While this is not true, a fully self-consistent approach that would account for the spatial variation of the temperature in the sheath region appears not to be feasible, especially given the fact it would require modelling the sheath dynamics simultaneously. In any case, it is a secondary effect and has little importance as far as the calculation of power deposition goes, as has been shown already. For completeness, a contour of the variation of the temperature in time and space appears in figure 4.5. The underlying assumption corresponds to parallel horizontal isosurfaces in this graph. This is not grossly

4.4 The asymmetric sheath

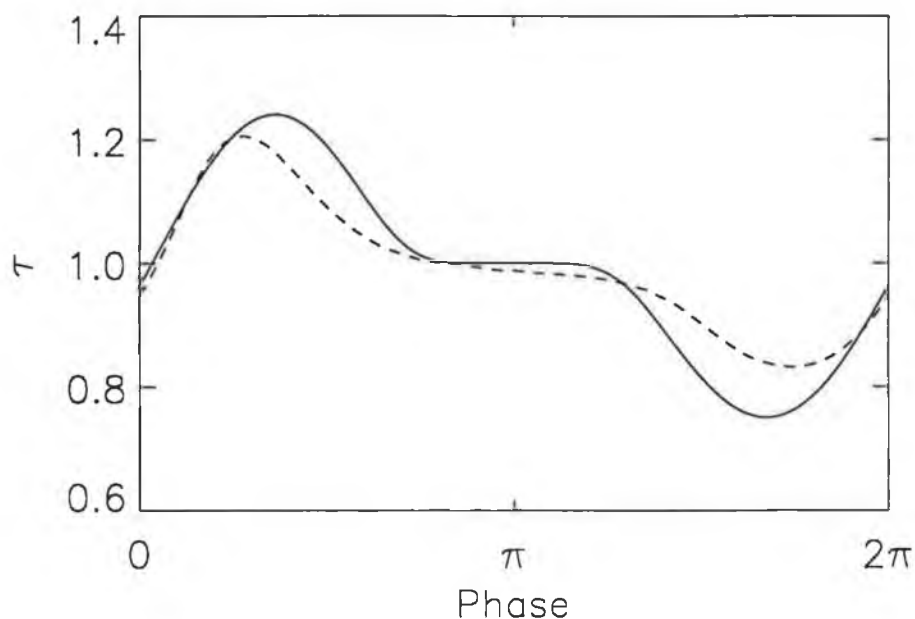


Figure 4.4: *A comparison of the variation of the normalised temperature τ from the model and the symmetric PIC simulation. The solid line is the model prediction and the dashed line is the PIC result. Conditions as in figure 4.2.*

violated.

4.4 The asymmetric sheath

So far, the case of the symmetric sheath has been considered, and it has been possible to obtain analytic scalings and a compact formula providing the contribution of pressure heating in terms of the discharge parameters. In the asymmetric case there are two major differences: on the one hand, there is a finite contribution of the first-order term in the averaging of equation (4.33), on the other hand, electron loss has to be considered.

However, the pressure heating mechanism remains the same. This can

4.4 The asymmetric sheath

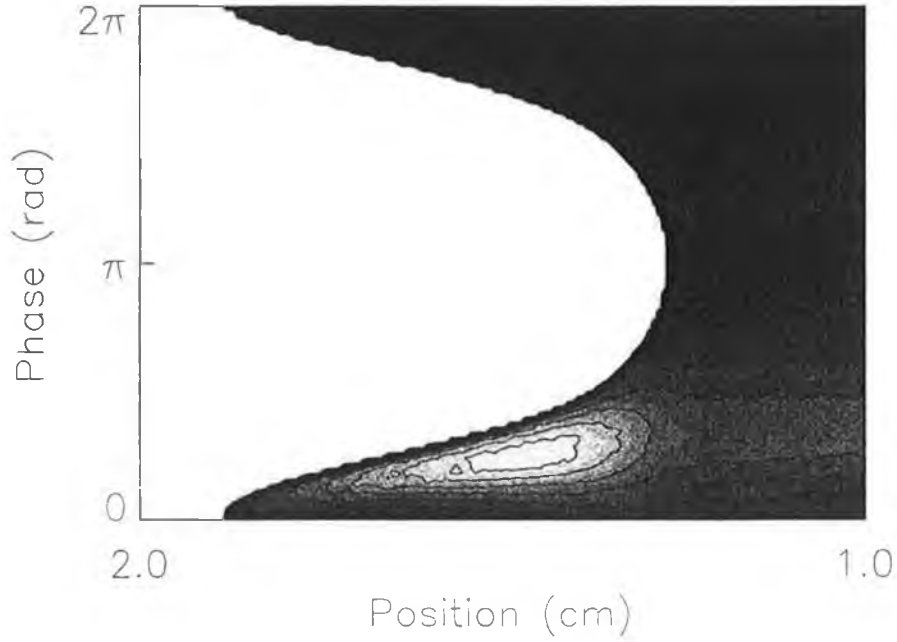


Figure 4.5: The variation of the normalised temperature in time and space as obtained by the symmetric PIC. White corresponds to $\tau = 1.5$ while black to $\tau = 0.5$. Conditions as in figure 4.2.

be demonstrated by noticing that if the second order terms are ignored, the instantaneous power deposition becomes

$$\begin{aligned}
 P &= \frac{1}{2} n_0 \bar{v}_b T_b \delta \tau^{(1)} \\
 &= -n_0 \bar{v}_b T_b \delta \ln \frac{n_s}{n_0} \sin \theta \\
 &= -n_0 \bar{v}_b T_b \delta \sin \theta \int_0^s \frac{1}{n} \frac{dn}{dx} dx.
 \end{aligned} \tag{4.38}$$

In figure 4.6 the result of equation (4.38) when the integration is performed over the density profile from the (asymmetric) simulation is compared with the power calculated from the simulation. There is perfect agreement everywhere except at the end of the rf cycle where electron loss becomes important, illustrating the correctness of the model.

4.5 Discussion

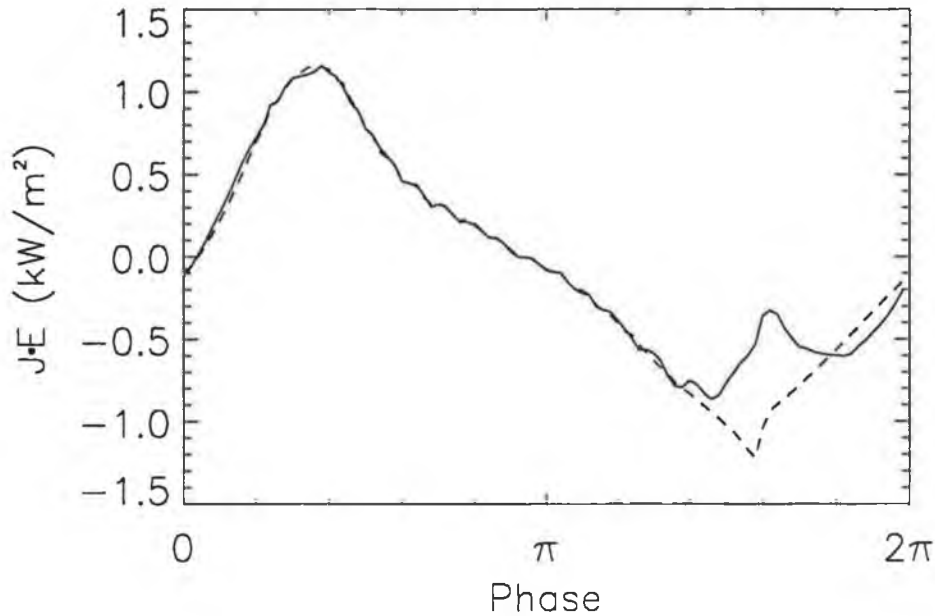


Figure 4.6: *A comparison of the power per unit area and P_{pr} (dashed line) variation from the PIC (asymmetric) simulation. Conditions as in figure 4.2.*

4.5 Discussion

It is interesting to compare at this point the two theories that have been discussed so far, that of stochastic heating through Fermi acceleration and that of pressure heating. According to the stochastic heating arguments, heating is the result of the instantaneous energy exchange of electrons with the sheath edge. In other words, heating is considered as a localised effect and what happens in between these interactions is somehow irrelevant, save for current conservation issues and the randomisation processes involved to permit heating. In addition, the electrons interact individually with the sheath edge and their collective behaviour has no crucial role. Pressure heating presents us with a completely different idea. It is not the sheath edge on

4.5 Discussion

which the emphasis is focused, but rather the dynamical interaction of the electrons with the fields that lie in the entire sheath region (essentially the field described as the “quasi-neutrality” field in section 3.4). Heating does not appear as a localised effect, and no importance is attached to the existence of a point separating the quasi-neutral plasma from the space-charge region of the sheath. In addition, the fluid interpretation of pressure heating emphasises the collective action of electrons.

Whether the two theories are complimentary or represent a different interpretation of the same idea is an interesting question. Pressure heating, was indeed viewed as an “additional mechanism” [4], but, from the arguments developed in this chapter, pressure heating accounts for the *whole* of the heating observed. Although one can think of the possibility of formulating a model based on Fermi acceleration, with a “wall” velocity conveniently chosen to provide net heating with the correct scalings, it is not easy to see on what physical basis that model would stand.

Summarising, it has been shown in this chapter that pressure heating is consistent with the calculated power deposition in the PIC simulation. An analytic model has been developed which illustrates the mechanism, and given a density profile in the sheath, can provide quantitative information about the heating rates. Solved for the case of a symmetric sheath using Lieberman’s model for the density profile, the model exhibits very good agreement with a PIC simulation modelling a symmetric sheath as far as the prediction of power deposition is concerned. The prediction of the temperature variation with time was not as good but this is not critical for the model. Finally, for the asymmetric sheath case, due to the absence of a convenient analytic model of the sheath including electron loss (the Godyak-Sternberg model [77] would be appropriate, but due to its complexity the density profile

4.5 Discussion

cannot be derived from it), no analytic scalings were obtained. However, the correctness of the pressure heating model has been demonstrated by using the density profile from the PIC simulation. If in the future a model which accurately describes the asymmetric sheath is derived, it will be possible for the present model to be generalised.

CHAPTER 5

Investigation of the plasma-sheath transition

5.1 Introduction

5.1.1 The Bohm criterion

As has been mentioned in chapter 1, when the plasma comes in contact with a wall, the electrons, being more mobile than the ions, are absorbed initially at a faster rate by the wall. This results in the formation of a positive space-charge region called the sheath, which shields the plasma and extends to several electron Debye lengths λ_D . So far, this research has been concerned with the electron dynamics in the sheath region. In this chapter, the focus will shift to the ion behaviour and particularly to the ion dynamics outside the sheath connected with the sheath formation.

In order for the sheath to reach steady-state the ions have to fulfil the Bohm criterion which, in a simplified form for one ion species, states that

5.1 Introduction

the average ion velocity has to be greater or equal to the Bohm speed (or ion acoustic speed) i.e.¹

$$\langle u \rangle \geq \sqrt{\frac{kT_e}{m_i}} = c_s. \quad (5.1)$$

For such a high velocity to be generated, an additional layer called the *presheath* has to exist in front of the sheath in order to accelerate the ions. The characteristic length of this layer is of the order of the smallest of the characteristic lengths L of the plasma region associated with the ions (mean free path, ionisation length or lengths associated with the discharge geometry). The transition from the plasma to the sheath and the corresponding Bohm condition at the boundary will be the subject of this chapter. Despite the fact that this is a fundamental problem since it concerns practically any confined plasma, and although it dates from the first examinations of plasmas by Langmuir and Tonks [80, 81], it is still a point of much confusion.

The first explicit formulation of the Bohm criterion is due to Bohm [9] in 1949. In that original work, Boltzmann electrons and cold ions were assumed in an essentially hydrodynamic approach. To elucidate the problem and illustrate its physical meaning, the Bohm criterion will be demonstrated using the original approach (see [8]).

Let us consider a plasma with cold mono-energetic ions and hot Maxwellian electrons and assume that a sheath exists at $x \geq 0$. The ion distribution function $f(x, v)$ at the sheath edge is

$$f_i(0, v) = n_0 \delta(v - v_0), \quad (5.2)$$

¹Although strictly speaking the Bohm criterion gives a minimum for the average ion velocity, with some rare exceptions [78, 79] which correspond to non-neutral plasmas or plasmas with very high collisionality where the Debye length is of the same order or larger than the ion mean free path, it is found that the Bohm criterion is satisfied marginally, that is with the equality sign. From this point on, although the inequality sign will be retained, it is implied that the Bohm criterion is marginally satisfied.

5.1 Introduction

where n_0 is the density at the sheath edge (found at $x = 0$), $v_0 > 0$ is the ion velocity at the sheath edge and δ is the Dirac delta function. The ion distribution function can be obtained at any point in the sheath region from energy conservation i.e.,

$$f_i(x, v) = n_0 \delta \left(\sqrt{v^2 - \frac{2q_i V}{m_i}} - v_0 \right), \quad (5.3)$$

where V is the sheath potential. The electron distribution function is

$$f_e(x, v) = n_0 \sqrt{\frac{m_e}{2\pi k T_e}} \exp \left[-\frac{m_e}{2k T_e} \left(v^2 + \frac{q_e V}{m_e} \right) \right]. \quad (5.4)$$

Introducing the dimensionless variables

$$\eta = -\frac{q_i V}{k T_e}, \quad u = \frac{v}{v_s}, \quad \xi = x \sqrt{\frac{4\pi n_0 q_i^2}{k T_e}} \quad (5.5)$$

where $v_s = (m_i/2kT_e)^{1/2}$, gives

$$f_i(\eta, u) = n_0 \frac{\delta(\sqrt{u^2 - \eta} - u_0)}{u_s} \quad (5.6)$$

and

$$f_e(\eta, u) = n_0 \sqrt{\frac{m_e}{\pi m_i}} \frac{1}{v_s} \exp \left(-\frac{m_e}{m_i} u^2 - \eta \right). \quad (5.7)$$

To obtain the densities equations (5.6) and (5.7) have to be integrated with respect to velocity yielding

$$n_i = n_0 \int \delta(y - u_0) \frac{y dy}{\sqrt{y^2 + \eta}} = n_0 \left(1 + \frac{\eta}{u_0^2} \right)^{-\frac{1}{2}} \quad \text{and} \quad (5.8)$$

$$n_e = n_0 \exp(-\eta). \quad (5.9)$$

Finally, Poisson's equation becomes

$$\frac{d^2 \eta}{d\xi^2} = \frac{n_i - n_e}{n_0}. \quad (5.10)$$

Multiplying equation (5.10) by $\eta' = d\eta/d\xi$ and integrating, yields

$$\frac{1}{2} \eta'^2 = n_0 \{ 2u_0^2 [(1 + \eta u_0^{-2})^{\frac{1}{2}} - 1] + e^{-\eta} - 1 \} + \frac{1}{2} \eta_0'^2, \quad (5.11)$$

5.1 Introduction

where η_0 is the normalised potential at the sheath edge. Assuming that η'_0 is zero, and since the left-hand side of equation (5.11) is always positive, the following relation has to be satisfied

$$2u_0^2[(1 + \eta u_0^{-2})^{\frac{1}{2}} - 1] \geq 1 - e^{-\eta}, \quad (5.12)$$

which by Taylor-expanding near $\eta = 0$ gives

$$2u_0^2\left(\frac{1}{2}\eta u_0^{-2} - \frac{1}{8}\eta^2 u_0^{-4}\right) \geq \eta - \frac{1}{2}\eta^2, \quad (5.13)$$

or

$$u_0^2 \geq \frac{1}{2}, \quad (5.14)$$

which is the Bohm criterion written in the new variables.

An equivalent way to obtain the same result illustrating its physical meaning was pointed out by Allen and Thonemann [82]. It is easy to see from equation (5.10) that in order for a monotonic solution for $\eta(\xi)$ to exist, η'' must be positive in the vicinity of $\eta = 0$. In figure 5.1 the normalised electron density along with the normalised ion density are shown for various values of the incident ion velocity u_0 on a logarithmic scale. Observe that unless $u_0^2 \geq 1/2$, the ion density drops faster than the electron density, which would give oscillatory solutions for $\eta(\xi)$. Therefore, the conclusion is again that the Bohm condition has to be satisfied.

The demonstration presented above is subject to some criticism due to the fact that if η , η' and η'' were to vanish simultaneously at the origin, the potential would remain zero everywhere. However, as long as the electron Debye length is small compared to the other characteristic lengths of the system, the effect of finite but small η' and η'' is negligible.

The problem of accounting for a full ionic distribution function instead of cold mono-energetic ions was first treated by Harrison and Thompson [83],

5.1 Introduction

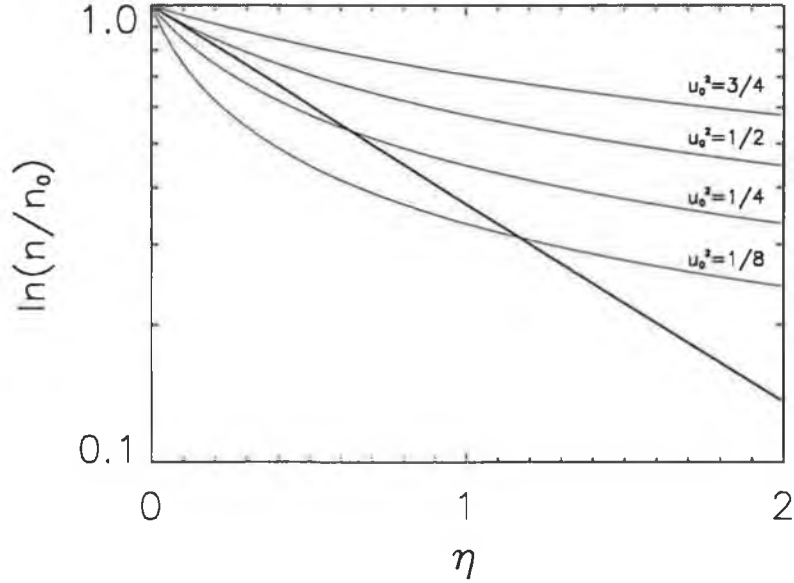


Figure 5.1: The electron density profile (straight line) and the ion density profile in the sheath as a function of potential η for various values of the incident ion velocity u_0 .

who considered that the ion distribution function is constituted by groups of ions k with velocities u_k and a density contribution c_k which yielded

$$\sum_k \frac{c_k}{m_k u_k^2} \leq \frac{1}{kT_e}, \quad (5.15)$$

or, for a continuous distribution function,

$$\left\langle \frac{1}{u^2} \right\rangle \leq \frac{m_i}{kT_e}. \quad (5.16)$$

However, objections regarding their derivation were made, concerning in particular whether the transition from equation (5.15) to equation (5.16) is valid [84]. A self-consistent kinetic calculation was carried out by Riemann [85] who found the same expression² as in equation (5.16).

²Note however that in Riemann's calculation the averaging takes place over the particles

5.1 Introduction

5.1.2 The Bohm criterion for multiple ion species

The case of multiple ion species has been treated by Riemann [27]. The result is a generalised Bohm criterion which in an hydrodynamic context yields

$$\sum_k \frac{q_k^2 n_{k0}}{m_k \langle u_{k0} \rangle^2} \leq \frac{e^2 n_{e0}}{kT_e}, \quad (5.17)$$

and in its kinetic form gives

$$\sum_k \frac{q_k^2 n_{k0}}{m_k} \left\langle \frac{1}{u_{k0}^2} \right\rangle \leq \frac{e^2 n_{e0}}{kT_e}, \quad (5.18)$$

where the summation index k runs over the ion species. An important point to note is that in contrast with the single ion case, the Bohm criterion does not provide enough information to obtain both the ion densities and average velocities at the sheath edge. That is, equation (5.17) in combination with a quasi-neutrality condition at the sheath edge

$$\sum_k q_k n_{k0} = e n_{e0}, \quad (5.19)$$

provides only 2 equations for $2k$ unknowns and, generally speaking, there is no reason for the trivial solution (each ion arriving at the sheath edge with an average velocity equal to its own Bohm velocity) or any other restrictive solution to be assumed. A particular solution could only be obtained, if at all, by using global equations that describe generation and loss mechanisms, and taking into account plasma/presheath dynamics. This point has recently attracted a lot of attention and contradictory statements have been made: Franklin, for example [86], assuming constant ionisation rates and that the density ratio between the two ion species is constant over the discharge, showed that in the collisionless limit the ions will arrive at the sheath boundary, each with its own Bohm speed. In contrast, Hershkowitz incident on the sheath edge (that is particles with $u > 0$) only.

5.1 Introduction

et al. [87] have presented measurements from experiments performed on a multi-dipole low-pressure plasma indicating that the two ion species present (argon and helium) both arrived at the sheath edge with a velocity equal to the sound speed of the plasma. In brief, no final conclusion has been reached yet as far as this point is concerned. This is further discussed in section 5.3.

5.1.3 The Plasma-Sheath transition

As was mentioned in section 5.1.1, in order for the Bohm criterion to be fulfilled, the presence of a “presheath region” is needed. It can be shown [10], that while the ions accelerate to satisfy the Bohm criterion, quasi-neutrality can be maintained only through the following presheath mechanisms:

1. Through collisions. In this case the characteristic presheath length is expected to be of the order of the ion mean free path $L \approx L_{mfp}$.
2. Through ionisation. In this case the presheath’s characteristic length is of the order of the ionisation length $L \approx L_i$.
3. In a discharge geometry which allows for current concentration, as in spherical or cylindrical geometries, it is possible to have a “geometric” presheath. The characteristic presheath length is then related to the discharge geometry.
4. Finally, if the plasma extent is restricted, so that the possible characteristic presheath lengths are greater than the discharge lengths, the presheath region coincides with the whole plasma region.

Considering now the transition between the presheath and sheath layers, it appears natural that it results in a singular two-scale problem: on the presheath scale (characteristic length L) the sheath appears as a thin layer

5.1 Introduction

(characteristic length λ_D) with a steep potential gradient, whereas on the sheath scale the presheath appears as a large-scale region with a very weak potential gradient. In the limit $\lambda_D/L \rightarrow 0$ (which corresponds to the collisionless plasma limit), from the presheath perspective the sheath becomes an infinitely small region with $d\Phi/dx \rightarrow -\infty$ at the sheath edge and from the perspective of the sheath the presheath is infinitely long with $d\Phi/dx \rightarrow 0$.

The singularity that occurs at the boundary has been related by Stange-man and Allen [88, 89] and later by Riemann [10] to the marginal equality form of the Bohm criterion. Meanwhile, Emmert *et al.* [28] presented a sheath-presheath model where the sheath edge was not distinguished by a singularity, but this result was an artifact of the inclusion of a source term accounting for the production of hot ions. In a similar model, Bissel and Johnson [29] obtained a singularity at the sheath edge using the marginal form of Bohm's criterion as a boundary condition. The problem of the matching of the presheath and sheath in the collisional case, where λ_D/L has a small but finite value, also presents a lot of difficulties. It was first discussed by Caruso and Cavaliere [90] and further elaborated by Franklin and Ockendon, who presented a model [91] where a transition layer with a characteristic length l_t such that $L \gg l_t \gg \lambda_d$ exists in order to match the presheath to the sheath solutions. Godyak and Sternberg [77] on the other hand, presented a model where there is a smooth transition from the plasma to the sheath, by assuming a finite electric field at the sheath edge. Later, Riemann [92] argued that this transition is non-physical, and that the "intermediate scale" accounting for both collisions and space-charge has to be considered for the matching of the two regions.

In this chapter results obtained with the aid of the PIC simulation [93] are presented. The advantages of this treatment are two-fold: the situation

5.2 Investigation of the single ion species case

can be simplified by studying the plasma sheath transition through collisions only, since there is no ionisation present in the simulation and the geometry is planar. Also, the transition from the plasma to the sheath is done naturally, avoiding the difficulties and the lack of self-consistency present in analytic or semi-analytic [94] models.

5.2 Investigation of the single ion species case

5.2.1 The Bohm criterion in the single ion species case

For the case of a single ion species a model gas with argon mass is used and the ion flux is set equal to $\Gamma_i = 1.55 \times 10^{18} \text{ m}^{-2}\text{s}^{-1}$ corresponding to a value of the density at the sheath edge equal to $n_s = 6.25 \times 10^{15} \text{ m}^{-3}$, provided the Bohm criterion is satisfied with the equality sign. In order to check the validity of the Bohm criterion, the average ion velocity normalised to the Bohm velocity $\langle u \rangle / u_B$ is shown in figure 5.2 as a function of position. The point where the hydrodynamic Bohm criterion is marginally satisfied is marked by the vertical solid line, whereas the kinetic criterion ($\langle 1/u^2 \rangle^{-1} / u_B^2 = 1$) is marked by the dashed line. The difference in the position where this occurs is very small and barely exceeds the discrimination limits of the simulation (the maximum resolution obtained by the simulation is obviously the cell size). Therefore, one can argue that although the kinetic description of the Bohm criterion presents some advantages, from a theoretical point of view, related to the degree of self-consistency and the assumptions used, in practical terms the hydrodynamic description is more easily understood and gives satisfactory results. Note also, that the kinetic criterion is satisfied *after* the hydrodynamic one. The reason for this can be understood by considering

5.2 Investigation of the single ion species case

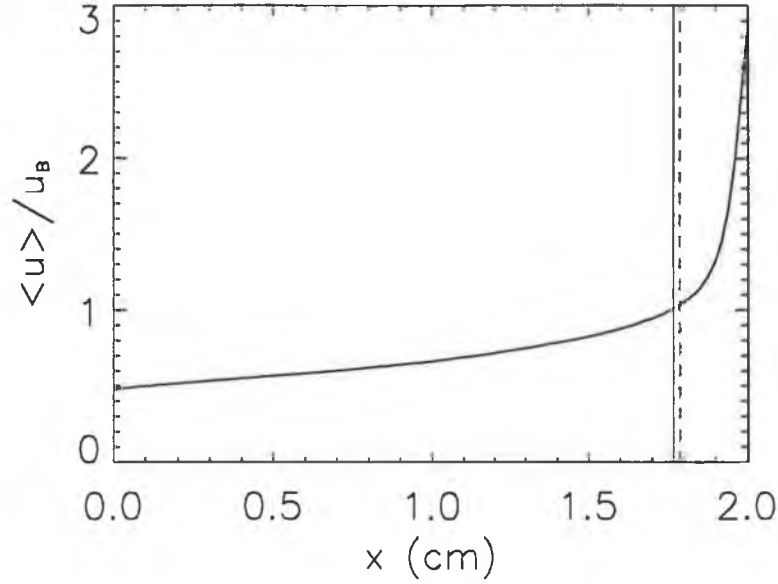


Figure 5.2: The average ion velocity normalised to the Bohm velocity $\langle u \rangle / u_B$ as a function of position. The points where the hydrodynamic and kinetic Bohm criteria are marginally satisfied are indicated by the solid and dashed vertical lines respectively. Conditions: Argon gas, $J = 0 \text{ Am}^{-2}$, $T_e = 2.8 \text{ eV}$, $T_i = 0.025 \text{ eV}$, $P = 10 \text{ mTorr}$ and $n_s = 6.25 \times 10^{15} \text{ m}^{-3}$.

Schwarz's relation

$$\langle x^2 \rangle \geq \langle x \rangle^2 \geq \langle x^{-2} \rangle^{-1}, \quad (5.20)$$

which states that this is to be expected from the statistical properties of the distribution function.

The charge density as a function of position for the same parameters is shown in figure 5.3. As expected, the Bohm criterion accurately describes the transition between the quasi-neutral plasma and the space charge region in the sheath.

5.2 Investigation of the single ion species case

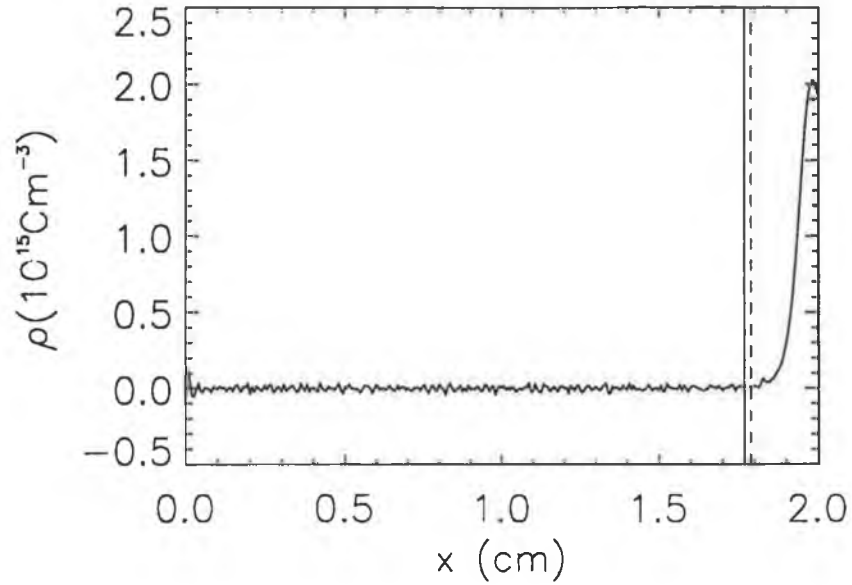


Figure 5.3: *The charge density as a function of position. The vertical lines are as in figure 5.2. Conditions as in figure 5.2.*

5.2.2 The plasma, presheath and sheath regions

Considering now that the geometry is planar and that there is no ionisation present, three separate regions are expected to be present in the simulation:

1. A quasi-neutral plasma region which extends to infinity, where the density and potential drop linearly due to ambipolar diffusion as we approach the sheath.
2. A quasi-neutral presheath region which accelerates the ions and matches the plasma to the sheath region. In this region, the linearity in the density and potential should fail.
3. A space charge sheath region where the ions are further accelerated to

5.2 Investigation of the single ion species case

high velocities due to the presence of the strong sheath electric field and there is a steep variation in the density and potential profiles.

Indeed, in figure 5.4 where the ion density and the potential are shown as a function of position along with linear fits in the plasma region, these three regions can be clearly identified: on the left from $x = 0.0$ cm to about $x = 1.3$ cm the ion density and potential fall linearly, then a quasi-neutral but not linear region follows until about $x = 1.9$ cm, where quasi-neutrality breaks down (see figure 5.3) at the Bohm point and the sheath region starts. The ion mean free path for these conditions is about 6mm, in very good agreement with an estimate from these plots.

Finally, the ion distribution function obtained at various positions in the discharge is shown in figure 5.5. Near the boundary, the distribution has a “double hump” shape due to the ion loading procedure discussed in section 2.3.2. Moving towards the sheath, the distribution relaxes, and after the Bohm point, at about $x = 1.9$ cm, there is essentially no contribution to the distribution of the low-energy thermal ions in the collision-free region of the sheath.

5.2.3 Plasma potential variation in the presheath

The form of the potential in the presheath region is important since it affects the ion distribution function. An analytic estimate of the potential distribution across the presheath, under the assumptions of a collisional presheath with a constant mean free path, has been found by Riemann [10] to be

$$\frac{x}{L_{mfp}} = \frac{1}{2} \left(1 - \exp \left(\frac{2eV}{kT_e} \right) - \frac{2eV}{kT_e} \right), \quad (5.21)$$

where x is measured from the Bohm point and the potential V is zero at $x = 0$. Since equation (5.21) cannot be directly solved for the potential

5.2 Investigation of the single ion species case

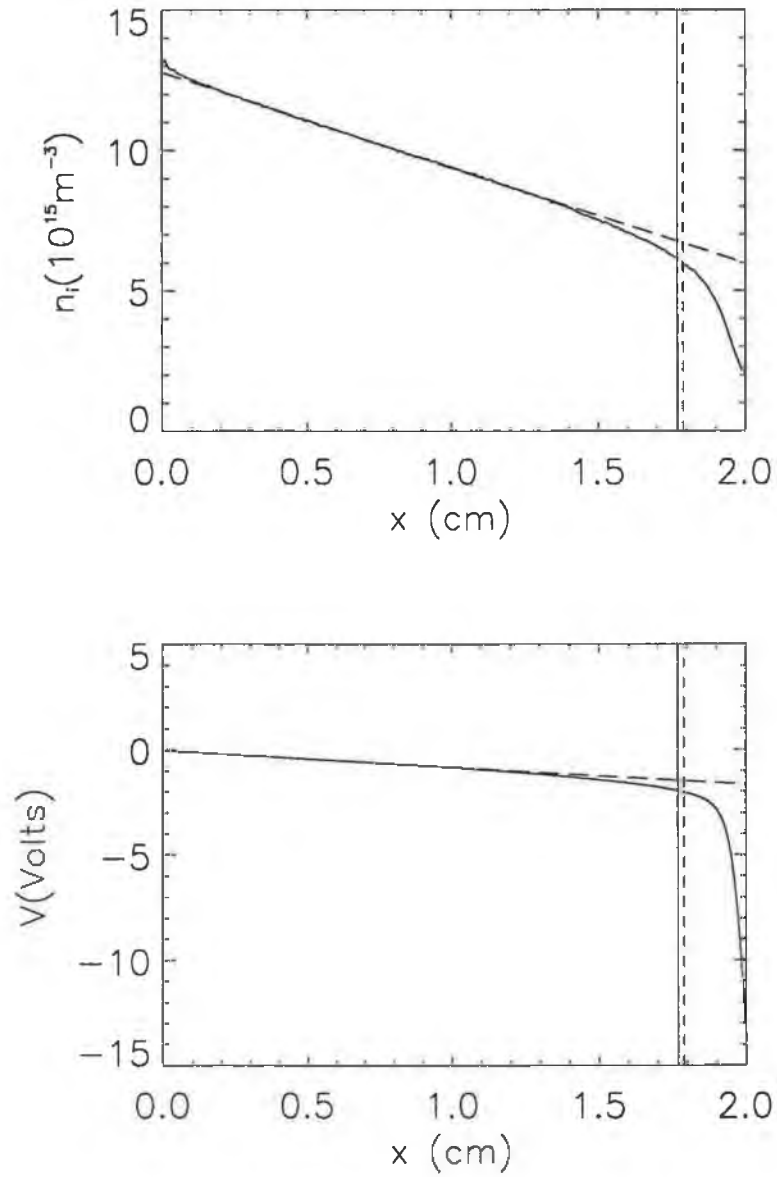


Figure 5.4: The ion density and potential as a function of position (solid lines). The vertical lines are as in figure 5.2. The long-dashed lines shown, are linear fits of the density/potential in the plasma region. Conditions as in figure 5.2.

5.2 Investigation of the single ion species case

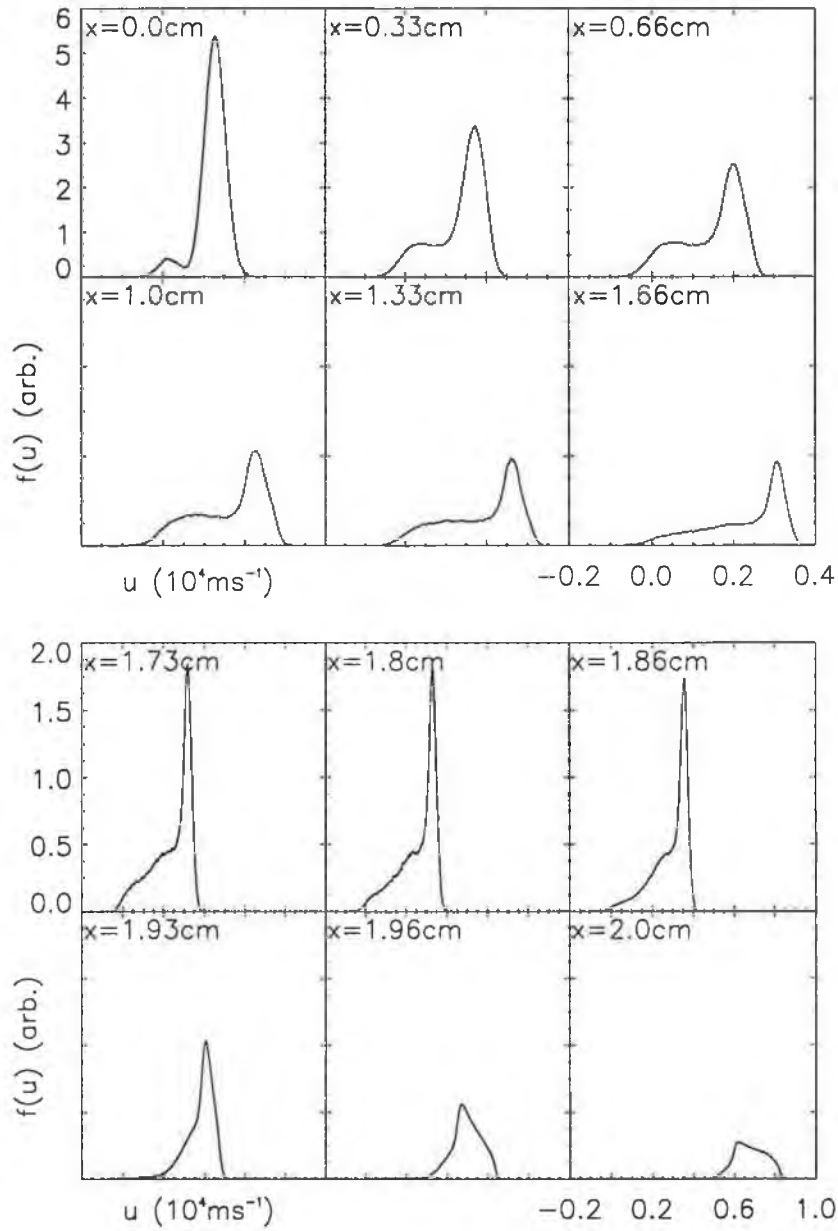


Figure 5.5: The ion distribution function at various positions. All distributions have been normalised together so that at $x = 0$, $\int_{-\infty}^{\infty} f(u) du = 1$. Conditions as in figure 5.2.

5.3 Investigation of the two ion species case

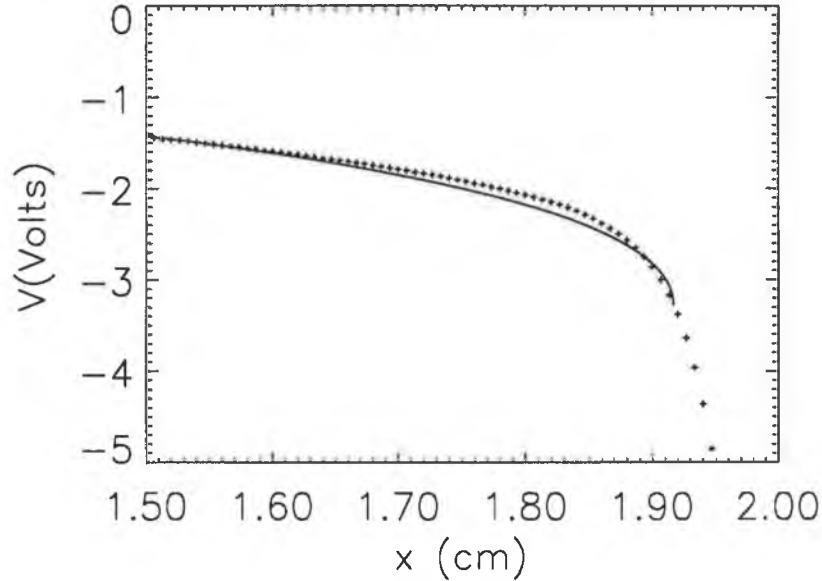


Figure 5.6: *The potential near the Bohm point (+) and the numerical fit from Riemann's estimate (solid line). Conditions as in figure 5.2.*

as a function of the position, a fit of equation (5.21) to the potential curve obtained from the simulation has been performed. The fitting parameters used were the mean free path L_{mfp} and the point of origin (Bohm point). The method used for the fitting is the Levenberg-Marquardt method [95] and it yielded a Bohm point at $x = 1.91$ cm with a mean free path length $L_{mfp} = 4.7$ mm, very close to the actual values. The fit together with the simulation potential close to the Bohm point, are shown in figure 5.6.

5.3 Investigation of the two ion species case

In the case of two or more ion species, the most interesting problem is how the individual average velocities of each of the species are related to satisfy

5.3 Investigation of the two ion species case

the general Bohm criterion. For simplicity, the analysis is restricted to the case of two single charged ions based on argon and helium models. The marginal (hydrodynamic) Bohm criterion is then written as

$$\frac{q_1^2 n_1}{m_1 \langle u_1 \rangle^2} + \frac{q_2^2 n_2}{m_2 \langle u_2 \rangle^2} = \frac{e^2 n_e}{k T_e}. \quad (5.22)$$

After normalising the average velocities to the species' individual Bohm velocities, equation (5.22) can be written as

$$n_1(\tilde{u}_1^{-2} - 1) + n_2(\tilde{u}_2^{-2} - 1) = 0, \quad (5.23)$$

where $\tilde{u}_{1,2} = \langle u_{1,2} \rangle / u_{B1,2}$. It is easy to see from equation (5.23) that either the trivial solution will be satisfied, i.e. both ions will reach the sheath edge with an average velocity equal to their own Bohm velocity, or alternatively one will be subsonic and the other supersonic at the Bohm point.

Let us start by making some general remarks. Ignoring collisions for the time being, since the ions fall through the same potential as they approach the sheath region, they both acquire the same energy and therefore \tilde{u}^2 varies by the same amount. However, due to their finite collisionality each of the ion species experiences a different friction force which restricts the amount of energy gain. Therefore we can intuitively expect that the most collisional ion (a characterisation conveniently described by the ion mean free path) will have $\tilde{u} < 1$ and the less collisional one will have $\tilde{u} > 1$. It also follows that the trivial solution will be obtained if the ion species have the *same* collisionality.

To demonstrate this, a series of simulations have been performed where the ion fluxes are kept constant, but the collision frequencies (and therefore the mean free paths) change. The results of these simulations are tabulated in table 5.1 and shown in figure 5.7 verifying the arguments presented above: the ion species with the larger mean free path arrives at the Bohm point

5.3 Investigation of the two ion species case

#	$L_{He}(\text{cm})$	$L_{Ar}(\text{cm})$	$n_{He}(\text{m}^{-3})$	$n_{Ar}(\text{m}^{-3})$	\tilde{u}_{He}	\tilde{u}_{Ar}
1	1.9	7.4	2.14×10^{15}	8.65×10^{15}	0.93	1.38
2	1.9	1.9	1.94×10^{15}	1.14×10^{15}	1.02	1.02
3	7.7	1.9	1.67×10^{15}	1.34×10^{15}	1.20	0.85

Table 5.1: *The values of the ion mean free paths, ion densities at the sheath edge and ratio of their average velocity to their individual Bohm speed. Conditions: Helium and Argon gases, $J = 0 \text{ Am}^{-2}$, $T_e = 2.8 \text{ eV}$, $T_i = 0.025 \text{ eV}$, $\Gamma_{He} \simeq 1.58 \times 10^{19} \text{ m}^{-2}\text{s}^{-1}$, $\Gamma_{Ar} \simeq 2.94 \times 10^{18} \text{ m}^{-2}\text{s}^{-1}$*

with an average velocity above its own Bohm speed and vice-versa. In the second case presented, where both species have approximately the same mean free path, the normalised velocity profiles are almost identical and both ion species reach their Bohm speed simultaneously at the Bohm point. Note also that the mean free path values indicated in table 5.1 are approximated by a “local” mean free path, $L_{mfp} = \nu_m^{-1} u_B$.

An interesting point which arises from what has been shown so far is that the values of the fluxes that the ions have do not affect which of the two ion species exceeds its Bohm velocity. This is shown in the next set of simulations presented in table 5.2 and figures 5.8 and 5.9, where one of the ion species (helium) maintains the same flux $\Gamma_{He} = 1.58 \times 10^{19} \text{ m}^{-2}\text{s}^{-1}$ while the other one (argon) has a flux that varies from $\Gamma_{Ar} = 9.41 \times 10^{17} \text{ m}^{-2}\text{s}^{-1}$ to $\Gamma_{Ar} = 6.94 \times 10^{18} \text{ m}^{-2}\text{s}^{-1}$. The mean free path for helium for all these cases is $L_{He} \approx 3.8 \text{ cm}$ whereas for argon $L_{Ar} \approx 1.9 \text{ cm}$. As can be seen, helium exceeds its Bohm velocity at the Bohm point, whereas argon does not reach it for all cases. It is interesting also that despite the fact the flux ratio changes by almost an order of magnitude, the velocity profiles are barely affected. In contrast, the density profiles change significantly and while in the first case

5.3 Investigation of the two ion species case

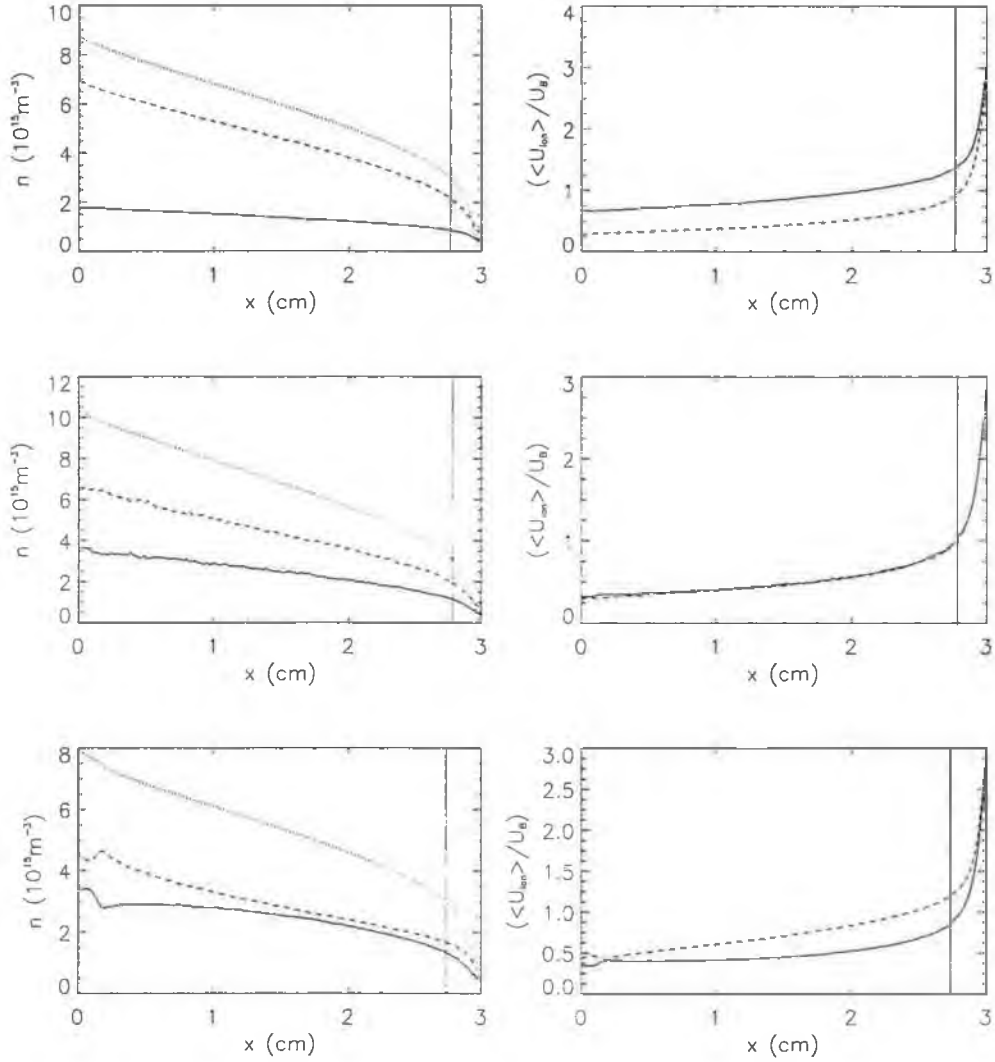


Figure 5.7: The ion density and average ion velocities normalised to the individual Bohm speed as a function of position, for the cases presented in table 5.1. Solid lines correspond to argon, dashed lines to helium, dotted to electrons. The vertical line indicates the Bohm point. Conditions as in table 5.1.

5.4 Summary

#	$\Gamma_{He}(\text{m}^{-2}\text{s}^{-1})$	$\Gamma_{Ar}(\text{m}^{-2}\text{s}^{-1})$	$n_H(\text{m}^{-3})$	$n_A(\text{m}^{-3})$	\tilde{u}_{He}	\tilde{u}_{Ar}
1	1.58×10^{19}	9.41×10^{17}	1.9×10^{15}	6.0×10^{14}	1.1	0.85
2	1.58×10^{19}	2.94×10^{18}	1.8×10^{15}	1.4×10^{15}	1.1	0.9
3	1.58×10^{19}	4.94×10^{18}	1.7×10^{15}	2.1×10^{15}	1.1	0.9
4	1.58×10^{19}	6.94×10^{18}	1.8×10^{15}	2.9×10^{15}	1.1	0.9

Table 5.2: *The values of the ion fluxes, ion densities at the sheath edge and ratio of their average velocity to their individual Bohm speed. Conditions: Helium and Argon gases, $J = 0\text{A/m}^2$, $T_e = 2.8\text{eV}$, $T_i = 0.025\text{eV}$, $P = 20\text{mTorr}$.*

helium is the dominant ion species and argon the minority, in the last case the roles are reversed.

5.4 Summary

In this chapter the ion dynamics within the transition layer from the quasi-neutral plasma to the space-charge region of the sheath have been investigated for the case of collisional ions. This was done for one and two ion species present.

In the single ion species case, it was shown that a presheath region exists in order to accelerate the ions to the Bohm velocity and a stable sheath to be formed. The presheath region was identified as the quasi-neutral region where the density and potential profiles stop falling linearly, as is the case in the bulk plasma. The length of the presheath region has been found to be of the order of the ion mean free path, as predicted by theoretical models, and the potential variation in this region agrees well with Riemann's formula. Finally, the Bohm point, which marks the transition from the quasi-neutral presheath region to the sheath region, was calculated by using the kinetic and

5.4 Summary

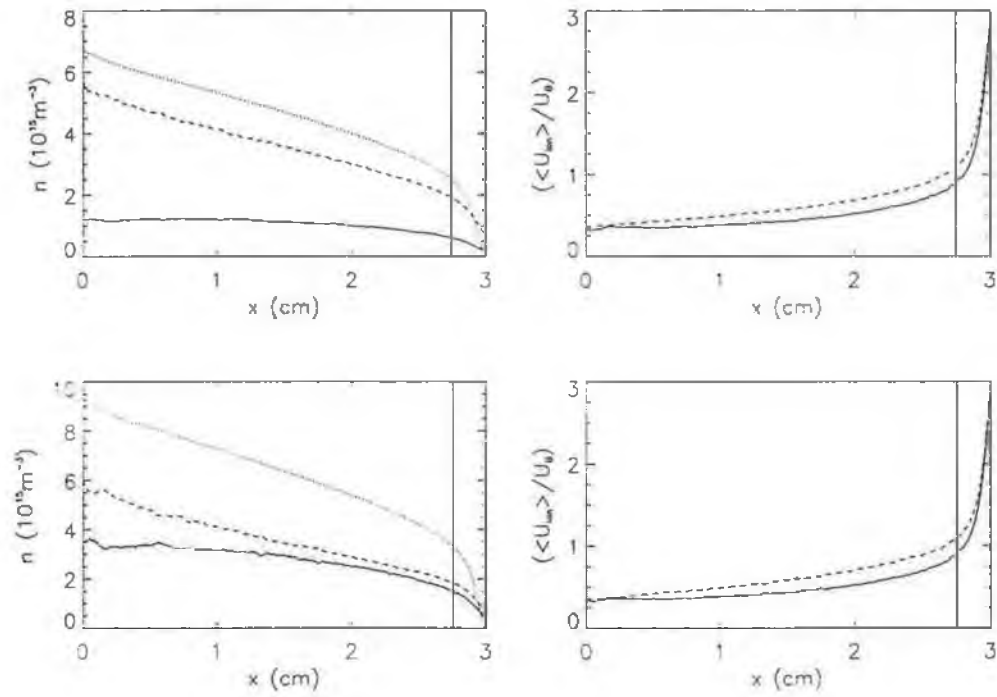


Figure 5.8: The ion density and average ion velocities normalised to the individual Bohm speed as a function of position, for the first two cases of table 5.2. Solid lines correspond to argon, dashed lines to helium, dotted to electrons. The vertical line indicates the Bohm point. Conditions as in table 5.2.

5.4 Summary

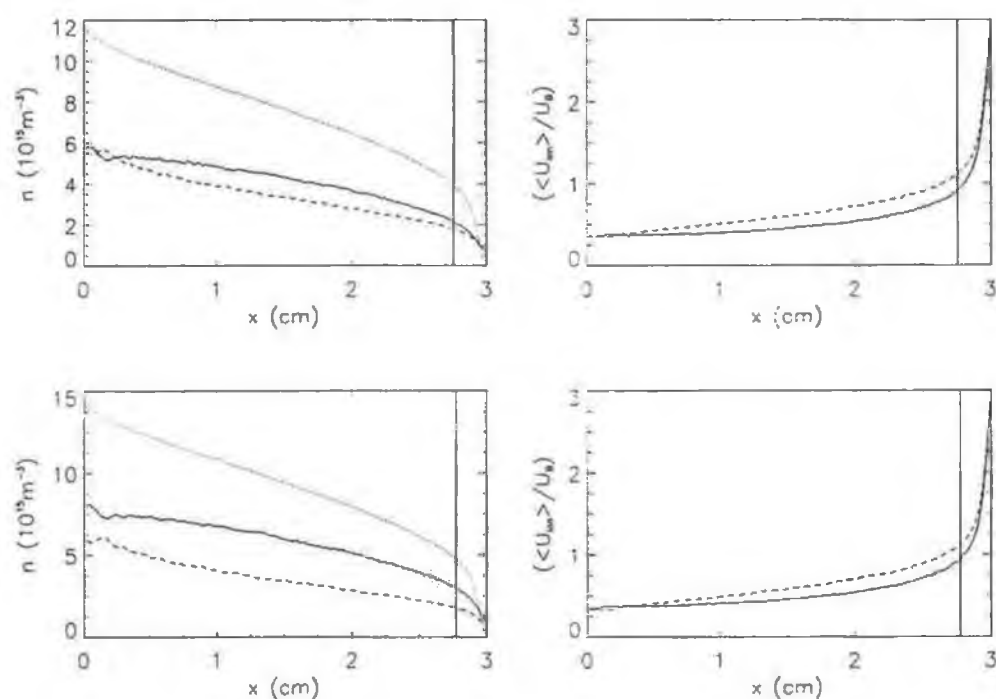


Figure 5.9: The ion density and average ion velocities normalised to the individual Bohm speed as a function of position, for the last two cases of table 5.2. Solid lines correspond to argon, dashed lines to helium, dotted to electrons. The vertical line indicates the Bohm point. Conditions as in table 5.2.

5.4 Summary

hydrodynamic versions of the Bohm criterion. The points indicated by the two criteria were very close together and to the point where quasi-neutrality breaks down. This validates the use of the hydrodynamic criterion.

In the case of two ion species, it was shown that the way the generalised Bohm criterion is satisfied depends on two parameters, the mean free paths and the particle fluxes of the two species. Concerning the mean free path, the less collisional of the two ion species will arrive at the Bohm point having an average velocity exceeding its own Bohm velocity whereas the average velocity of the most collisional one will be less than its Bohm velocity. The special situation where both ion species have on average their own Bohm velocity at the sheath edge is satisfied if and only if they have the same mean free path. On the other hand, the values of the individual ion species fluxes affect the density profiles and to some extent how far the average velocities of the ion species will be from the species Bohm velocities. These results contradict the results obtained by Franklin [86] who, assuming constant ionisation rates and a constant ratio of densities between the ion species everywhere in the discharge, has shown that each of the ion species will have on average its own Bohm velocity. This does not come as a surprise since the conditions presented here and in [86] are different, but most importantly because the constant density ratio assumption which is crucial to Franklin's result is certainly not valid in our simulation and can hardly be valid in general.

CHAPTER 6

Conclusion

In conclusion to this thesis, a summary of the main results presented within it as well as some suggestions for further research work follow in this chapter. The motivation behind this work was to extend our understanding of phenomena associated with the sheaths present in capacitive discharges and consequently further enhance our ability to use plasmas effectively. With that in mind, the primary interest in this work was the study of collisionless heating and in particular the nature of the heating mechanism that provides the energy needed to sustain a capacitive plasma in low-pressure conditions. In addition, the plasma-sheath interface has been examined with a focus on the presheath dynamics and the Bohm criterion. All results presented were obtained through a novel self-consistent simulation based on the Particle-In-Cell simulation scheme and designed to model the sheath/presheath dynamics in a semi-infinite plasma.

6.1 The simulation technique

In chapter 2 the numerical simulation used throughout this research has been presented. The simulation is based on the Particle-In-Cell scheme and is designed to model a current-driven, semi-infinite, one-dimensional plasma in contact with an electrode. Since the goal is to simulate fundamental physical phenomena in the sheath region and its vicinity, the chemistry included in this simulation has been kept to a minimum. Thus ionisation is ignored assuming that it is unimportant over a sheath length and the only collision processes included are elastic scattering for the electrons and charge-exchange for the ions, while in all cases a constant collision frequency is assumed. It is also possible to treat the plasma as completely collisionless.

The semi-infinite plasma which lies outside the simulation volume is modelled by assuming a certain distribution function for each of the species present. In this work drifting Maxwellians were assumed for all species, but different distribution functions could be used in principle. By obtaining the particles which are loaded to the simulation from distributions as consistent as possible with the distribution in the simulation and by dynamically adjusting these distributions as well as the boundary conditions, the source sheath at the boundary is minimised.

Although the simulation has been specifically designed to deal with the problems considered in this work, namely collisionless heating and the plasma-sheath transition in a collisional presheath, there are numerous different ways it could be put in use to support further research, not necessarily strictly related to these problems. An interesting application, for instance, would be to extend this simulation to model cylindrical geometry and use it for Langmuir probe design and interpretation. Due to the complexity of the sheath dynamics probe theory is quite involved and analytic models usually depend

6.2 Collisionless heating

strongly on the assumptions used. In addition, in the simulation presented here, the sheath and the rest of the plasma are only loosely coupled through the plasma boundary conditions. This makes the simulation ideal for gauging the effect of the probe on the plasma and vice-versa. Another possibility could be to model sheaths at conditions different from the ones presented here. For instance, as dual-frequency discharges start becoming available, this simulation could assist in elucidating the complex sheath structure in such devices.

6.2 Collisionless heating

The mechanism through which electrons are heated in the rf sheath in the absence of collisions has been the main subject of this work. In chapter 3 the mechanism of stochastic heating through Fermi acceleration was examined in detail. It has been shown analytically that current conservation does not allow for net heating to take place on average over an entire rf cycle, although some energy transfer takes place in order to maintain the drift energy. Predictions of heating from Lieberman's model have been compared to the simulation and although they do not entirely fail, the agreement is fortuitous since the assumptions used are inconsistent with current conservation. In contrast, it has been shown that when a calculation of heating due to Fermi acceleration is performed self-consistently through the PIC simulation, it yields zero net heating in accordance with the analytic calculation.

Collisionless heating has been further explored in chapter 4. There, it has been shown that heating can be effectively described as the result of the alternating compression and rarefaction of the electrons by the moving sheath. Although this had been already suggested by Surendra and Turner,

6.2 Collisionless heating

it had never been fully articulated, nor was it shown before that pressure heating completely accounts for the power dissipation. In this thesis an analytic model for collisionless heating has been developed which accounts for the sheath structure. The model has been solved analytically for the case of a time-symmetric sheath and the time-averaged power deposition has been expressed as a simple quadrature. Both the instantaneous power deposition and the average power deposition as a function of the plasma parameters were compared with the results of a PIC simulation modelling a symmetric sheath and excellent agreement was found. In addition, it has been shown that for the general case of an asymmetric sheath, although no analytic solution to the model was provided, a numerical solution is in very good agreement with the PIC simulation showing that pressure heating fully accounts for collisionless heating. Finally, the interpretation of collisionless heating as a pressure effect highlights the collective behaviour of the electrons. This also avoids attaching a special importance to the ill-defined notion of a sheath edge.

The goal in this work was to test if the predominant theory of stochastic heating through Fermi acceleration accurately describes the physical mechanism behind collisionless heating and if not, propose an alternative formalism. This has been effectively achieved and the theory of stochastic heating by Fermi acceleration can now be fully replaced by pressure heating, in global discharge models for example. However, there are several issues that remain open and suggest further research. For instance, the assumption of a constant bulk temperature requires a strong thermalisation process in the bulk plasma and cannot be fully met in a realistic discharge. In addition, it is not clear how the presence of two sheaths close to each other, as is commonly the case, will affect the temperature variation in the bulk. Finally the develop-

6.3 The plasma-sheath transition

ment of better analytic models that account for collisions, electron loss and asymmetry in the sheath would make it possible to obtain analytic scalings of power deposition directly comparable to experiments.

6.3 The plasma-sheath transition

The problem of the plasma-sheath transition through a collisional presheath has been treated in chapter 5. In brief, three regions have been identified in the simulation: a quasi-neutral linear bulk plasma region where the density profile is linear due to ambipolar diffusion, a quasi-neutral presheath region with a length of the order of the ion mean free path and finally a space-charge sheath region. The points where the kinetic and hydrodynamic Bohm criteria are satisfied marginally have been calculated and found to be very close to each other, which justifies the use of the hydrodynamic Bohm criterion. The potential in the presheath has been compared to Riemann's analytic calculation and good agreement was found.

Using two ion species, the generalised Bohm criterion has been investigated. It has been shown that for one of the ion species (the one with the larger mean free path) the average velocity has to exceed its Bohm velocity at the sheath edge, whereas for the other ion species the average velocity has to be below its own Bohm velocity. The case of both ions having an average velocity equal to their own Bohm velocity is satisfied if and only if they have the same mean free path.

Although the results presented here do not by any means constitute a complete treatment of the plasma-sheath transition, they represent a useful approach: rather than studying the complete problem in a full discharge, the case of a collisional presheath is isolated and studied independently. This

6.3 The plasma-sheath transition

makes it possible to parametrise the problem (for the case presented here, the parameters being the ion fluxes and collision frequencies) and allows for the comprehension of the physics involved. The technological impact this has is important since whether one measures ion currents through a probe, or does surface processing through ion bombardment, knowledge of the ion dynamics is imperative. It would be therefore instructive to generalise this work and study the plasma-sheath transition through an ionising or geometric presheath, as this would enhance our understanding of the processes involved and would probably open the possibility for a model accounting for all these processes to be constructed.

APPENDIX A

Lieberman's model for a collisionless capacitive rf sheath.

The main features of Lieberman's model describing a collisionless rf sheath driven by a sinusoidal rf current source are presented here. A detailed description of this model can be found elsewhere [7].

The structure of the sheath is as in figure 3.2. Assuming that $\omega_{pi} \ll \omega_{rf} \ll \omega_{pe}$, the ions respond only to time-averaged fields. Therefore particle and energy conservation are given by

$$n_i u_i = n_{i0} u_B, \quad (\text{A.1})$$

$$\frac{1}{2} M u_i^2 = \frac{1}{2} M u_B^2 - e \bar{\Phi}, \quad (\text{A.2})$$

where $\bar{\Phi}$ is the time-averaged potential and u_B is the Bohm velocity. Due to ion flux conservation, the ion density $n_i(x)$ falls as the ions are accelerated from the bulk towards the electrode. It is assumed that the electron density $n_e(x, t)$ follows the ion density, maintaining quasi-neutrality until the sheath

edge, such that

$$n_e(x, t) = \begin{cases} n_i(x) & \text{for } x < s(t), \\ 0 & \text{otherwise,} \end{cases} \quad (\text{A.3})$$

where $s(t)$ is the position of the electron sheath edge.

The electron sheath edge oscillates nonlinearly between the bulk plasma and the maximum sheath thickness s_m denoted as $x = 0$ and $x = s_m$ respectively in figure 3.2. Defining $2\phi(x)$ as the phase interval during which $s(t) < x$, the average electron density \bar{n}_e can be written as

$$\bar{n}_e = \left(1 - \frac{2\phi}{2\pi}\right). \quad (\text{A.4})$$

Taking the sinusoidal rf current to be $J_{rf} = -\tilde{J}_0 \sin \omega t$, ignoring the ion current which is negligible, and taking the current to be convection current on the left of the sheath edge and displacement current on the right, current continuity at the electron sheath edge gives

$$-en_i(s) \frac{ds}{dt} = -\tilde{J}_0 \sin \omega t. \quad (\text{A.5})$$

The system of equations is closed by obtaining the electric field through Poisson's equation

$$E = \begin{cases} \frac{e}{\epsilon_0} \int_{s(t)}^x n_i(\zeta) d\zeta & \text{for } s(t) < x, \\ 0 & \text{otherwise.} \end{cases} \quad (\text{A.6})$$

One can now solve for the ion density and the electron sheath position to obtain

$$\frac{n_i}{n_0} = \left[1 - H \left(\frac{3}{8} \sin 2\phi - \frac{1}{4} \phi \cos 2\phi - \frac{1}{2} \phi \right)\right]^{-1} \quad \text{and} \quad (\text{A.7})$$

$$\frac{x}{s_0} = 1 - \cos \phi + \frac{H}{8} \left[\frac{3}{2} \sin \phi + \frac{11}{18} \sin 3\phi - 3\phi \cos \phi - \frac{1}{3} \phi \cos 3\phi \right], \quad (\text{A.8})$$

where n_0 is the ion density at the bulk plasma, $\tilde{s}_0 = \tilde{J}_0/(e\omega n_0)$ is an effective amplitude of the sheath oscillation, and $H = \tilde{s}_0^2/(\pi\lambda_D^2)$.

Bibliography

- [1] M. A. Lieberman and A. J. Lichtenberg. *Principles of Plasma Discharges and Materials Processing*. Wiley, New York, 1994.
- [2] D.M. Manos and D.L. Flamm, editors. *PLasma Etching, An Introduction*. Academic Press, San Diego, CA, 1988.
- [3] V. A. Godyak. *Soviet Radio Frequency Discharge Research*. Delphic Associates, Inc., Falls Church, VA, 1986.
- [4] M. A. Lieberman and V. A. Godyak. From Fermi Acceleration to Collisionless Discharge Heating. *IEEE Trans. Plasma Sci.*, 26(3):955–986, June 1998.
- [5] Y. P. Raizer, M. N. Shneider, and N. A. Yatsenko. *Radio-frequency capacitive discharges*. CRC Press, Boca Raton, 1995.
- [6] W. J. Goedheer. Lecture notes on radio-frequency discharges, dc potentials, ion and electron energy distributions. *Plasma Sources Sci. Technol.*, 9:507–516, 2000.

BIBLIOGRAPHY

- [7] M. A. Lieberman. Analytical solution for capacitive rf sheath. *IEEE Trans. Plasma Sci.*, 16(6):638–644, December 1988.
- [8] F. F. Chen. Electric probes. In R.H. Huddleston and S. L. Leonard, editors, *Plasma Diagnostic Techniques*, volume 21 of *Pure and Applied physics*. Academic Press, New York, 1965.
- [9] D. Bohm. Minimum ionic kinetic energy for a stable sheath. In A. Guthry and R. K. Wakerling, editors, *The Characteristics of Electrical Discharges in Magnetic Fields*, chapter 3, pages 77–86. MacGraw-Hill, New York, 1949.
- [10] K.-U. Riemann. The Bohm criterion and sheath formation. *J. Phys. D: Appl. Phys.*, 24:493–518, 1991.
- [11] H. M. Mayer. Measurements with a wide-band probe. In *Proceedings of the VIth International Conference on Ionization Phenomena in Gases*, volume 4, pages 129–134, 1964.
- [12] M. Surendra and D. B. Graves. Electron accoustic waves in capacitively coupled, low-pressure rf glow discharges. *Phys. Rev. Lett.*, 66(11):1469–1472, November 1991.
- [13] M. M. Turner. Pressure heating of electrons in capacitively-coupled rf discharges. *Phys. Rev. Lett.*, 75(7):1312–1315, August 1995.
- [14] C. K. Birdsall and A. B. Langdon. *Plasma Physics via Computer Simulation*. Adam Hilger, Bristol, 1991.
- [15] R. W. Hockney and J. W. Eastwood. *Computer Simulation Using Particles*. Adam Hilger, Bristol, 1988.

BIBLIOGRAPHY

- [16] T. J. Sommerer, W. N. G. Hitchon, and J. E. Lawler. Electron heating mechanisms in helium rf glow discharges: a self-consistent kinetic calculation. *Phys. Rev. Lett.*, 63(21):2361–2364, November 1989.
- [17] G. G. Lister. Low-pressure gas discharge modeling. *J. Phys. D: Appl. Phys.*, 25:1649–1680, 1992.
- [18] J. M. Dawson. Thermal relaxation in a one-species, one-dimensional plasma. *Phys. Fluids*, 7(3):419–425, 1964.
- [19] C. K. Birdsall. Particle-in-cell charged-particle simulations, plus Monte Carlo collisions with neutral atoms, PIC-MCC. *IEEE Trans. Plasma Sci.*, 19(2):65–85, April 1991.
- [20] V. Vahedi, G. DiPeso, C. K. Birdsall, M. A. Lieberman, and T. D. Rognlien. Capacitive RF discharges modelled by particle-in-cell Monte Carlo simulation. I. analysis of numerical techniques. *Plasma Sources Sci. Technol.*, 2:261–272, 1993.
- [21] V. Vahedi, C. K. Birdsall, M. A. Lieberman, G. DiPeso, and T. D. Rognlien. Capacitive RF discharges modelled by particle-in-cell Monte Carlo simulation. II. Comparison with laboratory measurements of electron energy distribution functions. *Plasma Sources Sci. Technol.*, 2:273–278, 1993.
- [22] G. Gozadinos, D. Vender, and M.M. Turner. Boundary conditions and particle loading for the modeling of a semi-infinite plasma. Accepted for publication in *J. Comp. Phys.*, 2001.
- [23] M. Surendra and D. Vender. Collisionless electron heating by radio-frequency plasma sheaths. *Appl. Phys. Lett.*, 65(2):153–155, July 1994.

BIBLIOGRAPHY

- [24] R. Chodura. Plasma-wall transition in an oblique magnetic field. *Phys. Fluids*, 25(9):1628–1633, September 1982.
- [25] A. V. Phelps. The application of scattering cross sections to ion flux models in discharge sheaths. *J. Appl. Phys.*, 76(2):747–753, July 1994.
- [26] J.P. Verboncoeur, M.V. Alves, V. Vahedi, and C.K. Birdsall. Simultaneous potential and circuit solution for 1d bounded plasma particle simulation codes. *J. Comp. Phys.*, 104:321–328, February 1993.
- [27] K.-U. Riemann. The Bohm Criterion and Boundary Conditions for a Multicomponent System. *IEEE Trans. Plasma Sci.*, 23(4):709–716, August 1995.
- [28] G. A. Emmert, R. M. Wieland, A. T. Mense, and J. N. Davidson. Electric sheath and presheath in a collisionless finite ion temperature plasma. *Phys. Fluids*, 23(4):803–812, April 1980.
- [29] R. C. Bissell and P. C. Johnson. The solution of the plasma equation in plane parallel geometry with a maxwellian source. *Phys. Fluids*, 30(3):779–786, March 1987.
- [30] L. D. Landau. On the vibrations of the electronic plasma. *J. Physics USSR*, 10:25–34, 1946.
- [31] E. Fermi. On the Origin of the Cosmic Radiation. *Phys. Rev.*, 75(8):1169–1174, April 1949.
- [32] A. J. Lichtenberg and M. A. Lieberman. *Regular and Chaotic Dynamics*. Springer-Verlag, New York, 1992.
- [33] G. M. Zaslavskii and B. V. Chirikov. Mechanism for fermi acceleration in a one-dimensional case. *Sov. Phys. Dokl.*, 9(11):989–992, July 1965.

BIBLIOGRAPHY

- [34] M. A. Lieberman and A. J. Lichtenberg. Stochastic and adiabatic behavior of particles accelerated by periodic forces. *Phy. Rev. A*, 5:1852–1866, 1972.
- [35] A. J. Lichtenberg, M. A. Lieberman, and R. H. Cohen. Fermi acceleration revisited. *Physica*, 1D:291–305, 1980.
- [36] M. A. Lieberman. The dynamics of fermi acceleration. In Uwe Kortshagen and Lev D. Tsendin, editors, *Electron Kinetics and Applications of Glow Discharges*, volume 367 of *NATO ASI Series B*, pages 215–226. Plenum Press, New York, 1998.
- [37] A. J. Lichtenberg. Application of mapping dynamics to analysis of a capacitive rf discharge. In Uwe Kortshagen and Lev D. Tsendin, editors, *Electron Kinetics and Applications of Glow Discharges*, volume 367 of *NATO ASI Series B*, pages 227–240. Plenum Press, New York, 1998.
- [38] D. Gabor, E. A. Ash, and D. Dracott. Langmuir paradox. *Nature*, 176 (4489):916–919, 1955.
- [39] J. Pavkovich and G. S. Kino. R.F. theory of the plasma sheath. In *Proceedings of the VIth International Conference on Ionization Phenomena in Gases*, page 39, 1964.
- [40] V. A. Godyak. Statistical heating of electrons at an oscillating plasma boundary. *Sov. Phys. - Tech. Phys.*, 16(7):1073–1076, January 1972.
- [41] A. I. Akhiezer and A.S. Bakai. Stochastic plasma heating by rf fields. *Sov. J. Plasma Phys.*, 2(4):359–361, July-August 1976.
- [42] Yu. R. Alanakyan. Fermi acceleration and rf particle heating. *Sov. Phys. - Tech. Phys.*, 24(5):611–612, May 1979.

BIBLIOGRAPHY

- [43] C. G. Goedde, A. J. Lichtenberg, and M. A. Lieberman. Self-consistent stochastic electron heating in radio frequency discharges. *J. Appl. Phys.*, 64(9):4375–4383, November 1988.
- [44] U. Kortshagen, C. Busch, and L. D. Tsendin. On simplifying approaches to the solution of the Boltzmann equation in spatially inhomogenous plasmas. *Plasma Sources Sci. Technol.*, 5:1–17, 1996.
- [45] A. S. Smirnov and L. D. Tsendin. The space-time-averaging procedure and modeling of the rf discharge. *IEEE Trans. Plasma Sci.*, 19(2):130–140, April 1991.
- [46] I. D. Kaganovich and L. D. Tsendin. The space-time-averaging procedure and modeling of the rf discharge, part ii: Model of collisional low-pressure rf discharge. *IEEE Trans. Plasma Sci.*, 20(2):66–75, April 1992.
- [47] I. D. Kaganovich and L. D. Tsendin. Low-pressure rf discharge in the free-flight regime. *IEEE Trans. Plasma Sci.*, 20(2):86–92, April 1992.
- [48] I. D. Kaganovich, V. I. Kolobov, and L. D. Tsendin. Stochastic electron heating in bounded radio-frequency plasmas. *Appl. Phys. Lett.*, 69(25):3818–3820, December 1996.
- [49] Z. Wang, A. J. Lichtenberg, and R. H. Cohen. Space-averaged kinetic analysis of stochastically heated electropositive and electronegative rf capacitive discharges. *Plasma Sources Sci. Technol.*, 8:151–161, 1999.
- [50] U. Buddemeier and I. D. Kaganovich. Collisionless electron heating in rf gas discharges: II. The role of collisions and non-linear effects. In Uwe Kortshagen and Lev D. Tsendin, editors, *Electron Kinetics and*

BIBLIOGRAPHY

- Applications of Glow Discharges*, volume 367 of *NATO ASI Series B*, pages 283–291. Plenum Press, New York, 1998.
- [51] Y. M. Aliev, I. D. Kaganovich, and H. Schlüter. Collisionless electron heating in rf gas discharges: I. Quasilinear theory. In Uwe Kortshagen and Lev D. Tsendin, editors, *Electron Kinetics and Applications of Glow Discharges*, volume 367 of *NATO ASI Series B*, pages 257–281. Plenum Press, New York, 1998.
- [52] V. A. Godyak, O. A. Popov, and A. H. Khanna. Effective electron collision frequency in rf discharge. *Sov. J. Plasma Phys.*, 2:560–561, 1976.
- [53] V. A. Godyak and O. A. Popov. Experimental study of resonant rf discharge. *Sov. J. Plasma Phys.*, 5:227–221, 1979.
- [54] O. A. Popov and V. A. Godyak. Power dissipated in low-pressure radio-frequency discharge plasmas. *J. Appl. Phys.*, 57(1):53–58, January 1985.
- [55] V. A. Godyak and R. B. Piejak. Abnormally low electron temperature and heating-mode transition in a low-pressure rf discharge at 13.56 MHz. *Phys. Rev. Lett.*, 65(8):996–999, August 1990.
- [56] V. A. Godyak, R. B. Piejak, and B. M. Alexandrovich. Electrical characteristics of parallel-plate rf discharges in argon. *IEEE Trans. Plasma Sci.*, 19(4):660–676, August 1991.
- [57] V. A. Godyak, R. B. Piejak, and B. M. Alexandrovich. Measurements of electron energy distribution in low-pressure rf discharges. *Plasma Sources Sci. Technol.*, 1(1):36–58, March 1992.

BIBLIOGRAPHY

- [58] U. Kortshagen U. Buddemeier and I. Pukropski. On the efficiency of the electron sheath heating in capacitively coupled radio frequency discharges in the weakly collisional regime. *Appl. Phys. Lett.*, 67(2):191–193, 1995.
- [59] M. Surendra, D.B. Graves, and I.J. Morey. Electron heating in low-pressure rf glow discharges. *Appl. Phys. Lett.*, 56(11):1022–1024, 1990.
- [60] M. Surendra and M. Dalvie. Moment analysis of rf parallel-plate-discharge simulations using the particle-in-cell with monte carlo collisions technique. *Phy. Rev. E*, 48(5):3914–3924, November 1993.
- [61] D. Vender and R. W. Boswell. Numerical modeling of low-pressure RF plasmas. *IEEE Trans. Plasma Sci.*, 18(4):725–732, August 1990.
- [62] D. Vender and R. W. Boswell. Electron-sheath interaction in capacitive radio-frequency plasmas. *J. Vac. Sci. Technol. A*, 10(4):1331–1338, Jul/Aug 1992.
- [63] M. Surendra. Radiofrequency discharge benchmark model comparison. *Plasma Sources Sci. Technol.*, 4:56–73, 1995.
- [64] M. J. Kushner. Monte-carlo simulation of electron properties in rf parallel plate capacitively coupled discharges. *J. Appl. Phys.*, 54(9):4958–4965, September 1983.
- [65] A. E. Wendt and W. N. G. Hitchon. Electron heating by sheaths in radio frequency discharges. *J. Appl. Phys.*, 71(10):4718–4726, May 1992.
- [66] G. Gozadinos, D. Vender, and M.M. Turner. Monte-carlo simulations of collisionless heating in rf plasma sheaths. In *Proceedings of the 51st Annual Gaseous Electronics Conference.*, Maui, Hawaii, USA, 1998.

BIBLIOGRAPHY

- [67] G. Gozadinos, D. Vender, and M.M. Turner. Numerical simulations of stochastic heating in radiofrequency discharges. In *Proceedings of the XIVth ESCAMPIG*, Malahide, Ireland, August 1998.
- [68] M. M. Turner and M. B. Hopkins. Anomalous sheath heating in a low-pressure rf discharge in nitrogen. *Phys. Rev. Lett.*, 69:3511–3514, December 1992.
- [69] A.H. Sato and M.A. Lieberman. Electron-beam probe measurements of electric fields in rf discharges. *J. Appl. Phys.*, 68(12):6117–6124, December 1990.
- [70] G. Gozadinos, D. Vender, M.M. Turner, and M.A. Lieberman. Collisionless electron heating by capacitive radio-frequency plasma sheaths. *Plasma Sources Sci. Technol.*, 10:117–124, 2001.
- [71] J. Borovsky. The dynamic sheath: Objects coupling to plasmas on electron-plasma frequency time scales. *Phys. Fluids*, 31:1074–1100, 1988.
- [72] B. P. Wood, M. A. Lieberman, and A. J. Lichtenberg. Sheath motion in a capacitively coupled radio frequency discharge. *IEEE Trans. Plasma Sci.*, 19(4):619–627, August 1991.
- [73] M. Surendra. *Numerical Simulations of Glow Discharges*. PhD thesis, Chemical Engineering, University of California, Berkeley, 1991.
- [74] M. M. Turner. Collisionless heating in capacitively-coupled radio frequency discharges. In Uwe Kortshagen and Lev D. Tsendin, editors, *Electron Kinetics and Applications of Glow Discharges*, volume 367 of *NATO ASI Series B*, pages 313–328. Plenum Press, New York, 1998.

BIBLIOGRAPHY

- [75] G. Gozadinos, M.M. Turner, and D. Vender. On the pressure heating of electrons by capacitive rf sheaths. Submitted for publication to *Phys. Rev. Lett.*, 2001.
- [76] V. A. Godyak. Steady-state low-pressure rf discharge. *Sov. J. Plasma Phys.*, 2(1):78–84, 1976.
- [77] V. A. Godyak and N. Sternberg. Dynamic model of the electrode sheaths in symmetrically driven rf discharges. *Phys. Rev. A*, 42(4):2299–2312, August 1990.
- [78] H-B Valentini and E. Glauche. Steady state expansion of a low-pressure plasma including collisions and space charge effects. *J. Phys. D: Appl. Phys.*, 28:2279–2286, 1995.
- [79] H-B Valentini. Sheath formation in low-pressure discharges. *Plasma Sources Sci. Technol.*, 9:574–582, 2000.
- [80] I. Langmuir. The interaction of electron and positive ion space charges in cathode sheaths. *Phys. Rev.*, 33:954–989, June 1929.
- [81] L. Tonks and I. Langmuir. A general theory of the plasma of an arc. *Phys. Rev.*, 34:876–922, September 1929.
- [82] J.E. Allen and P.C. Thonemann. Current limitation in the low-pressure mercury arc. *Proc. Phys. Soc. (London)*, B67:768–774, 1954.
- [83] E. R. Harrison and W. B. Thompson. The low pressure plane symmetric discharge. *Proc. Phys. Soc.*, 74:145–152, 1959.
- [84] L. S. Hall. Harrison-Thompson generalization of bohm's sheath condition. *Proc. Phys. Soc.*, 80:309–311, 1962. Letter to the editor.

BIBLIOGRAPHY

- [85] K.-U. Riemann. Kinetic theory of the plasma sheath transition in a weakly ionized plasma. *Phys. Fluids*, 24:2163–2172, December 1981.
- [86] R. N. Franklin. Plasmas with more than one species of positive ion and the bohm criterion. *J. Phys. D: Appl. Phys.*, 33:3186–3189, May 2000.
- [87] N. Hershkowitz and L. Oskuz. Experimental test of riemann and godyak presheath/sheath transition and sheath electric field scaling. In *Proceedings of the XVth ESCAMPIG*, pages 474–475, Lillafured, Hungary, August 2000.
- [88] P. C. Stangeby and J. E. Allen. Plasma boundary as a Mach surface. *J. Phys. A: Math. Gen.*, 3:304–308, 1970.
- [89] J.E. Allen. A note on the generalized sheath criterion. *J. Phys. D: Appl. Phys.*, 9(16):2331–2332, 1976.
- [90] A. Caruso and A. Cavaliere. The structure of the collisionless plasma-sheath transition. *Nuovo Cimento*, XXVI(6):5221–5236, 1962.
- [91] R. N. Franklin and J. R. Ockendon. Asymptotic matching of plasma and sheath in an active low pressure discharge. *J. Plasma Physics*, 4(2): 371–385, 1970.
- [92] K.-U. Riemann. The influence of collisions on the plasma sheath transition. *Phys. Plasmas*, 4(11):4158–4166, November 1997.
- [93] G. Gozadinos, D. Vender, and M.M. Turner. Self-consistent pic simulation of a planar probe. In *Proceedings of the XVth ESCAMPIG*, pages 318–319, Lillafured, Hungary, August 2000.
- [94] T. E. Nitschke and D. B. Graves. Matching an rf sheath model to a bulk plasma model. *IEEE Trans. Plasma Sci.*, 23(4):717–727, 1995.

BIBLIOGRAPHY

- [95] W. H. Press, S. A. Teukolsky, W. T. Vetterling, and B. P. Flannery.
Numerical Recipes in C. Cambridge University Press, Cambridge, 1992.